



**TECHNISCHE
UNIVERSITÄT
WIEN**

Vienna University of Technology

DISSERTATION

**Spatio-temporal behaviour
of the catalytic hydrogen oxidation
on high-Miller-index rhodium surfaces**

ausgeführt zum Zwecke der Erlangung des akademischen Grades eines
Doktors der Naturwissenschaften unter der Leitung von

Assoc.Prof. Dipl.-Phys. Dr.rer.nat. Yuri Suchorski
Univ.Prof. Mag.rer.nat. Dr.rer.nat. Günther Rupprechter
Institut für Materialchemie (E165)

eingereicht an der Technischen Universität Wien
Fakultät für Technische Chemie

von

Martin Datler

Matrikelnummer e00625984

Liechtensteinstraße 117

1090 Wien, Österreich

12.06.2017

Kurzfassung

Das Ziel dieser Dissertation war es, das Reaktionsverhalten der katalytischen H₂-Oxidation auf hoch indizierten Rhodium-Oberflächen unter Hochvakuumbedingungen zu untersuchen. Zu diesem Zweck wurde eine orts aufgelöste Methode, die Photoelektronenemissionsmikroskopie (PEEM), verwendet, um die Reaktionskinetik *in situ* auf den unterschiedlich orientierten, µm-großen Domänen einer polykristallinen Rh-Folie zu untersuchen. Die Rh-Folie dient in dieser Studie als Modellkatalysator, da die kristallographisch unterschiedlich orientierten Domänen der Folie strukturelle Ähnlichkeiten mit den gestuften Oberflächen der Rh-Nanopartikel aufweisen, welche in kommerziellen Katalysatoren verwendet werden.

Da die Oberflächenkonzentration der adsorbierten Reaktanten (Sauerstoff und Wasserstoff) sowohl die katalytische Aktivität der Rh-Oberfläche als auch ihre lokale Austrittsarbeit (welche mit der Helligkeit der aufgenommen PEEM-Bilder korreliert) beeinflusst, kann die Analyse der lokalen PEEM-Helligkeit Aufschluss über die lokale katalytische Aktivität der Oberfläche geben (*kinetics by imaging* approach). Demnach ist es möglich, die kinetischen Übergänge zwischen dem inaktiven und dem reaktiven Zustand des Katalysators mittels PEEM *in situ* zu beobachten. Diese Übergänge der katalytischen Aktivität finden durch die Ausbreitung von Reaktions-Diffusions-Fronten statt. Unter bestimmten Reaktionsbedingungen, können auch sogenannte „chemische Wellen“ und oszillierende Muster auftreten.

Die Beobachtung solcher kinetischen Übergänge mittels PEEM zeigt, dass die auftretenden Reaktionsfronten sowohl an Defekten innerhalb der Domänen als auch an den Domänengrenzen nukleieren. Desweiteren konnte der Einfluss der domänenspezifischen Oberflächenstrukturen, welche mithilfe der Elektronenrückstreubeugung bestimmt wurden, auf die anisotrope Ausbreitung der Fronten beobachtet werden. Der Beschuss der Probe mit Ar⁺ Ionen erzeugt zusätzliche Defekte, welche die Anisotropie der Frontausbreitung verringern.

Im Gegensatz zur CO-Oxidation auf polykristallinen Oberflächen, wird die Ausbreitung von Reaktionsfronten in der H₂-Oxidation nicht von Domänengrenzen begrenzt. Da Wasserstoff über Korngrenzen hinweg diffundieren kann, wird das katalytische Verhalten der einzelnen Domänen durch die Diffusion von Wasserstoff gekoppelt. Die Reaktionskinetik der H₂-Oxidation auf der Rh-Folie im Bereich der Bistabilität konnte bestimmt werden, indem die lokale Änderung der PEEM-Intensität während der zyklischen

Veränderung des Wasserstoffdruckes (bei gleichbleibendem Sauerstoffdruck und konstanter Proben­temperatur) analysiert wurde. Die Ergebnisse mehrerer solcher Messungen wurden in einem „kinetischen Phasendiagramm“ zusammengefasst, welches die Reaktivitätszustände des katalytischen Systems im (p,T) -Parameterraum darstellt. Analog dazu wurde ein kinetisches Phasendiagramm für eine Rh-Folie konstruiert, welche zusätzlich mit Ar^+ Ionen beschossen wurde. Die Verschiebung des Diagramms der mit Ionen beschossen und dadurch defektreicheren Oberfläche in Richtung eines niedrigeren Wasserstoffdruckes spiegelt die höhere Toleranz der raueren Oberfläche gegenüber der Vergiftung mit Sauerstoff wieder.

Neben dem bistabilen Verhalten der H_2 -Oxidation auf Rh, wurden in einem bestimmten Parameterbereich auch Oszillationen der lokalen PEEM-Intensität beobachtet, obwohl alle externen Parameter konstant gehalten wurden. Sowohl die Oszillationsfrequenzen als auch die auftretenden Muster variierten auf den unterschiedlich orientierten Domänen, obwohl sich die auftretenden Reaktionsfronten über die Domänengrenzen hinweg ausbreiteten. Der Vergleich der räumlichen Verteilung der Oszillationsfrequenzen mit den lokalen Oberflächenstrukturen zeigte, dass auf gestuften Rh-Oberflächen, welche vicinal zu $\text{Rh}(110)$ sind, eine höhere Dichte der niedrig koordinierten Kanten- und Kinkatome zu einer höheren Oszillationsfrequenz führt.

Die beobachteten Oszillationsmuster bestehen hauptsächlich aus sich ausbreitenden und miteinander überlappenden, spiralförmigen Wellen, welche sich, ähnlich den Reaktionsfronten, über Domänengrenzen hinweg verbreiten. Die Analyse der Form einer solchen Welle, welche sich über drei unterschiedliche Domänen ausbreitete, zeigte, dass sich die Breite, der Radius und die Ausbreitungsgeschwindigkeit der Spirale beim Überschreiten einer Korngrenze sprunghaft ändern. Dieses Verhalten spiegelt die Abhängigkeit der Wellenausbreitung von der Oberflächenstruktur wieder.

Um ein tieferes Verständnis des Einflusses der Oberflächenstruktur auf die sich selbst erhaltenden Oszillationen zu erlangen, wurde das katalytische Verhalten der H_2 -Oxidation auf einer $\text{Rh}(111)$ -Einkristalloberfläche, welche einen mesoskopischen Defekt aufweist, untersucht. Mithilfe der Rasterkraftmikroskopie konnte gezeigt werden, dass die Seitenwände des $30\ \mu\text{m}$ breiten und $1\ \mu\text{m}$ tiefen grabenartigen Defektes stark gestuft sind. Die Beobachtung, dass die Reaktion ausschließlich innerhalb des Defektes oszilliert, deutet darauf hin, dass eine ausreichende Rauheit der Rh-Oberflächen für die Existenz der Oszillationen notwendig ist. Weitere PEEM-Beobachtungen zeigen, dass, abgesehen von den Reaktionsbedingungen, auch die Orientierung der atomaren Stufen, die Breite der Stufen und die Rauheit der Stufenkante die Existenz der Oszillationen bestimmt.

Die Oberflächenstruktur der Domänen der polykristallinen Rh-Folie ähnelt denen der Nanopartikel, welche in kommerziellen Katalysatoren verwendet werden, obgleich sich ihre Größe signifikant unterscheidet. Um zu überprüfen, ob die erhaltenen Ergebnisse auch auf der nm-Skala gültig sind, wurden die PEEM-Ergebnisse mit denen einer Feldelektronenmikroskopie-Studie, bei der die katalytische H₂-Oxidation auf einer stark gestuften Oberfläche einer Rh-Nanospitze untersucht wurde, verglichen. Der Vergleich der kinetischen Phasendiagramme zeigt, dass die Spitze eine noch höhere Toleranz gegenüber der Vergiftung mit Sauerstoff aufweist als die zusätzlich mit Ar⁺ Ionen beschossene Rh-Folie. Außerdem oszilliert die H₂-Oxidation auf der Rh-Nanospitze mit einer höheren Frequenz als auf den Domänen der Rh-Folie. Diese Beobachtungen bestätigen die Ergebnisse der PEEM-Studie, da die Rh-Spitze eine höhere Dichte von niedrig koordinierten Kanten- und Kinkatomen als die Rh-Folie aufweist.

Oszillationen können auftreten, wenn die Reaktion bistabil ist und wenn eine Rückkopplung existiert, welche die periodischen Wechsel zwischen den zwei Zuständen steuert. Im Falle der H₂-Oxidation auf Rh ist die Ursache der Bistabilität bekannt, jedoch verbleibt die Frage nach dem Feedback-Mechanismus. Da die Oszillationen nur auf gestuften Oberflächen beobachtet wurden, liegt die Vermutung nahe, dass die reversible Bildung von subsurface Sauerstoff als Feedback-Mechanismus dienen könnte. Unsere PEEM-Beobachtungen zeigen, dass kollidierende Wasserstofffronten innerhalb der Domänen der Rh-Folie Regionen ausbilden, welche auf PEEM-Bildern als „helle Streifen“ sichtbar sind. Da die Einlagerung von Sauerstoff unter die Rh-Oberfläche die lokale Austrittsarbeit reduziert, kann die Beobachtung der hellen Streifen als starkes Indiz für die Bildung von subsurface Sauerstoff angesehen werden. Daher unterstützt die Beobachtung der Ausbildung der hellen Streifen die These, dass die reversible Bildung von subsurface Sauerstoff als Feedback-Mechanismus der Oszillationen in der H₂-Oxidation auf Rh dient.

Abstract

The catalytic H₂ oxidation on high-Miller-index rhodium surfaces was studied in the 10⁻⁶ mbar pressure range using a polycrystalline Rh foil consisting of differently oriented μm-sized domains as a sample and the photoemission electron microscope (PEEM) as imaging tool. A polycrystalline Rh foil was chosen as model catalyst for this study since the high-Miller-index domains of such a foil exhibit structural similarities to the stepped surfaces of Rh nanoparticles used in commercially supported catalysts.

The general concept of this study is based on the relationship between the local activity of the catalyst surface and the corresponding PEEM image intensity, which both depend on the coverage of the adsorbed species (*kinetics by imaging* approach). Applying this approach allows to register kinetic transitions from the inactive state to the catalytically active state and vice versa by monitoring the reaction *in situ* by PEEM. Such transitions are accompanied by the observable nucleation and propagation of reaction-diffusion fronts. Under certain conditions chemical waves and oscillation patterns can also form on the surface.

PEEM observations of such transitions show, that hydrogen fronts nucleate on defects within individual domains as well as on the domain borders and that the local surface structure influences the front propagation. Artificial defects, which were created by Ar⁺ sputtering, partially equalise the different surfaces of the individual domains and thus also reduce the front propagation anisotropy, which is characteristic for particularly oriented domains.

In contrast to the CO oxidation reaction, the unhindered spreading of reaction fronts across domain borders was observed. The observed propagation of hydrogen across grain boundaries couples the catalytic behaviour of the differently oriented domains, i.e. the changes of the local PEEM intensity occurring during the cyclewise variation of p_{H_2} at constant p_{O_2} and at a constant temperature reflect the kinetic behaviour of the whole sample surface. The results obtained by monitoring the kinetic transitions by PEEM have been summarised in a kinetic phase diagram, which characterises the catalytic behaviour of the polycrystalline Rh sample in a broad parameter range. Analogously, a diagram for the additionally Ar⁺ sputtered Rh foil was constructed. The comparison of these two diagrams reveals, that the additional sputtering shifts the diagram towards lower hydrogen pressures, i.e. the Ar⁺ sputtering increases the tolerance of the catalyst surface towards oxygen poisoning.

In a narrow parameter range, a unique multifrequential self-sustained oscillating behaviour of the H₂ oxidation on the Rh foil was observed. The reaction exhibits coupled oscillations on different domains, which form complex structures on the whole sample surface. Summarising the spatial distribution of the frequencies in a frequency map lead to the insight, that the frequencies differ on different domains although the reaction fronts forming the oscillation patterns propagate across grain boundaries. Correlating the frequency map with the electron backscatter diffraction map (EBSD map), which provides information about the crystallographic orientations of the individual domains, reveals that the oscillation frequency is higher on vicinal *Rh*(1 1 0) surfaces, which exhibit a higher density of low coordinated step and kink atoms, than on generally smoother vicinal *Rh*(1 1 0) surfaces. The observed oscillation patterns consist mainly of spiral-shaped waves which overlap with each other. Like other reaction fronts, these spirals also spread unhindered across grain boundaries. PEEM observations of a single spiral spreading across three different domains revealed, that the width, the radius and the velocity of the spreading wave change abruptly when crossing grain boundaries. This observation lead to the conclusion, that the propagation behaviour of the hydrogen fronts strictly depend on the local surface structure.

To prove the role of the surface structure in the appearance of self-sustained oscillations in the H₂ oxidation on Rh, the behaviour of the reaction on the surface of a *Rh*(1 1 1) single crystal containing a mesoscopic furrow-like defect was studied. The corresponding PEEM observations demonstrated, that the reaction oscillates within the defect while on the smooth single crystal surface no oscillations were observed. AFM measurements revealed that the side walls of the 30 μm wide and 1 μm deep defect consist of highly stepped surfaces. This result confirms, that structural limits exist which determine the existence range of oscillations. The factors which govern the oscillating behaviour are, apart of the external reaction conditions, the orientation of the terraces, the width of the terraces and the roughness of the step edges.

The domains of the polycrystalline Rh foil consist of similarly stepped surfaces as those of nanoparticles used in commercial catalysts, however their sizes differ significantly. To prove the contribution of a possible size-effect, the obtained results are compared with those of an FEM study, where the catalytic H₂ oxidation was studied on the extremely curved and thus highly stepped surface of an apex of a Rh nanotip. The comparison of the kinetic phase diagrams for the Rh foil with that for a Rh tip shows, that the tip surface exhibits generally a higher tolerance towards oxygen poisoning than the annealed and the additionally Ar⁺ sputtered Rh foil. The oscillations in the H₂ oxidation, which

were also observed on the nm-sized Rh sample, occur on the tip with a higher frequency than those on the domains of the Rh foil. These observations are in agreement with the results for the Rh foil, since the surface of the highly curved apex of the nanotip exhibits a higher density of low coordinated step and kink sites than the domains of the present Rh foil.

Since the self-sustaining oscillations can occur if a bistable behaviour of the reaction and a feedback mechanism, which governs the periodic transitions between the two steady states, exist, a proper feedback mechanism for the observed oscillations has to be found. The present observations of the oscillations in the H₂ oxidation which take place solely on the stepped and kinked surfaces suggest the formation and depletion of subsurface oxygen as a feedback mechanism. Additional PEEM studies show, that the collisions of hydrogen fronts within the domains of the Rh foil lead to the formation of "bright stripes" within the PEEM images. These regions of low work function can be treated as evidence for the enhanced formation of subsurface oxygen since oxygen atoms incorporated below the sample surface lower the work function. This supports the suggestion about the subsurface oxygen formation as feedback mechanism for the observed oscillations.

Acknowledgements

I would like to express my thanks to all the people who have supported me during my Ph.D. studies. Particularly I would like to thank...

... my supervisor **Prof. Yuri Suchorski**, who always took the time to guide me since I started to work in his group as a trainee.

... my colleagues **Dr.rer.nat. Ivan Bespalov MSc, Dipl.-Chem.(FH) Sebastan Buhr, Johannes Zeininger BSc, Clara Freytag and Philipp Winkler BSc** for the fruitful collaboration and a really great time.

... **Prof. Günther Rupprechter**, the head of the IMC, who enabled me to work at his institute.

... the **Fonds zur Förderung der wissenschaftlichen Forschung (FWF)** and in particular the Special Research Program „Functional Oxide Surfaces and Interfaces“ (SFB F45 „FOXSI“) for financially supporting my research.

... **Johannes Frank** for his technical support concerning the experimental setup.

... **my family** for always supporting me during my studies with the various things I needed.

... **my friends** for their moral support.

... **Angelika**, for more than words could ever say.

Table of Contents

1	General introduction to catalysis	4
1.1	The working principle of catalysts	4
1.2	The role of catalysis in reshaping economy and society	6
1.3	Current challenges in improving catalytic systems	8
1.4	Outline of this thesis	10
2	The catalytic hydrogen oxidation reaction on rhodium	11
2.1	The hydrogen oxidation reaction	11
2.1.1	The catalytic hydrogen oxidation reaction on rhodium	12
2.2	Interaction of oxygen and hydrogen with rhodium	13
2.3	Bistability in and the kinetic phase diagram of the hydrogen oxidation . . .	15
2.4	Self-sustaining oscillating behaviour of catalytic reactions	16
2.4.1	Oscillations in the carbon monoxide oxidation on platinum group metals	17
2.4.2	Oscillations in the hydrogen oxidation on platinum group metals . .	19
3	Experimental	22
3.1	The ultrahigh-vacuum system	22
3.1.1	The PEEM-chamber	25
3.1.2	The XPS-chamber	27
3.1.3	The load lock	27
3.2	Methods	30
3.2.1	Photoemission Electron Microscopy	30
3.2.1.1	The photoeffect	30
3.2.1.2	Working principle of the PEEM	31
3.2.1.3	Layout of a UV-PEEM	33
3.2.1.4	The kinetics by imaging approach	34
3.2.2	Quadrupole Mass Spectrometry	35

Table of Contents

3.2.3	X-ray Photoelectron Spectroscopy	37
3.2.4	Electron backscatter diffraction	44
3.2.5	Atomic force microscopy	45
3.3	The catalytic systems	46
3.3.1	Rhodium	47
3.3.2	The rhodium model catalysts	47
4	Experimental results	50
4.1	Bistability and steady states of the hydrogen oxidation on the polycrystalline rhodium foil	51
4.1.1	Nucleation and propagation of hydrogen reaction fronts	51
4.1.2	Bistability and kinetic phase diagrams	57
4.2	Spatio-temporal oscillations in the hydrogen oxidation on pure rhodium	61
4.2.1	PEEM observation of the spatio-temporal oscillations in the hydrogen oxidation on the polycrystalline rhodium foil	61
4.2.2	The role of the surface structure in the oscillation frequency	62
4.2.3	The formation of the oscillation pattern	66
4.2.4	Guiding oscillations through geometry	69
4.2.5	Structural limits for the existence of oscillations	71
4.3	Spatio-temporal behaviour of the catalytic hydrogen oxidation on different scales	75
4.4	The feedback mechanism of the oscillating hydrogen oxidation on pure rhodium	81
4.4.1	Lowering of the local work function during the catalytic hydrogen oxidation on polycrystalline rhodium	81
4.4.2	The proposed feedback mechanism	83
5	Conclusions	87
	List of figures	90
	List of tables	92
	References	93
	Publications	102

Table of Contents

Curriculum vitae

108

1

General introduction to catalysis

Before the importance of catalysis for industrial branches and for environmental causes is discussed, the working principle of a catalyst, namely lowering the activation energy of a certain chemical reaction, is briefly addressed in 1.1. Also, the relationship of activation energy and reaction kinetics is shortly described using the Arrhenius equation.

The necessity of studying and optimising catalytic processes is addressed in 1.2 by discussing examples illustrating how the development of catalysts changed industrial processes as well as the daily life of mankind.

Further improving existing catalysts and developing new catalysts, which can face upcoming challenges, requires a detailed knowledge about the relevant steps of the catalysed reaction. Obtaining such new insights into the elemental steps of catalytic processes by studying commercially used catalysts under industrial conditions is hardly possible since too many unknown, or at least indistinguishable, factors might influence the catalytic activity. Therefore, less complex model systems are usually studied under controlled conditions (e.g. in high vacuum) to obtain fundamental insights on the role of only one (or a few) of these factors. Afterwards, the complexity of the studied model systems can be increased systematically towards commercial catalysts. This frequently used approach is addressed in 1.3.

Finally a brief outline of the thesis is given in 1.4.

1.1 The working principle of catalysts

Jakob Berzellius was the first one defining the term *catalysis* in 1835 [1] although catalytic processes might have influenced the life of mankind at least since 7000 B.C. The production of a mixed fermented beverage of rice, honey and fruit in an early Neolithic village of Jiahu in Henan province in China is one of the oldest confirmed applications of catalytic processes [2]. During the ages, the applications of catalysis became more and more sophisticated, but the working principle of a catalyst still remains the same: the

1 General introduction to catalysis

catalyst reduces the activation energy E_A by altering the reaction mechanism although it is not consumed during the reaction.

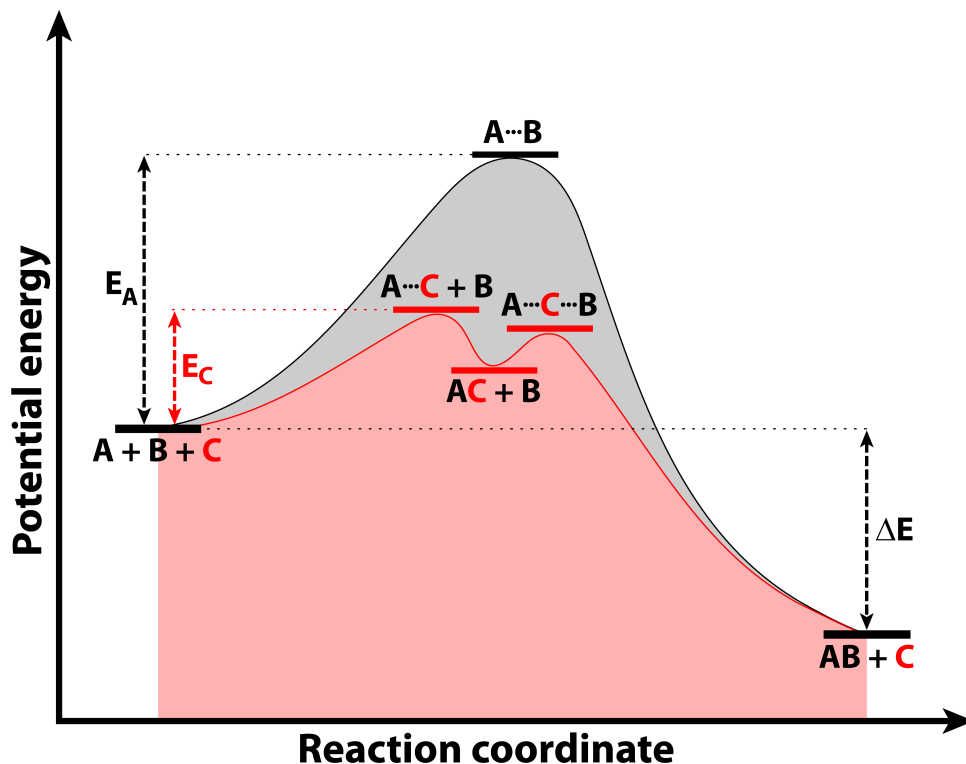


Fig. 1.1. Energy diagram of the chemical reaction $A + B \rightarrow AB$ without (gray) and with (red) a proper catalyst: The use of the catalyst alters the reaction pathway (by forming intermediates) and thus reduces the activation energy E_A to E_C .

As illustrated in Fig. 1.1, an exemplary chemical reaction $A + B \rightarrow AB$ requires overcoming E_A to process the two reagents A and B to the product AB , although the exothermic reaction releases the energy ΔE . The necessary activation energy can be reduced by using the catalyst C and thus altering the reaction mechanism by forming two new transition states ($A \cdots C$ and $A \cdots C \cdots B$) and a new intermediate product (AC). The modified reaction pathway requires the activation energy E_C , which is lower than E_A .

The change in the reaction rate resulting from this lowering of the activation energy can be described using the Arrhenius equation

$$k = A \cdot e^{-\frac{E_A}{k_B T}} \quad (1.1)$$

where k is the reaction rate, A is a pre-exponential factor, E_A is the activation energy, T is the temperature and k_B is the Boltzmann constant. The relationship between k and E_A

illustrates that under isothermal conditions even a small decrease of the activation energy might lead to a significant increase of the reaction rate.

Thus at the present day, many industrial branches depend on catalysts since their use significantly decreases the production efforts as well as the production costs. While in 2015 the global catalyst market size was approximately 6.65 kilo-tons [3], its global value will, according to a forecast, soon exceed 34.3 billion \$ [4]. Such a progress also results from scientific contributions to the field of catalysis.

1.2 The role of catalysis in reshaping economy and society

Most scientific achievements in history resulted from the attempts of solving actual problems in economy or society. This was also the case at the beginning of the 19th century, when probably the first observation of a heterogeneously catalysed reaction was published [5]. Humphry Davy addressed himself to the problem, that accidents in coal mines caused by the explosion of methane in the presence of a naked flame became more frequent annually, particularly in the north of England. In 1815 he finished developing a safety lamp, which helped to detect methane in coal mines without endangering the coal miners by a naked flame [5]. Further studies and improvements of his 'Davy lamp' led him to the insight, that methane and oxygen do not necessarily need a gas phase (a flame) for the reaction, since a glowing Pd or Pt wire can also provide the reaction on the surface, i.e. catalyse it. His work, published in 1817 [6], is probably one of the first clear evidences, that a solid surface can enable the reaction of reactants, which do not react with each other in the gas phase. Since these days, the field of heterogeneous catalysis has greatly evolved.

A milestone in the history of heterogeneous catalysis was the development of the ammonia synthesis, which saved Europe's population from mass starvation at the beginning of the 20th century. At that time it was already known, that fertilizers based on ammonia could increase the fertility and consequently the agricultural earning, but the common production method for ammonia, namely mining, could not satisfy the growing demand of fertilizers necessary for dealing with the enormous increase of Europe's population [7]. The solution for the supply problem of ammonia was provided by the development of the Haber-Bosch process, which enabled the production of ammonia, and thus also of fertilizers, at an industrial-scale [8]. The basic idea of Haber was to produce ammonia using the

1 General introduction to catalysis

nearly infinite supply of atmospheric nitrogen. Although the extremely strong triple bond in elemental nitrogen makes N_2 quite unreactive, Haber found a way to force atmospheric nitrogen to react with hydrogen within a flow reactor at high pressure and temperature conditions in the presence of an osmium catalyst [9]. This idea was enhanced by Carl Bosch who scaled the ongoing processes up to an industrial level of production and thus ensured that the increasing demand of ammonia for the production of fertilizers could be satisfied. This development was also honoured with two Nobel Prizes (Fritz Haber in 1919 and Carl Bosch in 1931). Without the development of the Haber-Bosch process the exponential growth of the world ammonia production from a few 100.000 tons at the beginning of the 19th century to about 211 million tons in 2013, which are mainly used for the production of fertilizers, would have hardly been possible [10, 11].

Catalysts also became part of the daily life of millions of people - even though probably many of them are not aware of it. A prime example is the three-way automotive catalytic converter, which was developed in 1973, 88 years after Carl Benz developed the first car. Within this period, in which exhaust gases were not treated, the amount of harmful emissions increased significantly due to the growing number of used cars. Since at the end of the 1960s car emissions of toxic CO reached levels of approximately 60 *g/km* per car [12], urban air quality problems became urgent. This situation significantly improved in the 1980s, when the use of the three-way converter was established [13]. This converter placed in the tailpipe of a combustion engine catalyses the oxidation of carbon monoxide and unburnt hydrocarbons to carbon dioxide and water as well as the transformation of nitric oxides and carbon monoxide to nitrogen and carbon dioxide. Further improvement of the three-way automotive catalytic converter enabled the reduction of car emissions of CO by approximately 98.3 % to values below 1 *g/km* [12].

Nowadays the goal switched towards entirely avoiding harmful emissions in power generation instead of only reducing them. For instance, a fuel cell generating electricity from oxidising H_2 can fulfil this objective, if air is used as source for the necessary oxygen and H_2 is produced in an environmentally friendly way without emitting harmful pollutants, e.g. using wind, solar or geothermal power. To enable the replacement of common combustion engines, the fuel cell technology needs to be exploited, but therefore a detailed knowledge of the processes occurring within a fuel cell is required. Numerous recently published papers addressing these processes, for example Refs. [14–17], illustrate the importance of studies directed to obtain this necessary knowledge.

1.3 Current challenges in improving catalytic systems

In the past the primary goal of catalytic research, namely altering the reaction kinetics by decreasing the activation energy of the catalysed reaction, was often reached by applying the trial and error principle, where different mixtures of probably suitable compounds were tested until a new composition exhibiting an improved catalytic behaviour was found. This screening approach, which led to the development of several catalysts which are still used, seemed to be a suitable procedure since mostly selectivity towards the favoured product was not as important as nowadays. A prime example for present days need of selectivity is the modern pharmaceutical industry, where unwanted byproducts could entail serious harm. For further increasing the selectivity of catalysts, nowadays it is necessary to understand the elementary steps of the occurring reactions leading to the desired product and to byproducts. Thus contemporary research has to gain fundamental insights into these competitive processes.

As already mentioned, studying commercially used catalysts, which usually consist of oxide supported metallic nanoparticles exhibiting differently oriented nanofacets, under real (high) pressure conditions can hardly lead to a detailed understanding of the ongoing processes, since the possible interplay of too many factors influences the catalytic behaviour of the studied reaction system. Differences in the surface structure such as the crystallographic orientation or the roughness of the surface, the composition of the gas phase, the temperature range, interactions between the catalytically active particles with the support or the influence of the particle size serve as good examples for such parameters. Therefore, in contemporary research less complex model systems are applied to study only one of the various factors which could influence the catalytic reactivity [18]. This scientific path was pioneered by Langmuir in the 1920's [19, 20] and rewarded by the Royal Swedish Academy of Sciences as Prof. Gerhard Ertl was honoured with the Nobel Prize in Chemistry in 2007 "for his studies of chemical processes on solid surfaces" [21]. Such a simplification can, for example, be achieved by decreasing the complexity of the surface and the gas phase. A model catalyst can be simplified until a well-defined surface, such as that of a single crystal, is reached. Apart from that, the amount of residuals within the gas phase can be reduced by performing the experiments in ultra-high vacuum (UHV). Combining both simplifications, enables the use of various surface-sensitive techniques to characterise and analyse the sample and the ongoing reaction. On the other hand, such a kind of simplification can be criticized since the reaction conditions significantly differ from real catalytic systems and thus probably the obtained results can hardly be trans-

ferred to real systems. For example, effects such as mass or heat transfer through the gas phase can play an important role in industrial approaches but are almost neglectable in UHV. Also, low-index single crystal surfaces composed of wide terraces perform differently than oxide supported particles which are enclosed by high-Miller-index facets. The differences resulting from the simplification of the reaction system are known as 'materials gap' and 'pressure gap', but since the scientific community is aware of these gaps and of the problems concerning studying modern catalysts under realistic conditions, there are efforts trying to bridge the materials and the pressure gap using e.g. the paths illustrated in Fig. 1.2 [22–25].

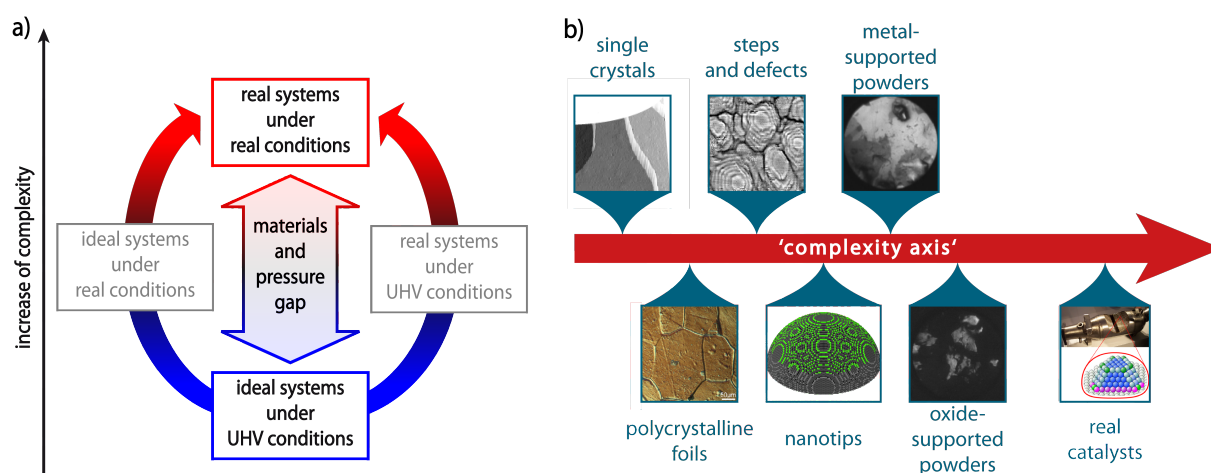


Fig. 1.2. Possible ways of bridging the pressure and materials gap: a) For bridging the gaps first the processes occurring within the simplified system need to be understood. b) The materials gap can be attempted to be overcome by following the "complexity axis".

After the ongoing processes occurring within a simplified model system, e.g. a single crystal under UHV conditions, are understood, closing the gaps can be attempted by either bringing the gas phase complexity closer to realistic conditions or increasing the complexity of a model system, as shown in Fig. 1.2a. For example one possible way of bridging the materials gap is following the steps marked in the "complexity axis", shown in Fig 1.2b.

The study presented in this thesis contributes to the effort of bridging the materials gap. Considering knowledge obtained in the past, which is partially discussed in the chapters 2 and 3, new insights in the factors influencing the spatio-temporal behaviour of the catalytic hydrogen oxidation on high-Miller-index rhodium surfaces could be obtained by studying the ongoing reaction on a polycrystalline Rh foil. Further, the influences of the surface roughness and the size of the catalyst are addressed.

1.4 Outline of this thesis

The present thesis is structured in five chapters. In the first chapter, a brief overview about the working principle of catalysts, the importance of catalysis for industry and the challenges in improving existing catalysts and developing new catalysts was given.

The second chapter provides an overview about the catalytic hydrogen oxidation on rhodium and the interaction of hydrogen and oxygen with differently oriented Rh surfaces. The reaction mechanism of the catalytic H₂ oxidation on Rh is discussed as well as the adsorption properties of the reactants. Also adsorbate induced reconstructions of different Rh surfaces are addressed. Afterwards, the bistable behaviour of the studied reaction and chosen examples of oscillating behaviour are treated.

The experimental setup used for nearly all experiments presented in this thesis is introduced in the third chapter. Afterwards the applied techniques are discussed before the studied Rh model catalysts, namely a polycrystalline Rh foil and a *Rh*(111) single crystal, are presented.

The fourth chapter addresses the experimental results obtained using PEEM. In the first section of this chapter, results concerning the bistable regime of the catalytic H₂ oxidation on the Rh foil are discussed. Then, the nucleation of reaction fronts and the influence of both, grain boundaries and the local surface structure on the reaction front propagation are addressed. The following analysis of the catalytic behaviour of the additionally Ar⁺ sputtered foil enables discussing the influence of the surface roughness on the catalytic activity of the catalyst. In the second section of the fourth chapter, spatio-temporal oscillations in the H₂ oxidation on Rh are presented. Features like the influence of the local surface structure on the local oscillation frequency or the origin of distinct patterns, which occur on differently oriented domains of the Rh foil, are discussed. The *Rh*(111) single crystal was used to verify the results concerning the above mentioned relationship between the surface roughness and the oscillation frequency. Within the third section, the H₂ oxidation on the Rh foil is compared with the behaviour of this reaction on a Rh-nanotip. In the last section, PEEM observations, which lead to a suggestion for a feedback mechanism of the oscillating H₂ oxidation on Rh, are discussed as well as the proposed feedback mechanism itself.

Finally, the most important results of this thesis are summarised in the fifth chapter.

2

The catalytic hydrogen oxidation reaction on rhodium

In section 2.1 the first commercial use of the catalytic H_2 oxidation as well as nowadays demands for hydrogen based technology are mentioned. Afterwards the Langmuir-Hinshelwood mechanism of the catalytic hydrogen oxidation reaction on Rh is briefly discussed.

The adsorption and desorption properties of hydrogen and oxygen are addressed in section 2.2 as well as adsorbate induced reconstructions of Rh surfaces.

Section 2.3 treats the bistable behaviour of the catalytic H_2 oxidation and possibilities to characterise bistable reaction systems in a broad parameter range.

Finally, a literature overview concerning the oscillating CO oxidation and H_2 oxidation on Pt group metals is given in section 2.4.

2.1 The hydrogen oxidation reaction

H_2 and O_2 can form H_2O either via the gas phase reaction or via a heterogeneously catalysed reaction. Dealing with the gas phase reaction entails enormous risks since even small mistakes in the handling can shift the kinetics of the ongoing exothermal reaction towards explosive regimes [26]. Thus, mainly the well controlable (and thus far less dangerous) catalytic H_2 oxidation is used in technological approaches.

The first commercial use of the catalytic H_2 oxidation was the Döbereiner's lighter, which was developed in 1823 [27]. Within this device, H_2 is generated from sulfuric acid reacting with zinc while the necessary oxygen is provided from the atmosphere. When the produced H_2 stream flows through a Pt sponge, which is exposed to air, the H_2O production is catalysed. Since this process is exothermic, the Pt sponge heats up and finally ignites the mixture of gases.

Since that time, the importance of the catalytic H_2 oxidation significantly increased.

2 The catalytic hydrogen oxidation reaction on rhodium

Nowadays, it might even be part of the answer to one of the major challenges we have to face, namely the anthropogenic-driven climate change and its relationship to future energy demands [28]. A possible way to cope with this task would be to switch from carbon-based (fossil fuel) to hydrogen-based energy systems. Today, the catalytic H_2 oxidation is only used in relevant amounts for power and heat generation via fuel cells in surroundings where using common combustion engines would have significant drawbacks. For example in space technology fuel cells provide electricity and water, which may serve as drinking water after a special treatment [29] while fossil fuel combustion engines would only consume oxygen without producing a useful product. On the other hand, the sector of renewable energy generation grows in the power industry sector [30]. Also the automotive industry pursues the objective of reducing the harmful gas emissions of the used engines and thus tries to implement the fuel cell technology on the market [30]. However, there is still a long way to go and present-day research has to overcome multiple scientific and technological challenges to create the prerequisites necessary for reaching the goal of shifting the global carbon-based energy economy towards a clean and renewable economy based on hydrogen [28].

2.1.1 The catalytic hydrogen oxidation reaction on rhodium

The catalytic H_2 oxidation on Rh follows the Langmuir-Hinshelwood mechanism [31, 32], i.e. both reactants first have to adsorb on the sample surface, before the product can be formed. This reaction pathway, which is illustrated in Fig 2.1, can be described using the following equations, where $*$ represents an unoccupied adsorption site.



Both, O_2 and H_2 adsorb dissociatively on two free adjacent adsorption sites on the Rh surface (2.1, 2.2). The more loosely bound hydrogen can afterwards diffuse towards the

more strongly bound oxygen and form the intermediate OH (2.3). In the following, H_2O can be produced by two different reaction paths. Either two OH molecules react with each other leaving a single oxygen atom (2.4) or an OH molecule reacts with a hydrogen atom and thus creates a free adsorption site (2.5). Finally, water leaves another free adsorption site behind when it desorbs from the sample surface (2.6).

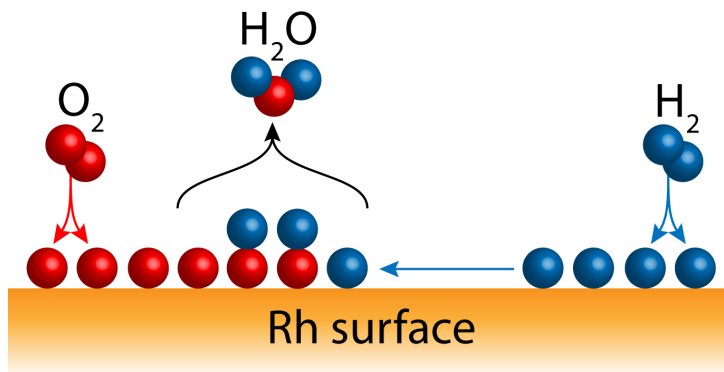


Fig. 2.1. Schema of the Langmuir-Hinshelwood mechanism of the catalytic H_2 oxidation on Rh: After the dissociative adsorption of O_2 and H_2 , first the intermediate OH is formed before H_2O can be produced and finally desorbs from the sample surface.

2.2 Interaction of oxygen and hydrogen with rhodium

Adsorbing species may form certain super-structures, which usually depend on the total coverage and the temperature. Sometimes adsorbats may even change the surface structure via inducing (or lifting) reconstructions or oxidising (or reducing) the sample surface. While under the studied reaction conditions ($433\text{ K} \leq T \leq 493\text{ K}$) the adsorbed hydrogen desorbs from the sample surface nearly immediately [33–37], oxygen remains on the sample surface [38–40]. Thus in the following only chosen adsorption phases for oxygen and the influence of adsorbed oxygen on the surface structure are discussed and summarised in Tab. 2.1.

At 130 K adsorbing oxygen forms on $\text{Rh}(100)$ surfaces at a total coverage Θ_{O} of 0.25 ML a (2×2) superstructure which undergoes a "clock" reconstruction at Θ_{O} of 0.5 ML [41, 42]. On $\text{Rh}(110)$ oxygen can adsorb between 125 and 300 K at Θ_{O} of 1 ML in a $(1 \times 2)\text{p}2\text{mg}$ pattern, and at Θ_{O} of 0.5 ML above 470 K in a $(2 \times 2)\text{p}2\text{mg}$ array [43]. Further, at 390 K and Θ_{O} of 0.7 ML , adsorbed oxygen can also form a (2×10) superstructure [44, 45] while at 620 K , oxygen adsorbs after an exposition of 5 L as (1×2) , $\text{c}(2 \times 6)$ or as $\text{c}(2 \times 8)$ array [46]. Up to 480 K Rh can reconstruct at $\Theta_{\text{O}} \leq 1\text{ ML}$ in $(1 \times n)$ phases with $2 \leq n \leq 5$

2 The catalytic hydrogen oxidation reaction on rhodium

Table 2.1. Adsorption phases for oxygen on Rh and oxygen induced reconstructions of Rh surfaces

Surface	T	Θ_O	Pattern	Reconstruction	Ref.
<i>Rh</i> (1 0 0)	130 <i>K</i>	0.25 <i>ML</i>	(2×2)	-	[41]
<i>Rh</i> (1 0 0)	130 <i>K</i>	0.25 <i>ML</i>	(2×2)	-	[42]
<i>Rh</i> (1 1 0)	125 – 300 <i>K</i>	1 <i>ML</i>	(1×2)p2mg	-	[43]
<i>Rh</i> (1 1 0)	> 470 <i>K</i>	0.5 <i>ML</i>	(2×2)p2mg	-	[43]
<i>Rh</i> (1 1 0)	390 <i>K</i>	0.7 <i>ML</i>	(2×10)	-	[44, 45]
<i>Rh</i> (1 1 0)	620 <i>K</i>	-	-	(1× <i>n</i>) with <i>n</i> = 2, 6, 8	[46]
<i>Rh</i> (1 1 0)	< 480 <i>K</i>	≤ 1 <i>ML</i>	-	(1× <i>n</i>) with 2 ≤ <i>n</i> ≤ 5	[47]
<i>Rh</i> (1 1 1)	320 <i>K</i>	0.25 <i>ML</i>	(2×2)	-	[40]
<i>Rh</i> (1 1 1)	320 <i>K</i>	0.25 – 0.5 <i>ML</i>	(1×2)	-	[40]
<i>Rh</i> (3 3 2)	430 – 510 <i>K</i>	0.1 – 0.6 <i>ML</i>	-	step-doubling	[48]

(i.e. each n^{th} $[1\bar{1}0]$ row is missing) [47]. On the *Rh*(1 1 1) surface oxygen can adsorb at 320 *K* at Θ_O of 0.25 *ML* as (2×2) O-adlayer, while a Θ_O between 0.25 and 0.5 *ML* lead to the (1×2) phase [40].

Besides the low-Miller-index Rh surfaces, also high-index surfaces may reconstruct due to the adsorption of oxygen. An example is the *Rh*(3 3 2) surface, which doubles its step height between 430 and 510 *K* if Θ_O is between 0.1 and 0.6 *ML* [48]. One possibility to lift this reconstruction is annealing at 1000 *K*.

However, co-workers from the working-group I participate in studied the H₂ oxidation on Rh *in situ* using FIM and FEM. Recently they could show, that none of the differently oriented facets of the studied Rh tip reconstructs under the same reaction conditions, which were applied during the study presented within this thesis. Further details concerning these studies are addressed in section 4.3.

Summarising this overview can be said, that Rh surfaces can reconstruct due to oxygen adsorption, but that the co-adsorption of hydrogen seems to inhibit this process - at least under the studied reaction conditions.

2.3 Bistability in and the kinetic phase diagram of the hydrogen oxidation

Since the H_2 oxidation on Rh follows the Langmuir-Hinshelwood mechanism, both hydrogen and oxygen need to adsorb on the sample surface to produce H_2O . If the set reaction conditions cause a preferential adsorption of H_2 , the sample surface remains almost adsorbate free because hydrogen either desorbs nearly immediately after adsorbing or it reacts with an adsorbed oxygen atom to OH. In the following water is produced, which also desorbs nearly immediately after its formation. In this steady state, oxygen can not cover the surface since adsorbing oxygen is almost instantly reacted off. Thus the reduced, nearly adsorbate free surface is catalytically active. In turn, the preferred adsorption of oxygen leads to a dense oxygen coverage that inhibits the adsorption of hydrogen and thus also the formation of H_2O . This catalytically inactive state is also called "poisoned".

The inequivalence in the adsorption properties of the reactants lead to the bistable behaviour of the catalytic H_2 oxidation on Rh, i.e. the system can be under identical parameters, such as temperature and partial pressures, in two different states of catalytic reactivity [49]. Catalytic transitions from one steady state to the other one are typically manifested by a change of the surface coverage via propagating reaction fronts.

If the partial oxygen pressure p_{O_2} and the temperature are held constant while the partial hydrogen pressure p_{H_2} is varied cyclewise, the bistability is reflected in the hysteresis-like behaviour of the reaction rate, which is schematically shown in Fig. 2.2a and b. Starting at the left bottom part of the hysteresis loop, an increase of p_{H_2} leads to a sudden increase of the H_2O production rate at a certain temperature dependent proportion of p_{H_2} and p_{O_2} . This proportion is called transition point τ_A . Decreasing p_{H_2} after this kinetic transition from the poisoned state to the catalytically active state leads to the reversed transition back to the inactive state. This transition takes place at the kinetic transition point τ_B , which occurs at a significantly lower p_{H_2} than τ_A . This difference originates from the blocked adsorption of H_2 by the dense oxygen coverage and is reflected by the width of the loop.

Each measured hysteresis characterises the reaction system at a certain temperature by revealing the region of high activity, low activity and bistability, where the system can be in either of both states - depending on the prehistory of the sample, i.e. depending from which side this area is entered. The transition points obtained from multiple hysteresis-measurements performed at different temperatures but at the same p_{O_2} can be used to

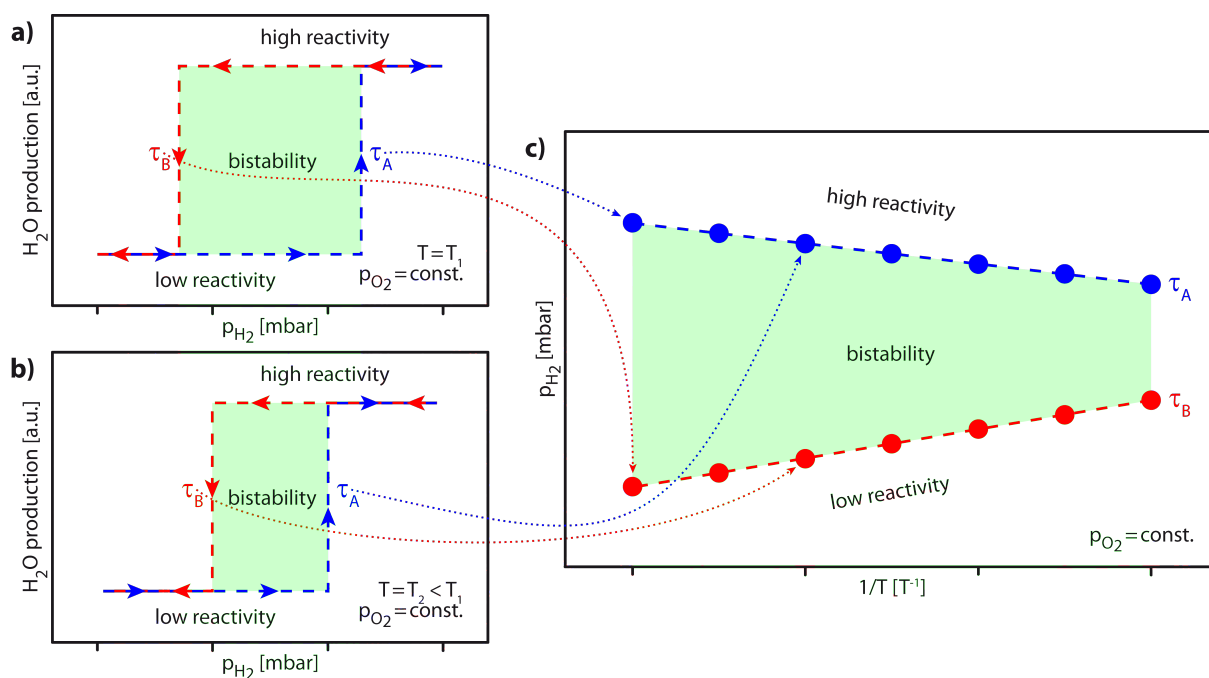


Fig. 2.2. Construction of a kinetic phase diagram: a) Schematic hysteresis loop of the reaction rate at constant p_{O_2} and T , b) The same as (a) but at a different temperature, c) Schematic kinetic phase diagram constructed from kinetic transition points τ_A and τ_B .

plot a kinetic phase diagram in the (p_{H_2}, T) -parameter space. As shown in Fig. 2.2c, such a kinetic phase diagram characterises the catalytic behaviour of a sample in a broad parameter space.

2.4 Self-sustaining oscillating behaviour of catalytic reactions

The production rates of some chemical reactions can exhibit an oscillating behaviour under stationary external conditions [50]. Such oscillating reactions are studied since the beginning of the 20th century. Already in 1921, the Bray–Liebhafsky reaction, i.e. the oscillating decomposition of hydrogen peroxide, was observed [51], while in 1928, the oscillatory behaviour of an electrochemical reaction, i.e. of the electrodisolution of iron in sulfuric acid solution, was studied for the first time [52]. In the early 1950s, the probably most famous example of an oscillating behaviour, namely the Belousov-Zhabotinski reaction, was discovered [53, 54]. In the field of heterogenous catalysis, oscillations in the catalytic CO oxidation on *Pt* surfaces are studied since the 1970s [55, 56] while oscillations

in the NO reduction on *Pt* are observed since the 1980s [57].

Such self sustaining oscillations may occur if two basic requirements are fulfilled. First, the reaction must exhibit a bistable behaviour and, secondly, a feedback mechanism must exist, which initiates the periodic switches between the two steady states [58]. Beside the academic interest, studying oscillating operation regimes also make sense from a practical point of view since a reaction system exhibiting a non-steady behaviour may perform better than the same system remaining in a steady state regime [59]. Further, the local catalytic activity of such reaction systems can be tuned, e.g. via laser pulses, to fit temporally changing demands [60]. The huge amount of experimental and theoretical efforts, which was spent on this field, results in the knowledge that oscillating reactions are a particular case of the wide class of self-organized phenomena in chemistry, physics, biology and sociology.

In the following, a short literature overview is given, which treats chosen examples of oscillating behaviour.

2.4.1 Oscillations in the carbon monoxide oxidation on platinum group metals

The first study describing the oscillating behaviour of a heterogeneously catalysed reaction was published in the early 1970s and concerned the catalytic CO oxidation on Pt [56]. Insights into the complex processes, which enable the oscillating behaviour of the catalytic CO oxidation, were obtained by studying the periodic change of the reaction rate [61], surface-structural transformations [62] or the local work function [63]. Such studies were performed not only on various Pt but also on Pd single crystal surfaces and on Pt nanotips [64–66]. Further, self-sustained kinetic oscillations in the CO oxidation on supported catalysts, such as silica-supported Pt, were studied [67].

As already mentioned above, a reaction can only oscillate if it exhibits a bistable behaviour and if a feedback mechanism exists. In the following, the origin of the bistability of the CO oxidation on Pt group metals and the corresponding feedback mechanisms for the *Pt*(110) and the *Pt*(100) surface, which are both based on reconstructions of the Pt surfaces, are briefly discussed. Finally, the formation of subsurface oxygen, which serves on the *Pd*(110) surface as feedback mechanism is addressed.

Generally, the catalytic CO oxidation on platinum group metals follows the Langmuir-Hinshelwood mechanism, i.e. both reactants need to adsorb on the sample surface before they can form CO₂. The bistability of the CO oxidation on Pt group metals originates

2 The catalytic hydrogen oxidation reaction on rhodium

from the asymmetric adsorption properties of CO and oxygen. CO adsorbs molecularly on a single adsorption site while oxygen adsorbs dissociatively on two adjacent adsorption sites. Thus CO can always adsorb molecularly on an oxygen covered Pt or Pd surfaces (catalytically active state) while the dissociative adsorption of oxygen is blocked by a dense CO coverage (catalytically inactive state).

The CO_{ad} -induced lifting of the (2×1) phase (missing row reconstruction) serves on $\text{Pt}(110)$ as feedback mechanism, which induces the transition between the active oxygen covered surface and the poisoned CO covered surface. On the oxygen covered (2×1) phase CO adsorbs preferentially and reactively removes the previously adsorbed oxygen by forming CO_2 . In the following, the adsorbed CO lifts the reconstruction, i.e. it transforms the surface to the (1×1) phase. This process leads to a significant increase of the structure-sensitive sticking coefficient of oxygen [68]. Thus, oxygen starts to adsorb preferentially and depletes the remaining CO until the cycle is closed, since the oxygen covered surface again reconstructs to the (2×1) phase [69].

The CO oxidation can also oscillate on the $\text{Pt}(100)$ surface, but in this case the feedback mechanism is based on another type of reconstruction [70]. The clean $\text{Pt}(100)$ surface is generally known to be stable in a quasihexagonal (5×20) structure as long as the coverage of adsorbates, such as CO or oxygen, does not exceed a critical value which depends on the adsorbing species. If several species are adsorbed at the same time, all adsorbates contribute to the "combined coverage" necessary for the transformation from the (5×20) to the (1×1) phase [71]. Since the sticking coefficient of oxygen on the reconstructed surface is so small that it can be neglected, CO adsorbs nearly unhindered on the (5×20) phase until the critical coverage θ_{CO} of 0.5 is reached. At this coverage the back-transformation from the (5×20) to the (1×1) phase is induced. Since the sticking coefficient of oxygen on the (1×1) phase is at least two orders of magnitude higher than on the reconstructed surface, oxygen starts to adsorb and reacts with the previously adsorbed CO. Thus, the combined adsorbate concentration decreases below the corresponding critical value and the cycle is closed since the surface again reconstructs to the (5×20) phase [71].

In turn, on the $\text{Pd}(110)$ the reversible formation of subsurface oxygen serves as feedback mechanism [65]. On the metallic Pd, the sticking coefficient of oxygen is higher than that of CO. Thus oxygen adsorbs preferentially and forms subsurface oxygen since the adsorbed oxygen partially penetrates into the surface. This formation of subsurface oxygen significantly lowers the sticking coefficient of oxygen and thus leads to the preferential adsorption of CO. The adsorbed CO depletes the remaining oxygen from above and from

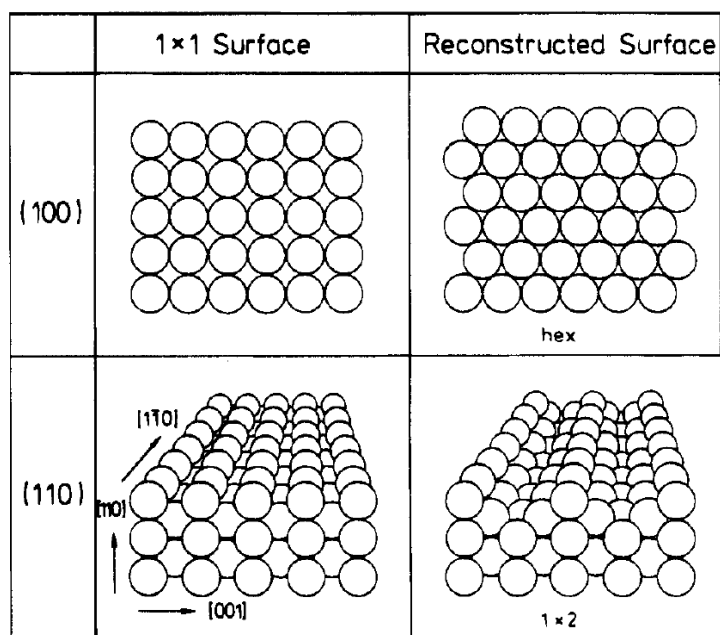


Fig. 2.3. Nonreconstructed and reconstructed Pt surfaces taken from [65].

beneath the sample surface. This process closes the circle since on the reduced surface oxygen again starts to adsorb preferentially.

2.4.2 Oscillations in the hydrogen oxidation on platinum group metals

Besides the CO oxidation, other reactions, such as the H₂ oxidation, can also exhibit an oscillating behaviour on Pt surfaces. For example, oscillations in the H₂ oxidation were studied on a Pt wire and on a Pt foil within a flow reactor at atmospheric pressure. In the case of the wire, oscillations in the temperature of the catalyst and in the production rate were observed [72] while in the case of the foil, the reaction rate, the work function of the metal and optical properties show an oscillating behaviour [73].

Ignition experiments at atmospheric pressure revealed, that the bistability of the H₂ oxidation on Pt is caused by the inhibition of the adsorption of oxygen by the previously adsorbed hydrogen [74]. While below a certain sample temperature adsorbed hydrogen remains on the surface, hydrogen partially desorbs above this temperature and thus enables the dissociative adsorption of oxygen, i.e. the kinetic transition from the catalytically inactive to the active steady state takes place. Cooling the sample afterwards significantly below this temperature leads to the reversed transition back to the inactive hydrogen

2 The catalytic hydrogen oxidation reaction on rhodium

covered phase.

Analogous to the oscillating CO oxidation on Pt, which is described above, the reconstruction of the surface also may serve as feedback mechanism in the oscillating H₂ oxidation on Pt [75]. For example on *Pt*(100), the unhindered adsorption of hydrogen leads to a dense coverage that lifts the quasihexagonal (5×20) structure. Since the sticking coefficient of oxygen is significantly higher on the (1×1) phase than on the (5×20) structure, oxygen starts to adsorb and depletes the remaining hydrogen. This decrease of the combined coverage induces the back-transformation from the (1×1) to the (5×20) phase and thus closes the cycle.

Besides that, the oscillating H₂O production rate in the H₂ oxidation on a polycrystalline Ni film supported by yttria stabilised zirconia at atmospheric pressure is also reported [76]. In this case, the bistability of the H₂ oxidation on the supported Ni is caused by the inhibition of the adsorption of hydrogen by previously adsorbed oxygen [77, 78] while the feedback mechanism is based on the different sticking coefficient of oxygen on Ni and NiO, as explained in the following. The preferential adsorption of oxygen on pure Ni leads under the set reaction conditions to the formation of NiO [76]. In turn, the preferential adsorption of hydrogen on NiO leads to the reduction of the sample surface after the previously adsorbed oxygen has been reactively removed. On the reduced Ni, oxygen adsorbs preferentially again and thus enables the depletion of the remaining hydrogen, which is followed by the oxidation of the surface that closes the cycle.

The oscillating behaviour of the catalytic H₂ oxidation could also be observed on bimetallic model-catalysts, for example on a *Rh*(111) surface alloyed with Ni [79, 80]. In this case, oscillations of the H₂O production rate were observed while periodic changes in the local work function were monitored by PEEM. In this particular case, the feedback mechanism is based on the reversible segregation and oxidation of Ni. Since on the oxygen covered *Rh*(111) surface the segregation of Ni is enhanced, a Ni/Rh adlayer forms, which is stabilised by chemisorbed oxygen. Since the adlayer exhibits a lower sticking coefficient for oxygen than the *Rh*(111) surface, hydrogen starts to adsorb preferentially on the Ni/Rh adlayer. In the following H₂O is formed while the adsorbing hydrogen reduces the previously oxidised surface. Hence the adlayer is destabilised and Ni diffuses back into the bulk. In turn, on the nearly adsorbate free *Rh*(111) surface, oxygen adsorbs preferentially again and thus closes the cycle [79]. Further, the oscillating H₂O production was observed under ambient pressures on silica-supported Rh powder catalysts, which consist of a fine powder (containing Rh and the supporting material) that was pressed into self-supporting discs [81].

2 *The catalytic hydrogen oxidation reaction on rhodium*

Also oscillations in the H₂ oxidation on unsupported, pure Rh were observed, but solely on sharp field emitter tips in high external electric fields ($> 10 \frac{V}{nm}$). In this case, the field stimulated formation of subsurface oxygen serves as feedback mechanism [82]. On the metallic Rh surface, oxygen adsorbs preferentially and incorporates into the bulk under high electric field conditions [83]. Since the formed subsurface oxygen significantly decreases the sticking coefficient of oxygen, the now preferentially adsorbing hydrogen can deplete the previously adsorbed oxygen by forming H₂O. If there is nearly no adsorbed oxygen left, hydrogen starts to pull out the incorporated oxygen. The lowering of the subsurface oxygen concentration leads to the recovery of the sticking coefficient of oxygen. Thus oxygen starts to adsorb again preferentially on the reduced Rh surface and reactively removes the remaining hydrogen. Thereby the cycle is closed, since the oxygen coverage again increases until subsurface oxygen is formed.

To our knowledge, the oscillating behaviour of the H₂ oxidation was yet neither observed on unsupported pure Rh single crystal surfaces nor on pure Rh foils or on the corresponding nanotips under field-free high vacuum conditions.

3

Experimental

The multifunctional ultra-high vacuum (UHV) apparatus, which was used to obtain the results presented in this thesis, is described in 3.1. After a brief overview, different components of the set-up are described in detail.

The working principles of the methods used for studying the catalytic H₂ oxidation on Rh, namely photoemission electron microscopy (PEEM), quadrupole mass spectrometry (QMS) and X-ray photoelectron spectroscopy (XPS), are explained in detail in 3.2, while methods which were solely used to characterise the surface of the model systems, namely electron backscatter diffraction (EBSD) and atomic force microscopy (AFM), are just briefly outlined.

Finally, the model catalysts, namely the polycrystalline *Rh* foil consisting of various differently oriented μm-sized domains and the *Rh*(111) single crystal, are described in 3.3.

3.1 The ultrahigh-vacuum system

The results presented in this thesis were obtained using a multifunctional UHV system with a base pressure of 1×10^{-10} mbar. In the following, the most important parts of the set-up are specified, before the PEEM- and the XPS-chamber as well as the load lock are described in detail.

Figure 3.1 depicts the UHV-system which consists of two separate chambers and the load lock which is placed between the two chambers. The schematic drawing shown in Fig. 3.1a highlights the main devices which were used to obtain the data presented in this thesis while a technical drawing of the apparatus is shown in Fig. 3.1b. In both chambers, namely the XPS-chamber and the PEEM-chamber, the sample can be cleaned by Ar⁺ sputtering and annealing by indirect radiation heating from a filament placed in the back of the sample and by electron bombardment. Type K thermocouples are used to monitor the sample temperature while two quadrupole mass spectrometers are used to monitor the

3 Experimental

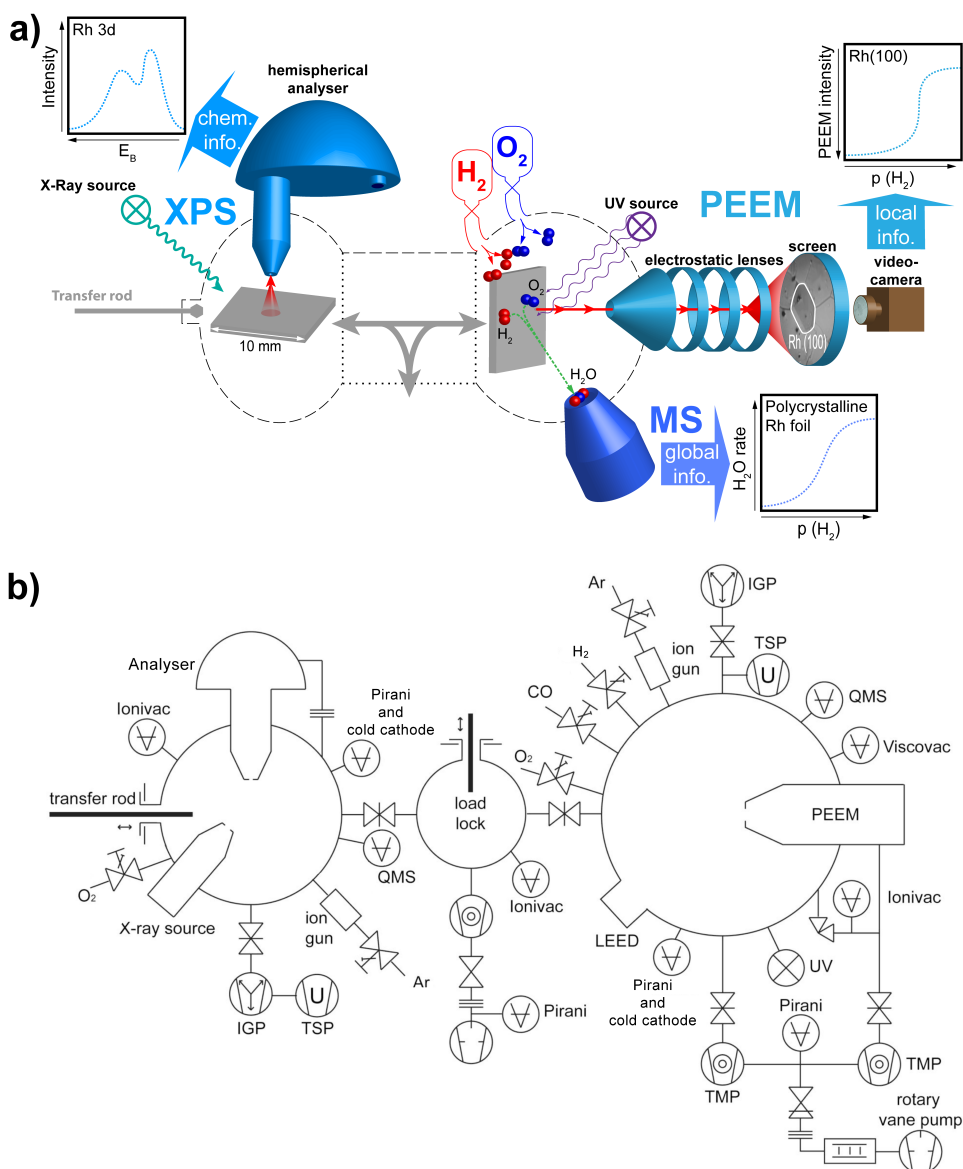


Fig. 3.1. Schematic drawing of the experimental set-up: a) Main parts necessary for characterising the sample using XPS (X-Ray source and hemispherical analyser), transferring the sample along the paths marked as gray arrows (Transfer rod) and studying local and global reaction kinetics of the H_2 oxidation using PEEM and MS (gas supply, UV source, electrostatic lens system, screen, video-camera, mass-spectrometer); b) Technical drawing of the whole apparatus.

gas phases in the two reaction chambers, which can be set using the gas supply systems. This construction enables setting the same conditions in the whole system and therefore allows to carry out measurements in both chambers under the same reaction conditions. The position of the studied samples can be adjusted in both chambers using the mounted manipulators.

3 Experimental

Additionally, the PEEM-chamber, which is used to obtain information about the reaction kinetics for the studied sample, is equipped with a photoemission electron microscope and a water-cooled deuterium discharge UV lamp. In turn, the XPS-chamber is additionally equipped with an X-ray source and a hemispherical electron energy analyser for obtaining chemical information about the sample.

The transfer system is used to move the sample within the UHV-system from one chamber to another, for example from the XPS-chamber to the load lock or to the PEEM-chamber. The gray arrows in Fig. 3.1a indicate the transfer paths between the chambers as well as the path necessary for taking a sample out of the apparatus or putting a new one into the load lock.

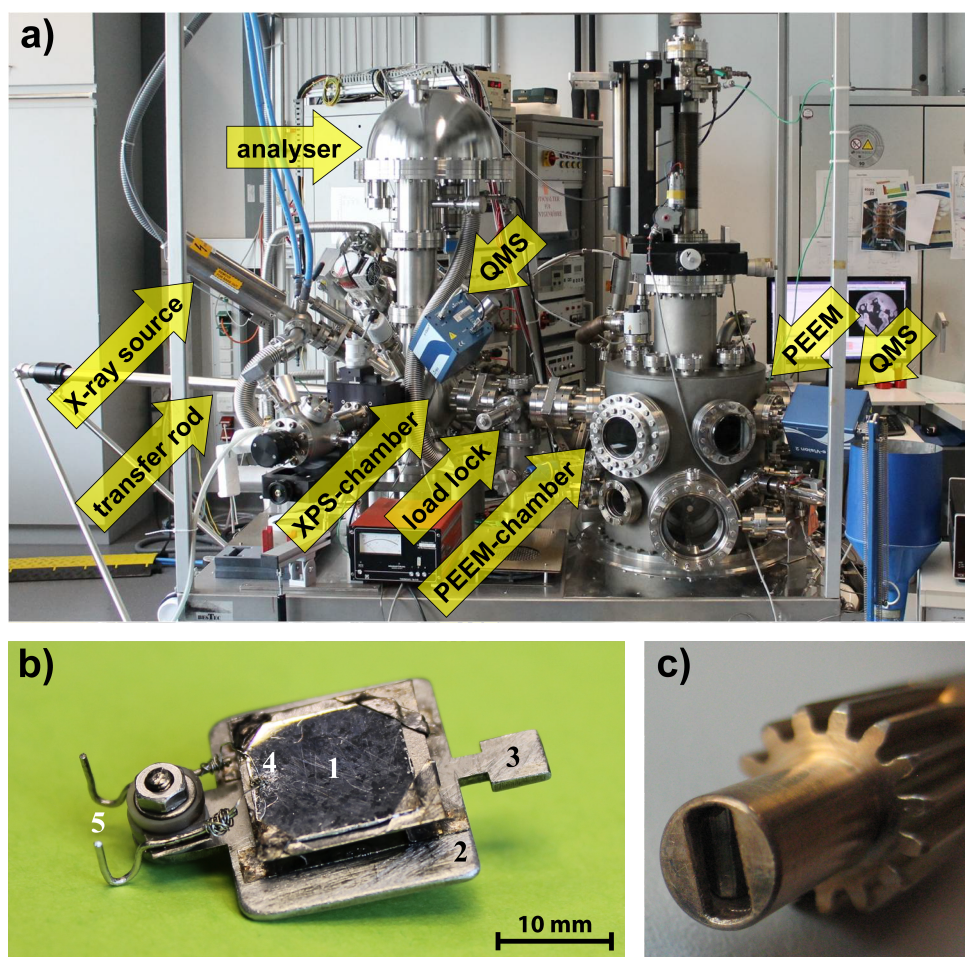


Fig. 3.2. Experimental set-up: a) UHV-system; b) Polycrystalline Rh foil (1) mounted onto the sample plate (2) with the transfer clutch (3). The NiCr/Ni type K thermocouple (4), which can be connected to the sample holder via the two contact electrodes (5), is spot-welded onto the sample; c) Transfer tool located at the end of the transfer rod.

3 Experimental

Chosen components of the UHV-apparatus, which were already mentioned above, are marked in the image of the set-up shown in Fig. 3.2a while the polycrystalline Rh foil mounted on the sample holder plate is imaged in Fig. 3.2b. To transfer the sample, first the transfer tool of the transfer rod, shown in Fig. 3.2c, is introduced into the transfer clutch of sample holder plate and locked by rotating the tool by 90° . Afterwards the sample can be transferred from one manipulator to another one, which is placed in a different chamber. Finally, the transfer tool can be unlocked and withdrawn. Using this procedure, the sample can be moved inside the UHV-system, i.e. without exposing it to air. Since the load lock can be sealed using gate valves (VAT) and each chamber can be pumped separately, samples can be taken out of the UHV-apparatus or placed inside the system via the load lock without breaking the vacuum in the two main chambers.

3.1.1 The PEEM-chamber

The photoemission electron microscope (PEEM-150, STAIB Instruments) is the eponymous device in the PEEM-chamber. The excitation of the photoelectrons, which are used to image the sample surface, is achieved by illuminating the sample with a water-cooled deuterium discharge UV lamp (D200, Heraeus), which has a cut off energy of 6.8 eV . Since it is necessary to place the sample during PEEM-measurements exactly perpendicular to the microscope axis as well as a few millimetres in front of the PEEM, the chamber is equipped with a manipulator having five degrees of freedom (freely movable in x -, y- and z-direction, one rotation axis perpendicular to the z-axis and the possibility to tilt the sample with respect to the z-axis).

Figure 3.3 shows the interior of the PEEM chamber. The base pressure of this chamber below 10^{-10} mbar is provided by an ion getter pump (StarCell 300, Varian). When performing experiments, this pump is usually sealed and the PEEM-chamber is solely pumped by a turbo molecular pump (TMU 260, Balzers) while the PEEM itself can be pumped differentially by another turbo molecular pump (TMU 071P, Pfeiffer Vacuum). A rotary pump (TriVac D8B, Leybold) provides the pre-vacuum (10^{-2} to 10^{-3} mbar) for both pumps. The differential pumping enables measurements in the PEEM-chamber in the 10^{-4} mbar range, while the pressure in the electron optics of the PEEM does not exceed the limit of $5 \times 10^{-7}\text{ mbar}$. Additionally, a titanium sublimation pump (TSP, Varian) is connected to the PEEM-chamber to increase the pumping speed for water.

The pressure in the PEEM-chamber can be monitored using five different devices. The total pressure can be measured by the combined Pirani and cold cathode pressure gauge

3 Experimental

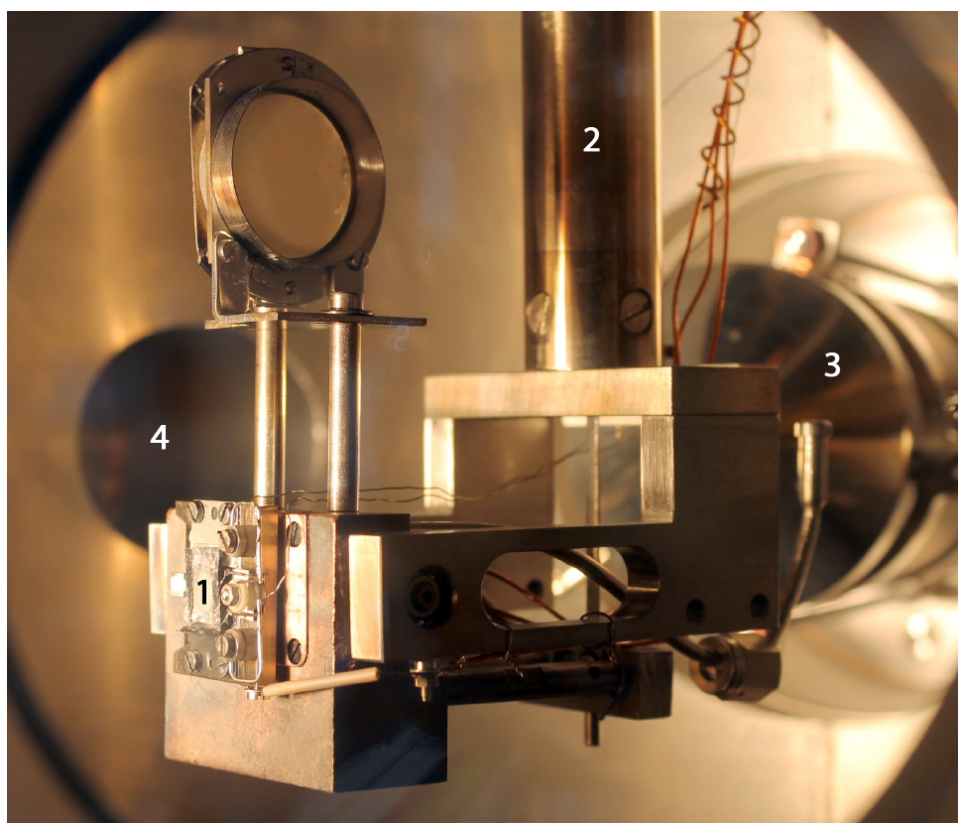


Fig. 3.3. View into the PEEM-chamber through a CF40 window showing the sample (1) placed at the sample holder adapter of the manipulator (2), the entrance cone of the PEEM (3) and the flange to the load lock (4).

(PKR 251, Compact FullRangeTM Gauge, Pfeiffer Vacuum) and a spinning rotor gauge (Viscovac, Leybold) while the composition of the gas phase within the PEEM-chamber can be monitored using a quadrupole mass spectrometer (e-Vision 2, MKS Spectra Products). As explained above, the electron optics of the PEEM and the reaction chamber are pumped differentially when experiments are performed. In this case, a Bayard-Alpert hot cathode ionization gauge is used to measure the pressure within the PEEM. Finally, the ion getter pump also indirectly measures the pressure within the pump via the ion current while the pre-vacuum is measured by thermal conductivity Pirani gauges (ThermoVac, Leybold).

The composition of the gas phase can be set using the gas supply system which consists of four leak valves (Balzers/Varian/MDC) connected to four gas cans (1 L CANgas, Messer Schweiz AG). High purity hydrogen (99,999%), oxygen (99,999%) and carbon monoxide (99,997%) can be introduced into the PEEM-chamber while argon (99,999%) can be dosed through the mounted Ar^+ ion sputter gun (IQE 11/35, SPECS).

3.1.2 The XPS-chamber

As already mentioned above, the XPS-chamber is, among other devices, equipped with cleaning facilities, an X-ray source and a hemispherical electron energy analyser. The water-cooled X-ray source (XR 50, SPECS) is mounted under the "magic angle" of 54.7° to the axis of the lens system of the hemispherical electron energy analyser (Phoibos 100, SPECS). Since the analyser is not equipped with a channeltron but with a micro-channel plate and a 2D-CCD detector, it is possible to measure spatially resolved XPS. Additionally, the position of the source can be adjusted using a linear motion feedthrough. Like the manipulator in the PEEM-chamber, the manipulator in the XPS-chamber (Standard LN2, SPECS) also has five degrees of freedom. It is freely movable horizontally and vertically and can be rotated perpendicular to the axis of the lens system of the hemispherical electron energy analyser as well as perpendicular to the axis of the manipulator. Further, the hemispherical analyser is connected to the chamber by a flexible metal hose to ensure better pumping conditions. The transfer rod, which can be used for transferring the sample, is also attached to the XPS-chamber. A view into the XPS-chamber through a CF40 window is shown in Fig. 3.4.

The base pressure below 10^{-10} mbar is provided by a combination of an ion getter pump and a titanium sublimation pump (VacIon Plus 500, Varian). The pressure is monitored using a combined Pirani and cold cathode pressure gauge (PKR 251, Compact FullRangeTM Gauge, Pfeiffer Vacuum) or an ionization gauge (MVC-3, Vacom). Alternatively, the ion getter pump also indirectly measures the pressure within the pump. Like the PEEM-chamber, also the XPS-chamber is equipped with a quadrupole mass spectrometer (e-Vision⁺, MKS Spectra Products) and a gas supply system consisting of two leak valves (MDC/Duniway Stockroom Corp.) and two gas cans (1 L CANgas, Messer Schweiz AG), namely high purity oxygen (99,999%) and argon (99,999%). This chamber is also equipped with similar cleaning facilities as the PEEM-chamber. The mounted Ar⁺ ion sputter gun (IQE 11/35, SPECS) is connected to the argon bottle, the sample can be annealed and the temperature of the sample can be measured by a type K thermocouple.

3.1.3 The load lock

Since the load lock is usually separated from the two main chambers by two closed gate valves, the load lock must be equipped with its own pumping system, i.e. with a turbo molecular pump (HiPace 80, Pfeiffer Vacuum) that provides the base pressure below 10^{-10} mbar. The necessary pre-vacuum of 10^{-2} to 10^{-3} mbar is achieved by a rotary

3 Experimental

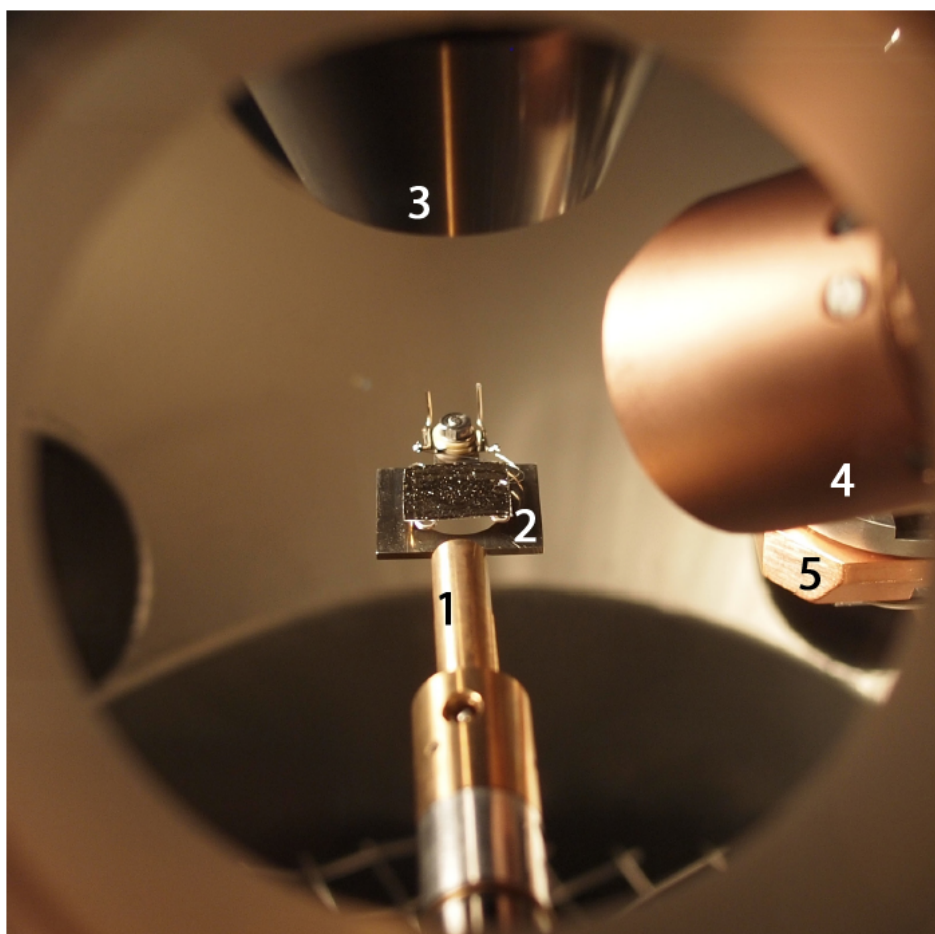


Fig. 3.4. View through a CF40 window into the XPS chamber showing the transfer rod (1) connected to a sample (2), a part of the hemispherical electron energy analyser (3), of the XPS source (4) and of the manipulator (5).

pump (Duo 5, Pfeiffer Vacuum) while the pressure within the load lock is measured by an ionization gauge (MVC-3, Vacom).

Since the XPS-chamber is connected to the load lock, as shown in Fig. 3.5, it also is possible to pump down the XPS-chamber via the load lock and the PEEM-chamber instead of using the ion getter pump. This possibility becomes relevant when XPS measurements at significantly higher pressures than the base pressure or cleaning procedures are performed. Similar to this approach, also the PEEM-chamber can be additionally pumped via the load lock if the gate valve between the PEEM-chamber and the load lock is open.

As already mentioned above, samples can be taken out or placed inside the load lock without breaking the vacuum in the main chambers. This can be done by venting the sealed load lock, removing the old sample from or mounting the new one on the feedthrough and

3 Experimental

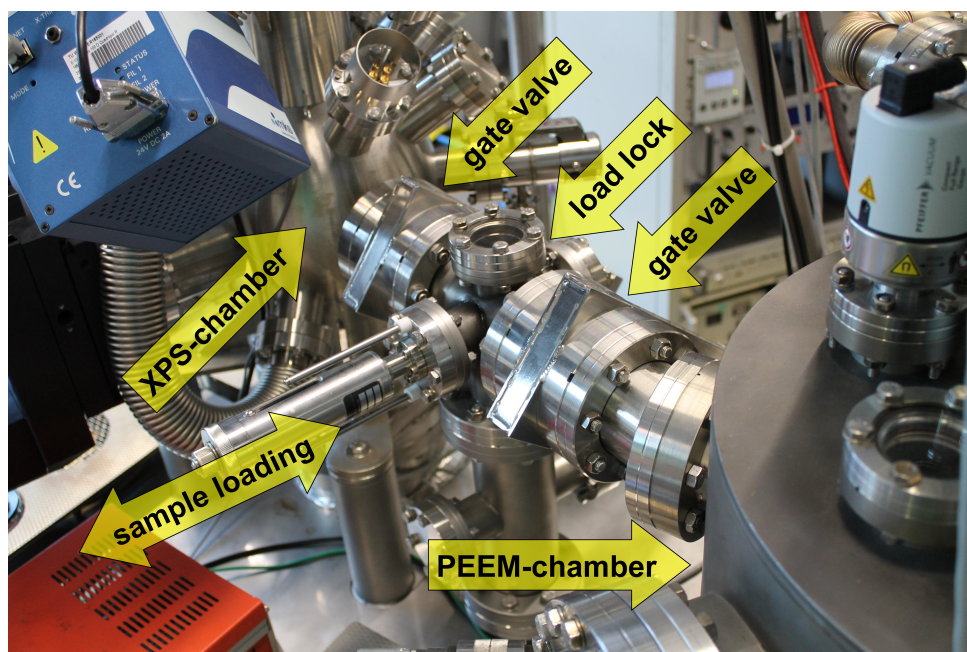


Fig. 3.5. Load lock located between the XPS-chamber and the PEEM-chamber.

evacuating the load lock again. After achieving a proper pressure, the gate valves between the main chambers and the load lock can be opened and the sample can be transferred.

3.2 Methods

Most results presented in this thesis were obtained using photoemission electron microscopy (PEEM) and quadrupole mass spectrometry (QMS). At the beginning of the presented studies, the purity of the studied samples and the effectiveness of the cleaning procedures were verified by X-ray photoelectron spectroscopy (XPS). Furthermore, the surfaces of the samples were also characterised by electron backscatter diffraction (EBSD) and atomic force microscopy (AFM) at the University Service Center for Transmission Electron Microscopy (USTEM).

In the following, the methods, which were primarily used for the present studies (PEEM, QMS, XPS) are explained in detail, while methods which were just used to characterise the surface of the model systems are just briefly outlined.

3.2.1 Photoemission Electron Microscopy

Photoemission electron microscopy (PEEM) was invented in the early 1930s when photoelectrons were used to image a metallic surface for the first time [84]. Since the PEEM-image brightness is related to the amount of the emitted photoelectrons, which in turn is related to the local work function, PEEM can be used to monitor any process that changes the work function of the surface. In contrast to scanning techniques like scanning tunneling microscopy or atomic force microscopy, which can only obtain information of small regions sequentially [85], PEEM can be used to image μm -sized regions of the surface in a parallel way, i.e. all monitored regions are visualised simultaneously. Approximately 60 years after the invention of PEEM, the development of UHV-compatible PEEM devices enabled applying this technique to observe *in situ* dynamic processes, such as adsorption, diffusion or layer growth [86]. The first attempts to apply PEEM to heterogeneous catalysis were performed on Pd and Pt single crystal surfaces [87–90]. The probably most famous application of PEEM, namely using it for monitoring oscillating surface reactions, was invented by the Nobel Laureate Gerhard Ertl [21].

3.2.1.1 The photoeffect

The photoeffect was discovered in 1887, when Hertz and Hallwachs observed the emission of photoelectrons from a metal sample, which was illuminated by electromagnetic radiation, i.e. UV-light [91, 92]. This phenomenon, which is illustrated in Fig. 3.6, was

3 Experimental

explained nearly thirty years later by Einstein [93], who was honoured for his work with the Nobel Prize in 1922. The most important equation of his thesis is

$$E_{kin} = h\nu - \Phi - E_B \quad (3.1)$$

where E_{kin} is the kinetic energy of an emitted photoelectron, $h\nu$ is the energy of the incident photon, Φ is the local work function of the sample and E_B is the binding energy of the electron. The work function, which also depends on the studied element, the local surface structure, adsorbates, etc., is defined as energy difference between the vacuum level E_{vac} and the Fermi level E_f of the sample.

$$\Phi = E_{vac} - E_f \quad (3.2)$$

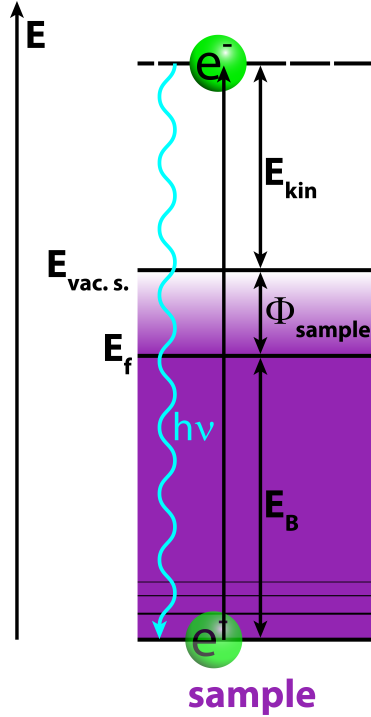


Fig. 3.6. Energy diagram of the photoeffect: An electron can be emitted if the energy of the incoming photon is bigger than the sum of the binding energy of the electron and the local work function of the material.

3.2.1.2 Working principle of the PEEM

A photoelectron spectrum has the width of $h\nu - \Phi$. Since UV-PEEM usually uses mercury lamps ($E_{max} = 4.9 \text{ eV}$) or deuterium lamps ($E_{max} = 6.8 \text{ eV}$) to illuminate the studied sample, the width of the obtained spectrum, which results from electrons emitted directly from the valence band, is in the dimension of a few eV . While only a small fraction of

3 Experimental

these electrons have not lost energy during their emission processes, the major part of the emitted yield are secondary (inelastically scattered) electrons with a very low kinetic energy. After emitting from the sample, the photoelectrons are accelerated, deflected and focused onto the detector by an electrostatic lens system. This detector usually consists of a microchannel plate (MCP) that amplifies the signal without losing its spatial resolution and a phosphorous screen which converts the electron beam into a visible image. The magnified image of the sample surface can be monitored by a video-camera. If a sufficient image brightness can be obtained (i.e. if a sufficient amount of electrons reaches the phosphorous screen), temporal resolution for real time imaging is only limited by the frame rate of the camera.

Inelastically scattered electrons are useless for spectroscopic applications like XPS but important for imaging techniques like PEEM since the image brightness depends solely on the sheer number of photoelectrons. According to the Fowler-theory [94], the photoelectron flux j emitted from a certain area of a surface can be approximately described by

$$j \sim (h\nu - \Phi)^2 \quad (3.3)$$

where $h\nu$ is the energy of the incident light and Φ represents the local work function of the sample area. Thus small changes of the local work function lead to a significant alteration of the photoelectron yield, which results in a change of the local PEEM-image brightness.

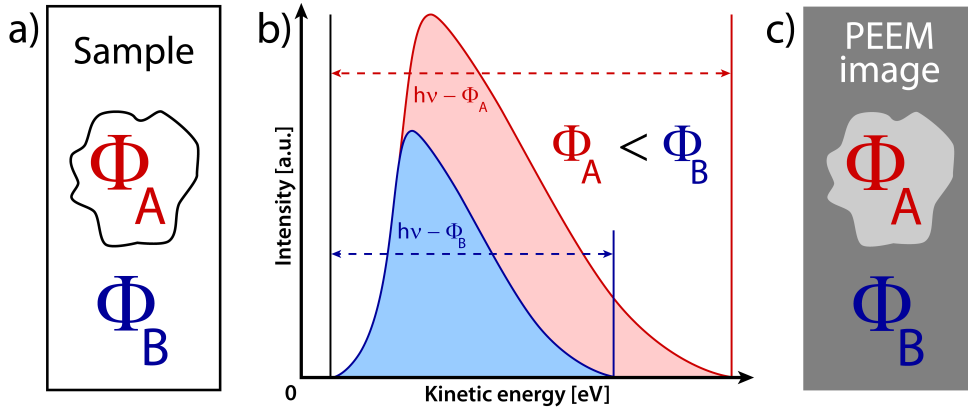


Fig. 3.7. Scheme of the contrast formation in PEEM after Ref. [95]: a) Metallic sample containing two regions of different work functions (Φ_A and Φ_B); b) Photoelectron emission spectra of the two regions; c) Resulting PEEM image reflects the differences in the local work function.

A schematic drawing of a sample surface consisting of two regions which exhibit different work functions is shown in Fig. 3.7a. If this sample surface is illuminated by UV light, photoelectrons are emitted from the whole sample surface. The area of the spectrum

which corresponds to the region which has a lower work function (Φ_A) is bigger than that corresponding to the higher work function (Φ_B) since the number of electrons emitted from the surface with lower work function is bigger than that emitted from the surface with higher work function. This difference, shown in Fig. 3.7b, results in a contrast within the PEEM-image, as illustrated in Fig. 3.7c.

3.2.1.3 Layout of a UV-PEEM

As mentioned above, a UV-PEEM consists of a UV-source, an electrostatic lens system and a detector. A schematic drawing of the PEEM-150 (STAIB Instruments), which was used in the present study, is shown in Fig. 3.8.

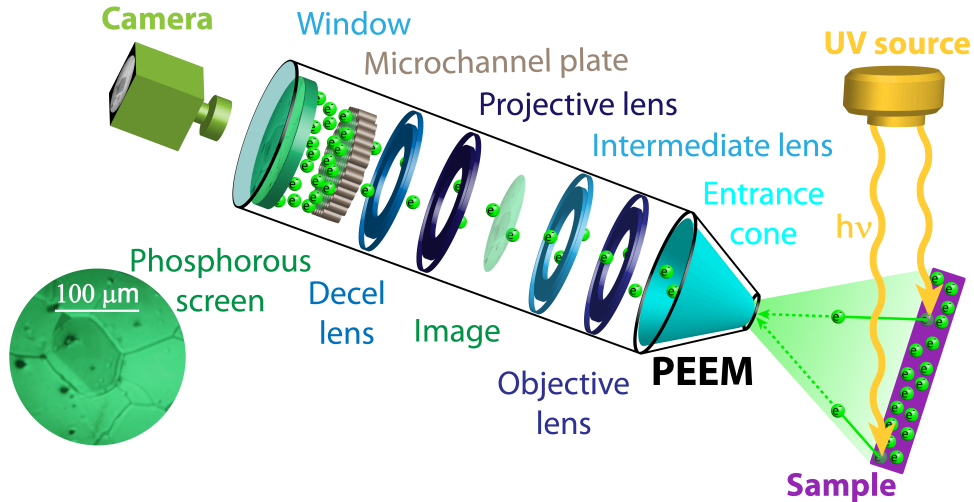


Fig. 3.8. Schematic drawing of a UV-PEEM: Due to the illumination of the sample by UV-light photoelectrons are emitted. These photoelectrons are focused by an electrostatic lens system, amplified by a microchannel plate and projected onto a phosphorous screen. Finally, a magnified picture of the sample forms on the phosphorous screen which can be recorded by a CCD camera. The PEEM-image placed in the bottom left corner shows the surface of a polycrystalline Pd foil.

A deuterium lamp with a cut-off energy of 6.8 eV was used to illuminate the sample, which is placed approximately 5 to 10 mm in front of the entrance cone, under an incident angle of circa 75° . The emitted photoelectrons are accelerated into the cone by an anode voltage of 15 kV . The following objective lens, which is set to a voltage of approximately 3.3 kV , forms a real image of the sample surface. This image is further magnified by the intermediate lens, where a voltage of 10 kV is applied. The signal is amplified by a microchannel plate (MCP) to enable imaging the sample surface with sufficient intensity.

3 Experimental

Since the MCP, which is a kind of array of channeltrons, has its sensitivity maximum for impinging electrons between 200 and 2000 eV, the kinetic energy of the photoelectrons is decreased by the projective lens (1.58 kV) and the decelerating lens (1.25 kV) before the electrons reach the MCP (800 V). Finally, the amplified electron beam is accelerated by a voltage of 3 kV onto the phosphorous screen which converts the magnified electron image into visible light. This screen is monitored through a window by a high speed CCD-camera (Hamamatsu Digital Camera C9300), which is placed outside the UHV-system. This set-up allows to monitor sample surfaces with a spatial resolution in the low μm and a temporal resolution in the low μs range. The diameter of the field of view is approximately 450 μm .

3.2.1.4 The kinetics by imaging approach

It was already discussed above, that the local work function influences the number of emitted photoelectrons, which, in turn, is linked to the local PEEM-image brightness. Since adsorbats influence the local work function and since the catalytic activity of the studied surface is related to the coverages of the adsorbed species, the local image brightness can be linked to the catalytic reactivity. Thus information about the catalytic activity of a certain region, e.g. of a domain of a polycrystalline foil, can be obtained by analysing the local image intensity. This method is known as the *kinetics by imaging* approach [96]. Figure 3.9 illustrates the basic idea of this approach in the case of the catalytic H_2 oxidation on Rh.

Since the adsorbed oxygen increases the local work function, less photoelectrons are emitted from the oxygen covered surface than from the adsorbate free or from the hydrogen covered surface. Thus the oxygen covered Rh surfaces appears in PEEM darker than a clean or hydrogen covered surface.

As already discussed in 2.3, changing the external parameters, for example p_{H_2} , can lead to the kinetic transition τ_A from the oxygen covered (poisoned) state to the reduced (catalytically active) state. If p_{H_2} is decreased again, the reversed transition τ_B from the steady state of high reactivity to the steady state of low reactivity occurs at a different (lower) p_{H_2} . The resulting hysteresis plot of the H_2O production rate is schematically shown in Fig. 3.9c. These kinetic transitions are also reflected in the image brightness, as shown schematically in Figure 3.9d. Therefore, the kinetic transition points τ_A and τ_B can be experimentally obtained either by analysing the H_2O production rate or the image intensity.

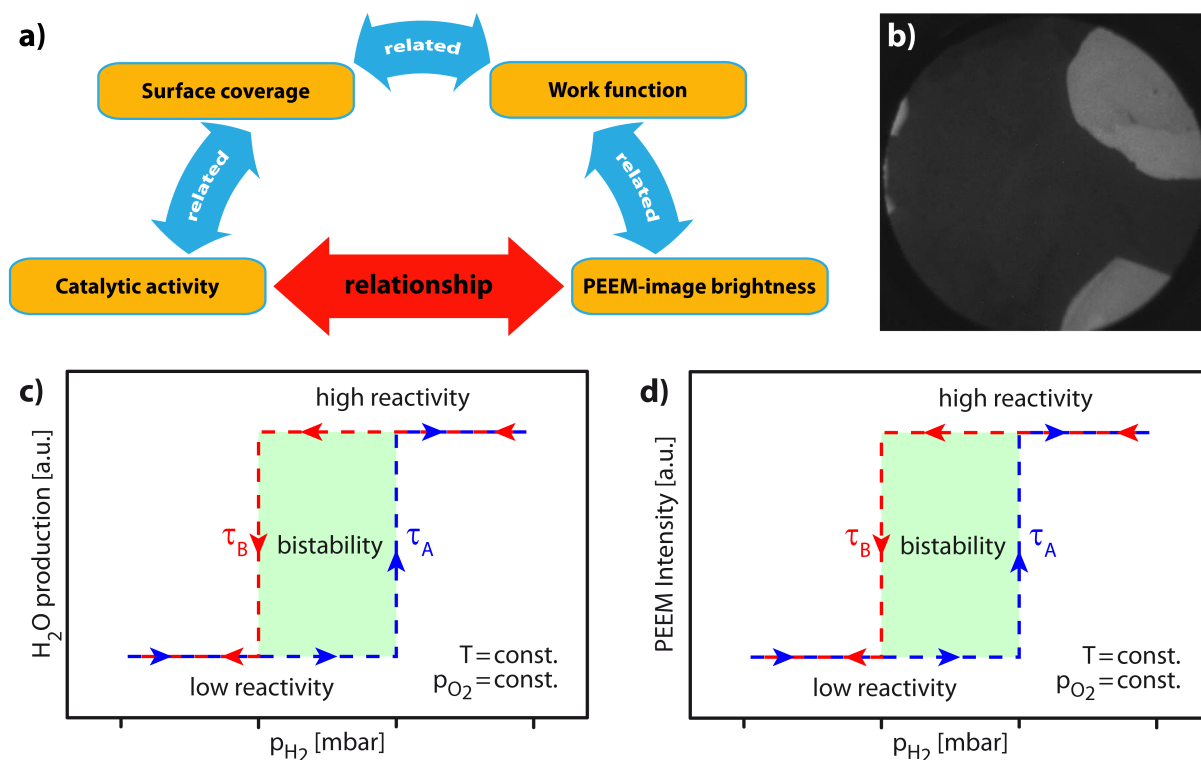


Fig. 3.9. Kinetics by imaging: a) Schematic relation between the catalytic activity and the PEEM-image brightness; b) PEEM-image of the ongoing H₂ oxidation on a polycrystalline Rh foil taken at 513 K, $p_{O_2} = 7.7 \times 10^{-7}$ mbar and $p_{H_2} = 8.1 \times 10^{-7}$ mbar. The dark region corresponds to the oxygen covered (catalytically inactive) surface while the bright regions indicate almost clean (active) regions; c) Schema of a hysteresis plot of the H₂O production rate in the isothermal catalytic H₂ oxidation on Rh at constant p_{O_2} , as already shown in 2.3; d) Schema of the corresponding hysteresis plot of the PEEM Intensity. The kinetic transition points τ_A and τ_B can be obtained from either of both plots.

3.2.2 Quadrupole Mass Spectrometry

Mass spectroscopy (MS) is commonly used for residual gas analysis because the partial pressures and the total pressure can be measured simultaneously. In the present work, MS was additionally used to monitor the H₂O production rate.

The working principle of a quadrupole mass spectrometer (QMS) is based on the mass-to-charge analysis of gas ions using a magnetic field. When gas molecules enter the ion source of a QMS they get ionised, e.g. by electron ionisation (EI), fast-atom-bombardment (FAB), electrospray ionisation (ESI) or Matrix-assisted laser desorption/ionisation (MALDI). The formed ions are accelerated towards the detector, but only those who exhibit a certain mass to charge ratio ($\frac{m}{z}$) can pass the analyser placed between the ion

3 Experimental

source and the detector. By scanning different $\frac{m}{z}$ -ratios partial pressures can be measured, which can be added up to obtain the total pressure. Furthermore, an MS can be used as leak check device. In this case the gas tightness of certain components of a UHV chamber is checked by analysing changes in p_{He} within the system while a flux of helium is directed toward the outside of the component.

The QMS (e-Vision 2, MKS Spectra Products) mounted to the PEEM-chamber, which is schematically illustrated in Fig. 3.10, was mainly used to monitor the total pressure as well as the partial pressures p_{O_2} and p_{H_2} . Entering gas molecules are ionized by an electron beam, which originates from a filament. If the pressure is high enough, i.e. if the flux of ions passing the quadrupole mass analyser is sufficient, a Faraday cup can be used as detector. Otherwise the additional use of an electron multiplier (EM) enables measuring pressures down to 3.8×10^{-14} mbar.

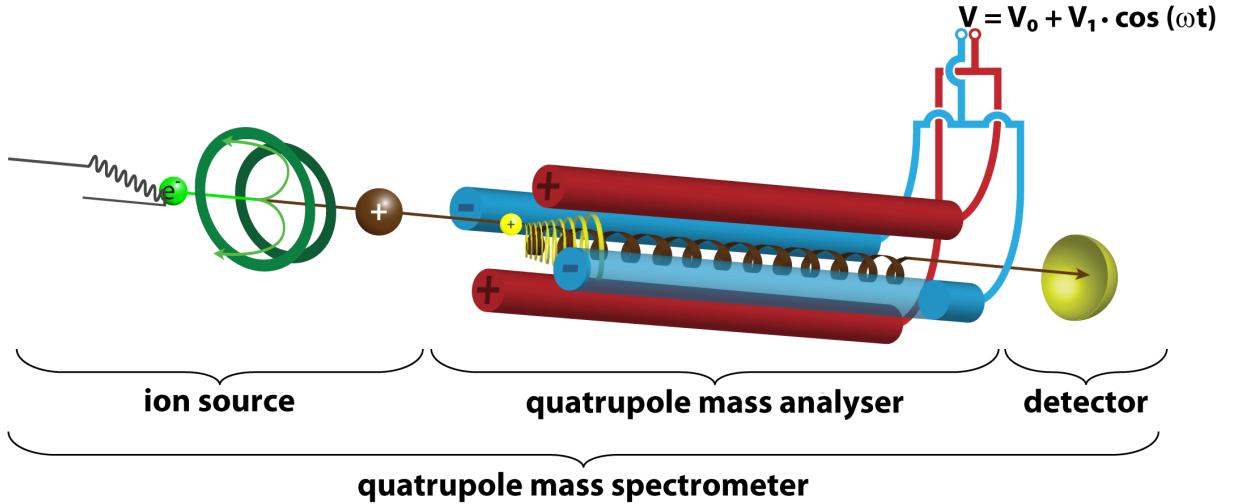


Fig. 3.10. Working principle of a QMS: Only ions having the same mass-to-charge ration as the brown ion can reach the detector on a stable spiral-like trajectory. The yellow ion is filtered out since it exhibits a different mass-to-charge ratio.

The quadrupole mass analyser consists of four parallel cylindrical electrodes, arranged in a uniform cross. A DC voltage (V_0) and an AC voltage (V_1) with the angular frequency ω are applied to the electrodes, so that opposite electrodes are poled identically. Thus the voltages

$$V^+ = V_0 + V_1 \cdot \cos(\omega t), \quad (3.4)$$

3 Experimental

and

$$V^- = -V_0 - V_1 \cdot \cos(\omega t) \quad (3.5)$$

are applied to the two pairs. The resulting quadrupole field is a superposition of electrostatic and electrodynamic fields. This field forces the ions, which exhibit the right $\frac{m}{z}$ -ratio, onto a stable spiral-like trajectory while the flight path of ions exhibiting different ratios is unstable. Thus only ions having a certain $\frac{m}{z}$ -ratio, which depends on the set parameters V_0 , V_1 and ω , can reach the detector. Commercial QMS usually vary either ω or V_0 and V_1 to measure different partial pressures. Since QMS only uses the $\frac{m}{z}$ -ratio as selection criteria, two ions having the same $\frac{m}{z}$ -ratio but different masses and charges, e.g. $m_2 = 2 \cdot m_1$ and $z_2 = 2 \cdot z_1$, can not be distinguished. Other difficulties for the interpretation of QMS-spectra result from the fact, that big molecules can degrade or that particles can be ionized several times, e.g. O_2^{++} .

3.2.3 X-ray Photoelectron Spectroscopy

X-ray photoelectron spectroscopy (XPS), which was originally called electron spectroscopy for chemical analysis (ESCA), is a chemically sensitive surface science technique based on the analysis of photoelectrons, which are excited by X-rays and emitted from the core-levels of surface atoms of a sample. Although the first broad band of photoelectrons emitted from a metal sample via the photo-effect due to the illumination by X-rays was recorded already in 1907 by P. D. Innes [97], it took 47 years until the first high-energy-resolution XPS-spectrum was obtained [98]. In 1981 Kai Siegbahn was honoured for this achievement with the Nobel Prize in physics "for his contribution to the development of high-resolution electron spectroscopy".

It was already mentioned in 3.2.1, that illuminating a surface with photons may lead to the emission of electrons. Since the photoelectron spectrum has the width of $h\nu - \Phi$, the spectrum obtained using an X-ray source is significantly broader than that obtained using a UV-source, i.e. due to the increase of the energy of the impinging radiation also core electrons can be excited. Usually X-rays are generated by a Mg- K_α -source (1253.6 eV) or an Al- K_α -source (1486.6 eV) while E_{kin} of the photoelectrons is measured by an energy analyser.

As already discussed in 3.2.1.1, the kinetic energy $E_{Kin, sample}$ of an emitted photoelectron is given by Einstein's formula

$$E_{Kin, sample} = h\nu - \Phi_{sample} - E_B \quad (3.6)$$

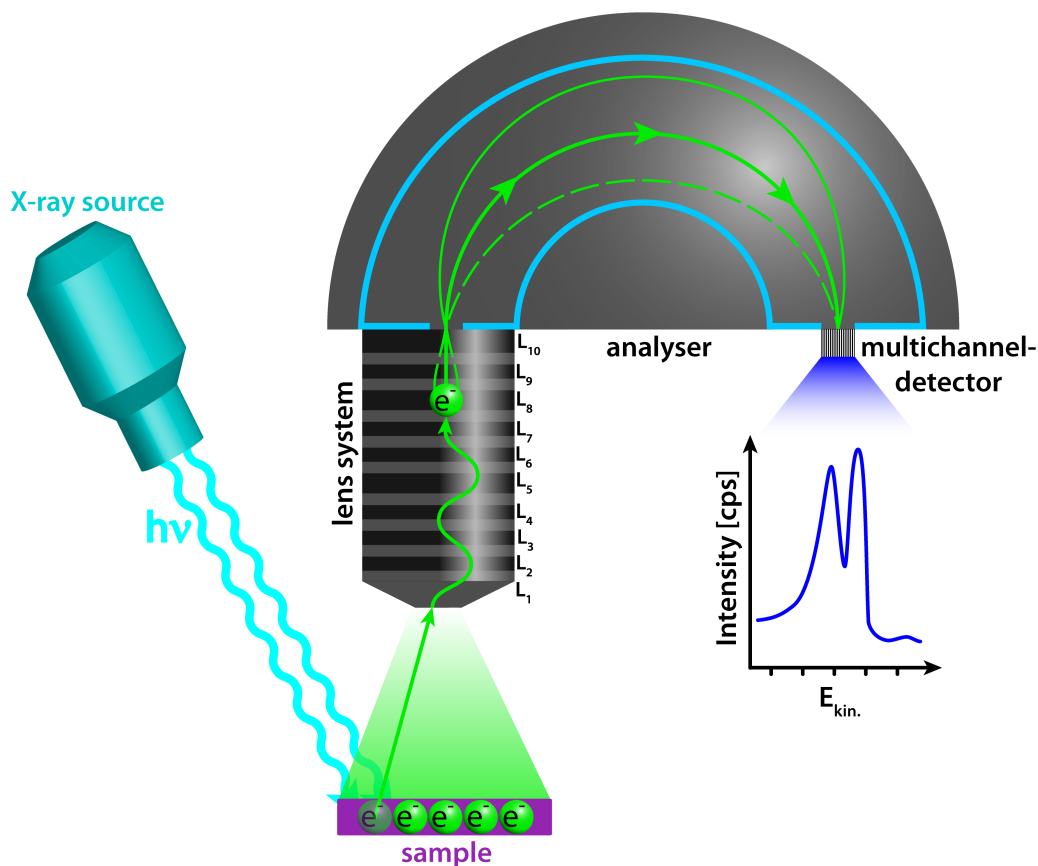


Fig. 3.11. Working principle of an XPS: The kinetic energy of photoelectrons, which are emitted from the sample due to the illumination by X-rays and focused by a lens system, is measured by a hemispherical energy analyser. The obtained data contains chemical information about the sample.

where $h\nu$ is the energy of the electromagnetic radiation, Φ is the local work function of the sample and E_B is the binding energy of the electron. In the case of XPS, $h\nu$ is known while E_{Kin} is usually measured by an hemispherical analyser (HSA). Since the sample and the analyser are connected via an electric conductor, the Fermi levels of these two metals are equalised. Thus it is not necessary to determine the unknown work function of the sample.

Due to the contact potential between the sample and the analyser, the kinetic energy of the photoelectrons changes during their flight from the sample to the analyser by $\Phi_{ana.} - \Phi_{sample}$. Thus E_B can be obtained by measuring $E_{Kin, ana.}$ if $\Phi_{ana.}$ and $h\nu$ are known.

$$E_{Kin, ana.} = h\nu - \Phi_{sample} - E_B - (\Phi_{ana.} - \Phi_{sample}) \quad (3.7)$$

$$E_{Kin, ana.} = h\nu - E_B - \Phi_{ana.} \quad (3.8)$$

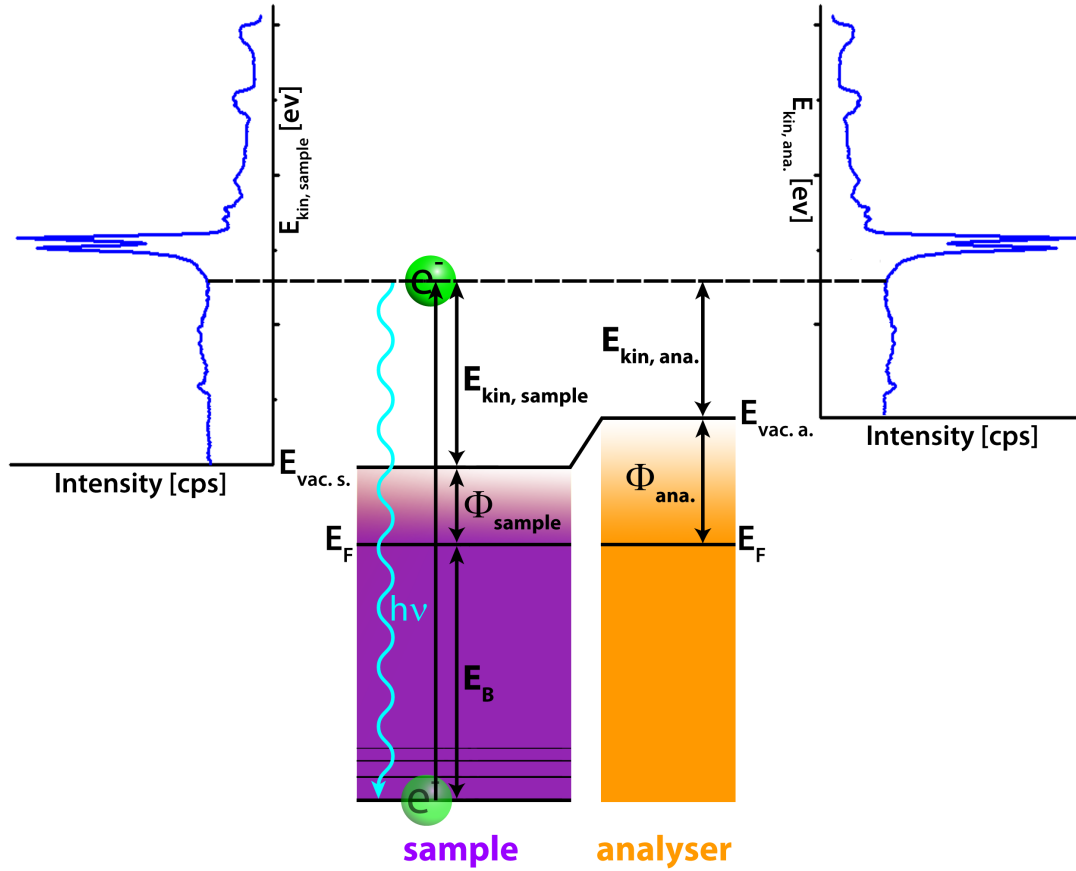


Fig. 3.12. Working principle of an XPS-analyser: The Fermi level of the sample and the analyser are equalised because this two components are electrically connected.

$$E_B = h\nu - E_{\text{kin, ana.}} - \Phi_{\text{ana.}} \quad (3.9)$$

Before the kinetic energy of the photoelectrons is measured by the HSA, the electrons first need to enter the analyser through a complex lens system which fulfils three different functions. First, the system can be used to adjust the dimensions of the studied region of the sample surface. Secondly, the system focuses the electron beam on the entrance slit S_{en} of the HSA and thirdly the system usually accelerates or slows down the electrons. As shown in Fig. 3.13, the analyser consists of a spherical capacitor with radii r_1 and r_2 to which the voltages V_1 and V_2 are applied. Thus photoelectrons enter a constant electrostatic field when they pass the entrance slit. Electrons having an kinetic energy close to the pass energy follow a semicircular trajectory with the radius r_0 before they leave the analyser through the exit slit S_{ex} and get detected by the multichannel-detector. Electrons exhibiting a kinetic energy that differs too much from the pass energy collide with the inner or the outer hemispheres.

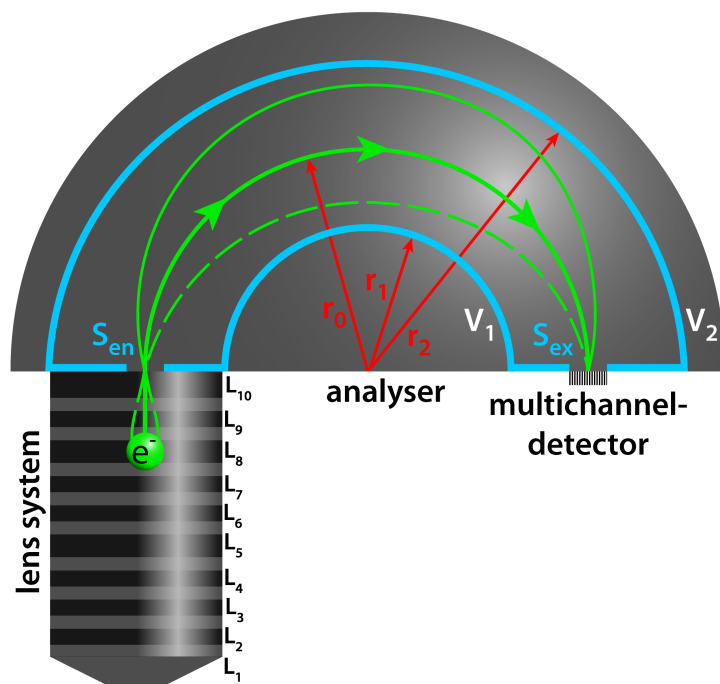


Fig. 3.13. Schematic cross section of a hemispherical electron energy analyser including the lens system, the entrance slit S_{en} , the spherical capacitor with radii r_1 and r_2 , to which the voltages V_1 and V_2 are applied, the approximately semicircular trajectories of electrons having kinetic energies which are close to the pass energy, the exit slit S_{ex} and the multichannel-detector.

During the emission process, an excited electron can either lose energy due to inelastic scattering or it can keep its energy if it only scatters elastically or does not even scatter at all. Photoelectrons, which lose kinetic energy due to inelastic collisions, can not be assigned to a certain atomic orbital any more, i.e. they cannot be used to obtain chemical information about the sample. On average, an electron scatters inelastically after travelling the inelastic mean free path λ in a material. Thus the information depth of XPS strongly depends on λ since the probability P of an electron to emit from a certain depth d without losing energy can be approximately described by

$$P(d) \sim e^{-\frac{d}{\lambda}}. \quad (3.10)$$

According to this dependence, approximately 63% of the emitted photoelectrons, which can be used to obtain chemical information about the sample, originate from a depth $d < \lambda$, circa 86% from a depth $d < 2 \cdot \lambda$ and nearly 95% from a depth $d < 3 \cdot \lambda$.

The *universal curve*, shown in 3.14, illustrates that λ lies for most metals between 5 and 20 Å and that the minima of both, the theoretical and the experimental data, is located

3 Experimental

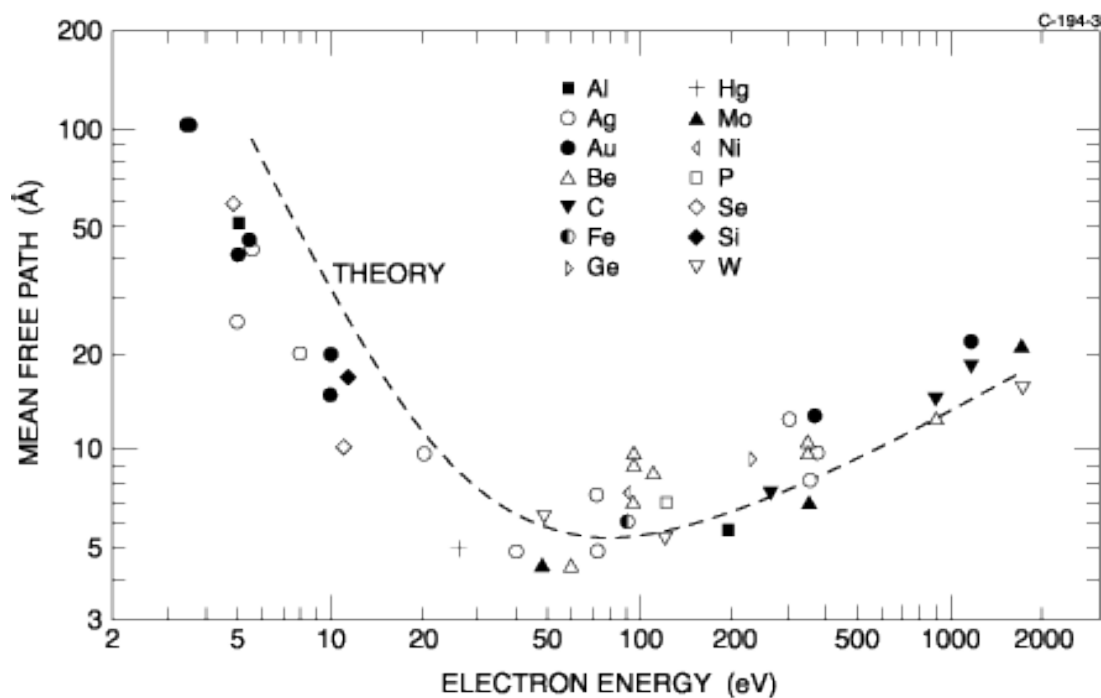


Fig. 3.14. Universal mean free path curve from Ref. [99] showing its minimum for most metals between 15 and 150 eV.

at kinetic energies between 15 and 150 eV. Thus, the data shown in Fig. 3.14 enable to estimate the surface sensitivity of XPS for a certain material.

The plot of the kinetic energy distribution for the analysed photoelectrons (counts per second against the kinetic energy) is called XPS-spectrum. The occurring peaks result from emitted electrons, which originate from certain orbitals of an element and which have not lost energy during their emission processes, while electrons which lost energy, contribute to the background. A schematic photoelectron spectrum for an incident photon energy of a few keV (X-rays) is shown in Fig. 3.15.

Due to the spin-orbit coupling, atomic orbitals with an angular momentum quantum number $l \neq 0$, i.e. p, d and f, may have two different energy states with different probabilities of occupancy. These probabilities can be described by the multiplicity M , which can be calculated using the formula

$$M = 2 \cdot j + 1. \quad (3.11)$$

where j is the sum of l and the spin momentum quantum number s which is $\pm\frac{1}{2}$. Thus peaks, which correspond to p-state ($l = 1$, $s = \pm\frac{1}{2}$) split up into two peaks. Since the total angular momentum j can either be $\frac{1}{2}$ or $\frac{3}{2}$, the multiplicities result in 2 and 4. Therefore, the ratio of the peak areas of $p_{1/2}$ to $p_{3/2}$ is 4 : 2 respectively 2 : 1. Analogously, the

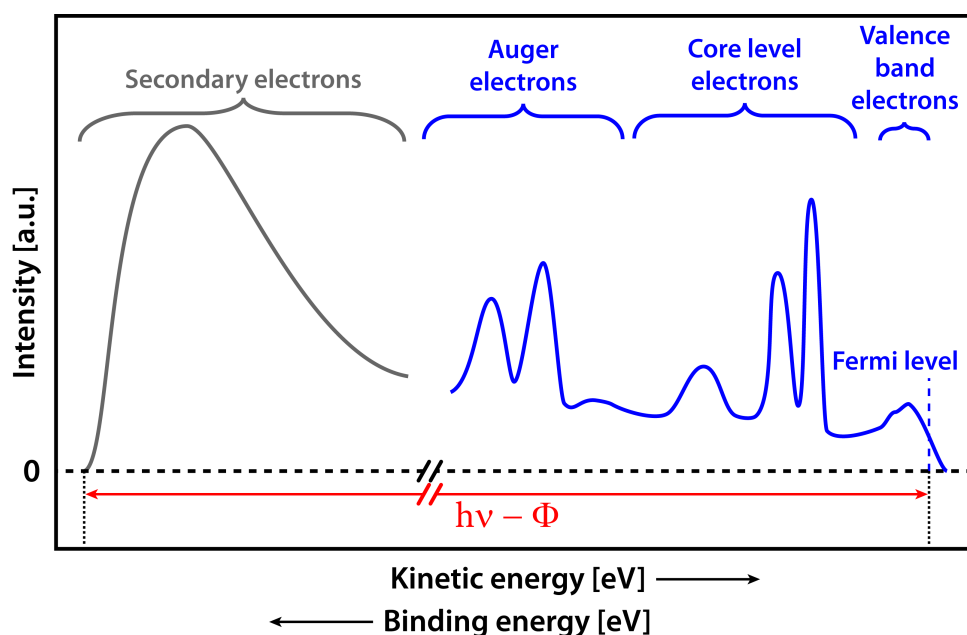


Fig. 3.15. Schematic photoelectron spectrum for an excitation energy of a few keV : The width of the spectrum depends on the energy of the incident radiation $h\nu$ and the sample work function Φ .

peak areas of $d_{3/2}$ and $d_{5/2}$ split up at a ratio of 2 : 3 while the areas of $f_{5/2}$ and $f_{7/2}$ divide up at a ratio of 3 : 4.

Besides these main peaks from the atomic orbitals, additional peaks can be observed within an XPS-spectrum. If a core level electron is emitted, it leaves behind a hole, which can be filled by an electron from a higher energetic level. Due to a photon, which is emitted during this process, another electron can be excited and in the following be emitted as a so called Auger electron. Auger electrons can be easily identified by changing the excitation source, since their kinetic energies are independent of the energy of the incident radiation [100]. In turn, the X-ray satellite peaks depend on the source. If the excitation source is non-monochromatic, the electromagnetic radiation consists of a characteristic line and several minor compounds, which exhibit higher photon energies than the characteristic line. Therefore each peak, which corresponds to a certain orbital of an element, is accompanied by a satellite peak which is shifted towards lower binding energies. The shift of these peaks can be predicted since it is identical for all peaks in the spectrum. On the other hand, shake-up lines occur at higher binding energies than the main peaks. In this case, a photoelectron excites another electron of its atom during its emission process and thus loses a certain amount of energy, i.e. the energy difference between the excited and the ground state of the second electron.

3 Experimental

Generally, the position of the peaks reveals qualitative information about the composition of the sample. However, modifications of the atomic environment, e.g. through an oxidation process, can lead to a "chemical shift" of the corresponding peak.

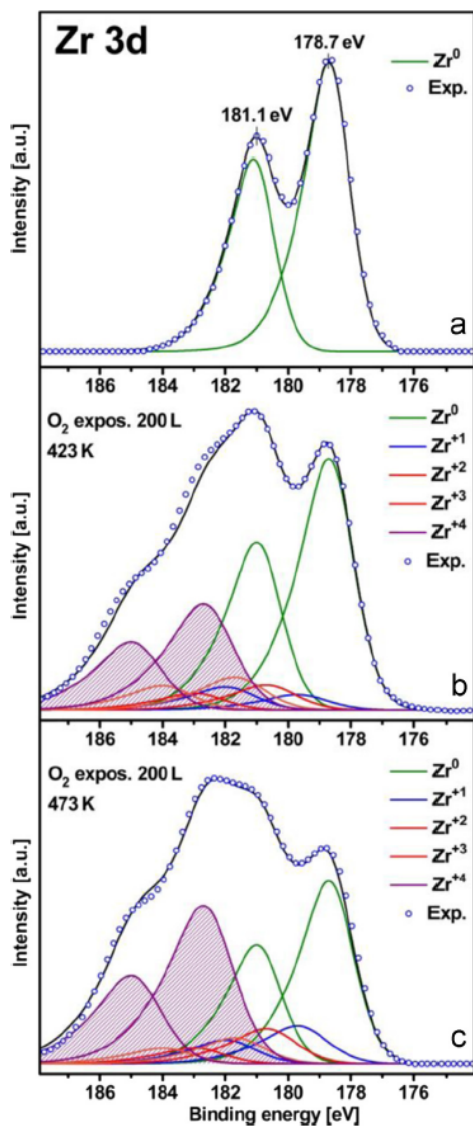


Fig. 3.16. Example of chemical shifts for different oxidation states of Zr from Ref. [101]: a) Metallic spectra fitted solely using the two metallic peaks of Zr 3d; b - c) Spectra of oxidised Zr. Besides the metallic peaks, also peaks corresponding to different oxidation states are necessary to fit the spectra.

Such shifts are illustrated in Fig. 3.16, which shows our measurements for different oxidation states of Zr [101]. Figure 3.16a shows the XPS-spectrum of clean Zr while (b) and (c) illustrate spectra of oxidised Zr. It is clearly seen, that the peaks, which correspond to the different Zr_xO_y states, are, in comparison to the metallic peak, shifted towards higher binding energies.

For obtaining quantitative information about particular species, the area of the corresponding peaks has to be analysed. For this, the sensitivity factor SF , which represents

3 Experimental

the probability of a certain atomic orbital to emit a photoelectron, has to be considered. The sensitivity factor SF is defined as

$$SF = f \cdot \sigma \cdot \varphi \cdot \lambda \cdot A \cdot T \quad (3.12)$$

with f standing for the photon flux, σ for the atomic cross section of the adsorption of a photon by the corresponding orbital, φ for the tilting angle between the analyser axis and the sample, λ for the mean free path of the photoelectrons in the sample, A for the illuminated area of the sample and T meaning the detector sensitivity. The number of atoms of a certain species within the studied region n can be calculated using the formula

$$n = \frac{I}{SF} \quad (3.13)$$

with I meaning the measured intensity.

3.2.4 Electron backscatter diffraction

Electron backscatter diffraction (EBSD) is commonly used to study crystalline surfaces qualitatively [102]. For example EBSD can be used to identify the crystallographic orientations of the μm -sized domains a polycrystalline metal foil consists of.

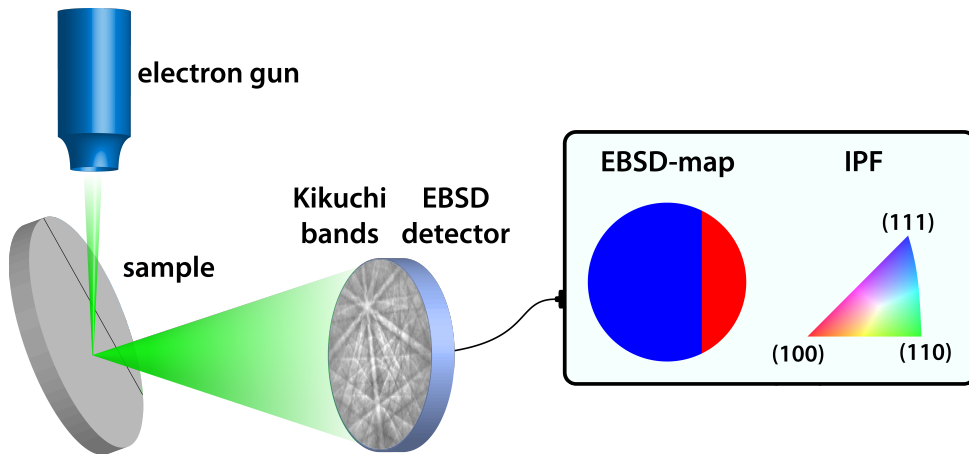


Fig. 3.17. Working principle of an EBSD: The sample surface is raster scanned by the electron beam of a SEM. Analysing the formed Kikuchi patterns reveals information about the crystallographic orientation of the sample surface, which can be summarised in a EBSD-map. The picture showing the Kikuchi bands was adapted from Ref. [103].

In the present study, the polycrystalline Rh foil was analysed at the University Service Center for Transmission Electron Microscopy of the Technische Universität Wien

3 Experimental

(USTEM) using a scanning electron microscope (SEM), which is equipped with an EBSD detector, as schematically shown in Fig. 3.17. During the experiments an electron beam (*current* $\sim 1 - 50$ nA, *acceleration voltage* $\sim 10 - 30$ keV) raster scans across the sample which is mounted in the SEM stage at the angle of 70° in respect to the normal position. The incident electrons diffract several times among the crystallographic planes of the studied material before they leave the sample again. The formed diffraction pattern is composed of intersecting bands (Kikuchi bands), which directly reflect the crystal lattice structure of the corresponding sample spot [104, 105]. Thus the spatial resolution of the SEM limits the spatial resolution of the EBSD.

The Kikuchi pattern are recorded by an EBSD detector, which is monitored by a CCD-camera while a computer software determines the crystallographic orientation of the surface for each spot by analysing the observed diffraction patterns. This data is usually summarised in a colour-coded EBSD-map, whereby the inverse pole figure (IPF) serves as legend.

3.2.5 Atomic force microscopy

Atomic force microscopy (AFM), which was developed on the basis of the scanning tunneling microscope (STM) in 1986 [106], is commonly used to image sample surfaces on the nm-scale or even with atomic resolution. The working principle of AFM is based on the interatomic forces between single atoms of a tip and the studied sample. Thus, in contrast to STM, also isolating sample surfaces can be imaged. Further, the maximum dynamic range, especially in the z-direction, is much higher in case of AFM and the use of AFM does not require UHV-conditions. AFM measurements can even be carried out under ambient pressure conditions, although the resolution is in this case worse than under low-pressure conditions.

In the present study, the surface of the Rh single crystal was analysed at the USTEM using an AFM, which is schematically shown in Fig. 3.18. A very sharp tip with a nominal tip radius in the low nm range, which is mounted on the cantilever spring, was used to scan the sample. A deflection of the tip caused by irregularities of the surface can be observed using a laser, which is focused onto the backside of the cantilever and reflected towards a four-segment photodiode since the deflection of the cantilever leads to a deflection of the laser spot. A feedback-mechanism readjusts the sample stage until the laser beam again hits the center of the photodiode. Analysing this readjustment results in an image of the topography of the sample surface.

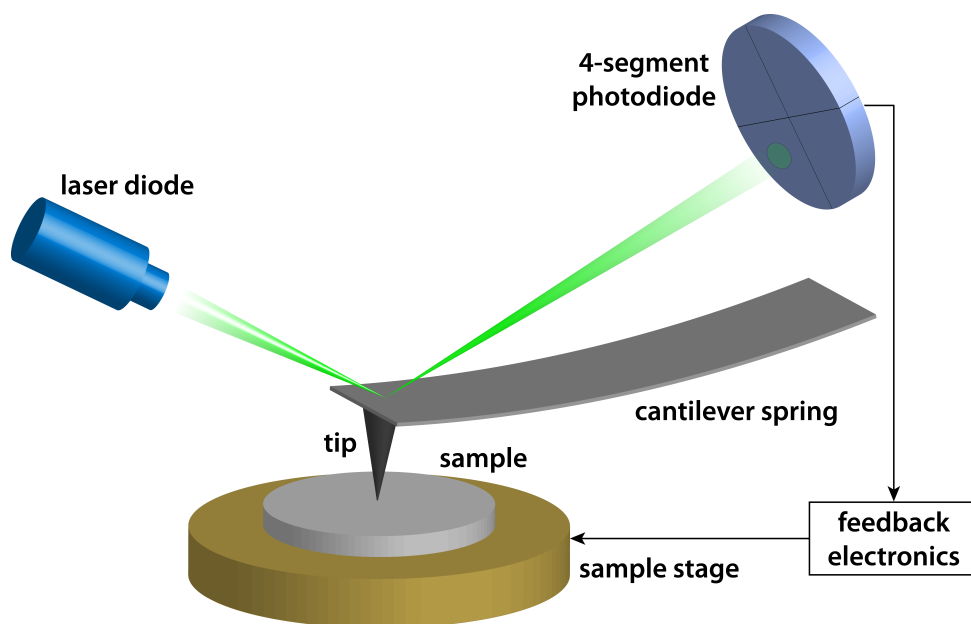


Fig. 3.18. Working principle of an AFM: The tip mounted on the (vibrating) cantilever scans across the sample surface. Changes of the deflection or of the resonance frequency of the cantilever due to mechanical forces between the tip and the sample are detected by a laser system. Analysing this data reveals the information necessary for imaging the topography of the sample surface.

In general, AFM can operate in different modes. In the "contact mode" the tip contacts the sample. The measured forces can be addressed to the overlapping wave functions of the tip and the sample and the resulting repulsion due to the Pauli principle. In this mode, the repulsion is kept constant via the feedback mechanism. In turn, the attractive force between the tip and the sample is measured in the non-contact mode and the tapping mode. In both modes, the cantilever oscillates with a frequency near its resonance frequency, but with a different amplitude. Attractive forces like the van der Waals force occurring between the surface or the tip decrease the frequency. In these modes, the feedback mechanism stabilises the oscillation amplitude or the frequency by adjusting the distance between the tip and the surface.

3.3 The catalytic systems

In the present study, two different Rh model catalysts were studied. Before the polycrystalline *Rh* foil and the *Rh*(111) single crystal are introduced in 3.3.2, the surface structure of Rh is briefly discussed in 3.3.1.

3.3.1 Rhodium

Rh crystallizes in a face-centred cubic (fcc) crystal lattice with a lattice constant of approximately 3.8 \AA [107, 108]. Usually for fcc systems the formation of the low-Miller-index planes of fcc metals, such as $Rh(100)$, $Rh(110)$ and $Rh(111)$, are preferred. However, Rh surfaces, which are used in commercial catalysts, consist mainly of stepped and kinked high-Miller-index domains. Such stepped surfaces are arrays of low-index oriented terraces, e.g. (100), which are generally separated by monoatomic steps.

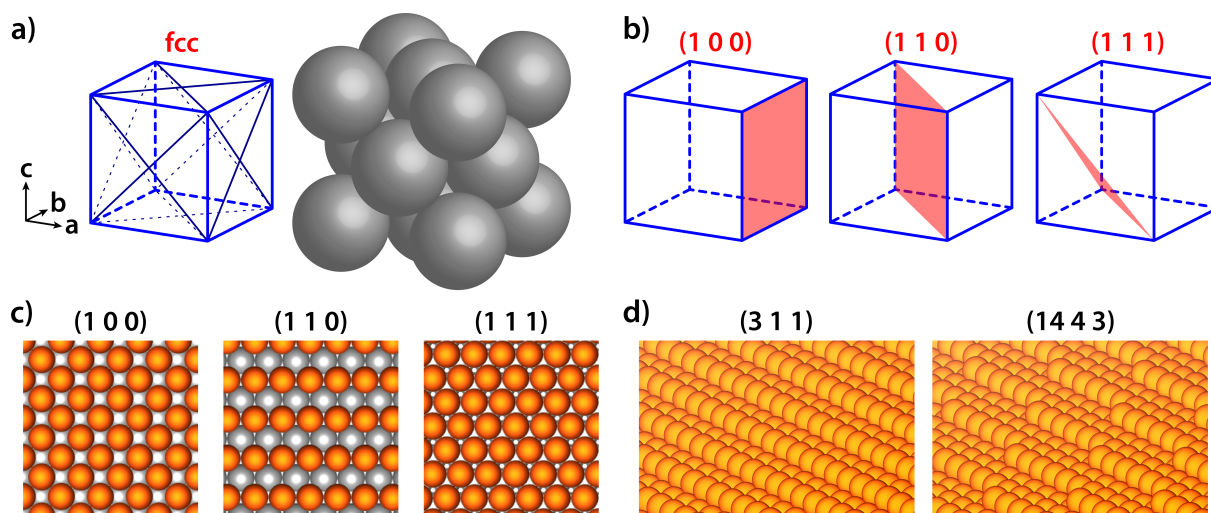


Fig. 3.19. Surface structure of Rh surfaces: a) Unit cell of Rh; b) Schematic illustration of low-Miller-index planes; c) Ball models of low-Miller-index Rh surfaces; d) Ball model of stepped Rh surfaces.

Figure 3.19a shows the unit cell of Rh. While Fig. 3.19b schematically depicts the low-Miller-index planes of Rh, ball models of these surfaces are illustrated in Fig. 3.19c. It can be seen, that the $Rh(110)$ surface is the most open structure while the $Rh(111)$ is the closed packed surface. Figure 3.19d shows ball models of two vicinal $Rh(100)$ surfaces, namely the $Rh(311)$ and the $Rh(1443)$ surface. While the step edges of the $Rh(311)$ surface are straight, the edges of the $Rh(1443)$ surface exhibit kink atoms.

3.3.2 The rhodium model catalysts

A $10 \times 10 \text{ mm}^2$ polycrystalline Rh foil of 0.2 mm thickness (MaTecK, purity 99.97%) and a $10 \times 10 \text{ mm}^2$ $Rh(111)$ single crystal of 0.6 mm thickness (MaTecK, purity 99.99%) served in the present study as model catalysts. The samples were mounted onto sample

3 Experimental

holder plates, as already shown in Fig. 3.2b. Both samples were cleaned using standard UHV-cleaning procedures (Ar^+ sputtering, annealing and heating in oxygen).

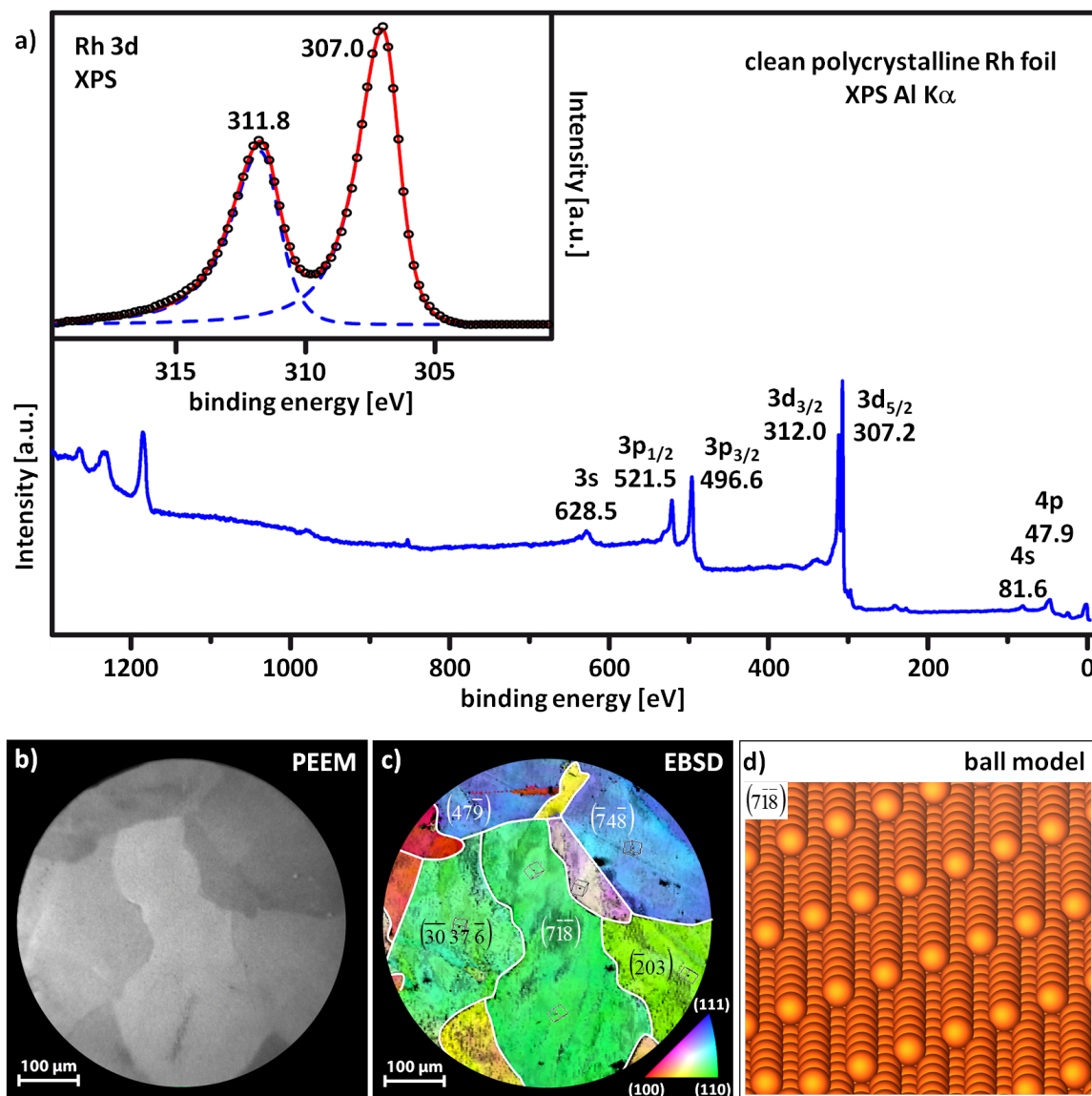


Fig. 3.20. The polycrystalline Rh foil: a) XPS survey spectra of the clean Rh foil and a detailed scan of the Rh 3d region; b) PEEM image of the clean Rh foil; c) EBSD-map of the same region. Chosen crystallographic orientations are indicated while domain borders are marked as white lines; d) Ball model of the stepped surface of the $Rh(7\bar{1}8)$ domain.

An XPS survey spectrum of the clean Rh foil and a detailed scan of the Rh 3d region are shown in Fig. 3.20. Right after these spectra were taken, the Rh foil was transferred within the UHV-system from the XPS-chamber to the PEEM-chamber to image the sample surface. A PEEM-image of the clean Rh surface is shown in Fig. 3.20b. The contrast within

3 Experimental

this image can be explained considering the Smoluchowski theorem [109], which correlates a higher atomic density with a higher work function. For example a closed-packed $Rh(111)$ surface exhibits a higher work function than the most open $Rh(110)$ surface. Besides the atomic density of the surface, its topography also influences the PEEM-image brightness. The roughness of a surface and structural features, like mesoscopic defects, grain boundaries, scratches, adatoms, etc., influence the photoemission yield and therefore the local image brightness. The exact orientations of the domains located within the field of view shown in Fig. 3.20b were obtained by EBSD-measurements. The corresponding results are summarised in the EBSD-map shown in Fig. 3.20c, where the IPF-map placed in the right bottom corner serves as legend. The indicated high-Miller-index domains consist of stepped surfaces, as shown for the $Rh(7\bar{1}\bar{8})$ domain in Fig. 3.20d.

The $Rh(111)$ single crystal surface exhibits a roughness depth which is smaller than $0.01 \mu m$ and an orientation accuracy smaller than 0.1° . Similar to the Rh foil, the flat $Rh(111)$ single crystal was also mounted onto a sample holder plate and the effectiveness of the cleaning procedure was verified by XPS before the catalytic hydrogen oxidation was studied.

4

Experimental results

In section 4.1 observations concerning reaction fronts in the catalytic hydrogen oxidation on high-Miller-index domains of a polycrystalline Rh foil are presented. Further, the influence of the roughness of the Rh surface on its catalytic reactivity is discussed and the kinetic phase diagrams for a smooth (annealed) and for a defect-rich (additionally sputtered) Rh surface are compared.

Under certain reaction parameters, self-sustaining oscillations of the reaction rate may occur in the hydrogen oxidation on Rh, although all the parameters, such as temperature and the partial pressures of hydrogen and oxygen are kept constant. The reason for this oscillating behaviour is the periodic change of the adsorbed reactants on the sample surface, which occurs due to changes in the adsorption properties of the Rh surface. This phenomenon can be monitored by PEEM. The observed pattern formation and features, which influence the multifrequencial coupled oscillations, such as the width of the terraces of a stepped surface or the amount of kinks, are addressed in section 4.2.

Modern commercial catalysts usually do not consist of μm -sized surfaces but of metal nanoparticles supported by oxides. Such individual nanoparticles can be modelled by a sharp nanosized tip. Thus it is reasonable to compare the reaction behaviour of the μm -sized domains of the Rh foil and of a nm-sized Rh tip. Such a comparison focusing on the kinetic phase diagrams and the oscillating behaviour is presented in section 4.3.

The self-sustained reaction rate oscillations in the catalytic hydrogen oxidation on Rh observed on both μm - and nanoscale might be based on the same feedback mechanism. Such a feedback mechanism based on the formation of subsurface oxygen is proposed and the observed indications for this feedback mechanism are presented in section 4.4.

4.1 Bistability and steady states of the hydrogen oxidation on the polycrystalline rhodium foil

Modern catalysts usually consist of noble metal (Pt, Pd, Rh) nanoparticles supported by various oxides [110]. Rhodium nanoparticles are e.g. used in the three-way-catalyst or energy conversion technology [111]. Since the existing studies concerning the hydrogen oxidation on rhodium were mostly done on low-index single crystal surfaces [49, 112, 113], we still need to attain detailed knowledge about the role of more complex surface structures. Therefore it is important to study the catalytic behaviour of differently stepped Rh surfaces. Stepped surfaces are usually studied using single crystal surfaces with high-Miller-indexes or using curved crystals, for which the step density varies across the sample surface [114–116]. Applying the first approach for studying the role of different step densities on the catalytic reactivity necessitates repeating the same experimental procedure for differently orientated single crystals. Doing so has two obvious disadvantages: it is difficult to keep the parameters in different experiments exactly the same and secondly such a set of single crystals is pretty expensive. Applying the second approach, i.e. using curved crystals, involves the challenge of resolving local reaction kinetics. Methods, which can only obtain area-averaged kinetic data (e.g. mass-spectrometry) can hardly manage to differentiate between the catalytic reactivity of differently orientated planes or facets of the same crystal.

For the study presented in this thesis, a third approach which allows the study of different regions of the sample surface simultaneously was applied: the *kinetics by imaging approach*. As already explained in detail in 3.2.1.4, it is based on the relationship between the surface coverage (and thus the catalytic activity) and the local work function of a surface, which in turn is reflected in the local PEEM image brightness [96]. Therefore, analysing PEEM-video sequences of ongoing reactions reveals information about the local catalytic behaviour. Since the studied polycrystalline Rh foil, as already described in 3.3.2, consists of μm -sized grains, whose crystallographic orientation varies within the studied field of view, the processes on different high-Miller-index surfaces can be directly compared in a single experiment and therefore under identical experimental conditions.

4.1.1 Nucleation and propagation of hydrogen reaction fronts

As already discussed in 2.3, studies of the catalytic H_2 oxidation on single crystals revealed the bistable character of the reaction, i.e. in a certain parameter range two steady states

4 Experimental results

(of low and high activity) may exist under exactly the same conditions [49]. The kinetic transitions from one steady state to the other are manifested by propagating reaction fronts [49, 112–114, 117]. Also, unusual features like triangular-shaped reaction fronts on a $Rh(111)$ single crystal surface, which seem to be linked to the formation of subsurface oxygen species, were reported [118].

Polycrystalline foils are particularly suitable for studying the nucleation and propagation of reaction fronts, since they provide a playground for comparing phenomena on differently structured surfaces within one experiment [120–123, 129]. Such a polycrystalline Rh foil is used in the present experiments. Since studies of the CO oxidation on such a Rh foil as well as on a polycrystalline Pd foil revealed that the CO reaction fronts nucleate mainly at the domain borders [124, 125], the first question to prove was whether the hydrogen fronts exhibit a similar behaviour.

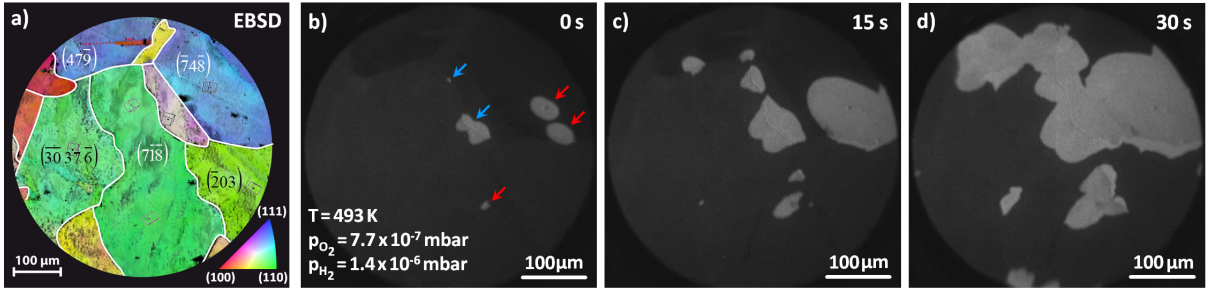


Fig. 4.1. Nucleation of hydrogen fronts in the H_2 oxidation on Rh: a) EBSD map of the studied field of view. Crystallographic orientations of individual domains are indicated; b) PEEM-video-frame illustrating the nucleation of hydrogen fronts at 493 K, $p_{O_2} = 7.7 \times 10^{-7}$ mbar and $p_{H_2} = 1.4 \times 10^{-6}$ mbar. The fronts nucleate both at domain borders (blue arrows) and within domains (red arrows); c) H_2 fronts nucleated in (b) propagate and new H_2 fronts nucleate; d) Continuation of (c).

Figure 4.1 illustrates the nucleation and propagation of hydrogen reaction fronts on the polycrystalline Rh foil during the kinetic transition from the inactive oxygen covered state (dark areas) to the active reduced state (bright areas). A comparison of the EBSD map, shown in Fig. 4.1a, with the positions of the nucleation events in the PEEM-video frame, shown in 4.1b, reveal that some H_2 fronts nucleate, similar to the CO fronts, on grain boundaries (blue arrows). In contrary to the CO oxidation, additional nucleation events on defects within domains were observed (red arrows). Fig. 4.1c and d show the spreading of existing fronts across the surface, while new reaction fronts still nucleate.

The subsequent question which can only be studied on polycrystalline samples concerns the role of the grain boundaries in the spreading of reaction fronts. It is known, that domain borders on polycrystalline platinum group metals confine the propagation of reaction

4 Experimental results

fronts in the catalytic CO oxidation reaction. This was already shown for polycrystalline Pt and Pd foils [120–123] as well as for the present Rh foil [124]. The role of the domain borders in the H₂ front propagation is illustrated in Fig. 4.2, where a front which approaches the domain border between the $Rh(\bar{7}4\bar{8})$ and $Rh(\bar{2}0\bar{3})$ domain was monitored.

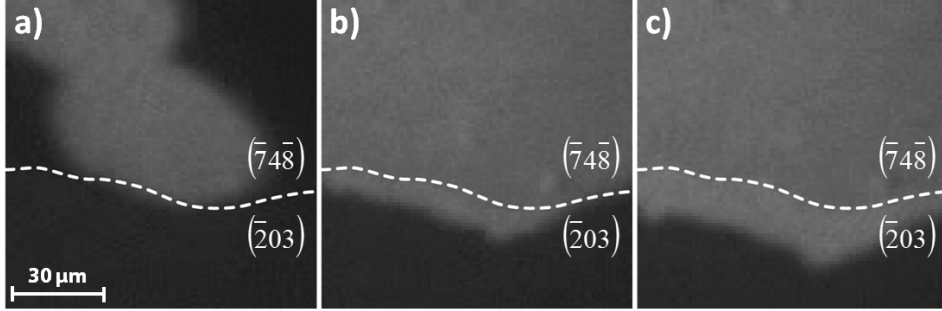


Fig. 4.2. Propagation of a H₂ reaction front across a grain boundary: a) PEEM-video frame showing a hydrogen front nucleated within the $Rh(\bar{7}4\bar{8})$ domain (bright area) at the moment of reaching the grain boundary between the $Rh(\bar{7}4\bar{8})$ and $Rh(\bar{2}0\bar{3})$ domain (dashed white line); b) The same H₂ front, but 0.75 s later. The front has crossed the grain boundary and continues spreading into the $Rh(\bar{2}0\bar{3})$ domain; c) The same, but 3 s later. The H₂ front continues propagating within the $Rh(\bar{2}0\bar{3})$ domain. All three frames were taken at 493 K, $p_{O_2} = 7.7 \times 10^{-7}$ mbar and $p_{H_2} = 1.9 \times 10^{-6}$ mbar.

During the kinetic transition from the inactive (oxygen covered surface) state (dark area) to the active (reduced surface) state (bright area) the H₂ front propagates unhindered across the grain boundary between the $Rh(\bar{7}4\bar{8})$ and the $Rh(\bar{2}0\bar{3})$ which is marked in Fig. 4.2a - c as dashed white line. On the first sight, this result is quite surprising since the activation energies for the CO and the H₂ oxidation on Rh are comparable [32, 126]. To our knowledge there are only two reported cases, where CO fronts can cross confines between differently orientated surfaces in the studied parameter range. First, CO reaction fronts on nanotips can spread from one facet to another one since the diffusion length of CO (μm -range) is significantly larger than the facet size (nm-range) [123]. Secondly, CO fronts are able to cross the grain boundaries of an Ar⁺ sputtered palladium foil, because the sputtered palladium can partially fill the boundary cracks [125]. Since our sample is neither a nanotip nor a heavily sputtered surface, it is necessary to find another explanation for this observation. One possible reason might be the different diffusion properties of CO and hydrogen on Rh. In the studied temperature range and at comparable submonolayer coverages on $Rh(111)$ the diffusivity of hydrogen is at least two orders of magnitude higher than that of CO [127]. This difference seems to be the reason why hydrogen, at least under the applied conditions, can cross the sub-micrometer grain boundaries be-

4 Experimental results

tween the domains.

Also the propagation of the reaction fronts in the H_2 oxidation on smooth single crystal surfaces exhibits interesting properties. For example wave patterns on anisotropic surfaces like the $Rh(110)$ surface are elliptically distorted [128], while hydrogen reaction fronts on the isotropic $Rh(111)$ surface can be circular or triangular shaped [118]. In addition, studies on stepped single crystals show that the presence of steps also influences the shape of the reaction fronts since hydrogen can diffuse faster in the direction parallel to the step edges than perpendicular [129, 130]. The presently studied Rh foil is well suitable for studying the influence of steps on different high-index surfaces within one experiment since its surface is composed of various stepped domains (see Fig. 4.1a).

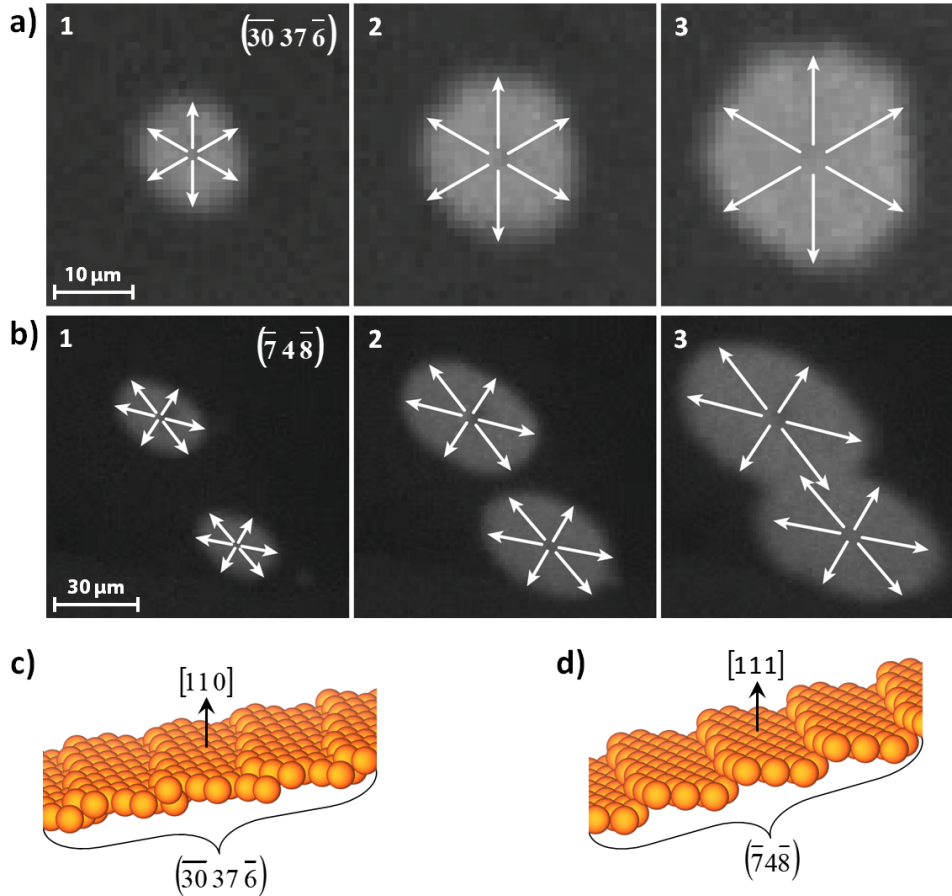


Fig. 4.3. Isotropic and anisotropic propagation of H_2 reaction fronts on stepped Rh surfaces: a) Circularly shaped front propagating on the $Rh(\bar{30}37\bar{6})$ domain at $473\ K$, $p_{O_2} = 7.7 \times 10^7\ mbar$ and $p_{H_2} = 2.3 \times 10^6\ mbar$. The time-interval between the frames 1, 2 and 3 is $0.75\ s$; b) Elliptically shaped H_2 fronts propagate on the $Rh(\bar{7}4\bar{8})$ domain. The temperature, the partial pressures and the time-interval between the frames 1, 2 and 3 are the same as in (a); c) Ball model of the $Rh(\bar{30}37\bar{6})$ surface; d) Ball model of the $Rh(\bar{7}4\bar{8})$ surface.

4 Experimental results

The present observations show that the H₂ reaction fronts on differently stepped high-index surfaces exhibit different shapes under identical conditions. For example the shape of the reaction front on the $Rh(\overline{30}37\overline{6})$ domain is approximately circular (Fig. 4.3a) while the observed fronts on the $Rh(\overline{7}4\overline{8})$ domain are elliptically shaped (Fig. 4.3b). Since the front propagation on the $Rh(\overline{30}37\overline{6})$ domain is mainly influenced by two factors, this behaviour can be explained. The surface consists of furrowed (110) terraces, as shown in Fig. 4.3c, for which one would rather expect an anisotropic front propagation. However, this anisotropy is compensated by the perpendicularly orientated steps. In turn, elliptically shaped H₂ fronts, observed on the $Rh(\overline{7}4\overline{8})$ domain, originate from the combination of the isotropic front propagation on the (111) terraces, as shown in Fig. 4.3d, and the additional distortion caused by the steps.

Conclusively, artificially modifying the roughness of surfaces can influence the behaviour of reaction fronts [125]. To prove this for the H₂ fronts on stepped Rh surfaces, the reaction front propagation for the annealed and for the additionally sputtered Rh surface was studied.

Figure 4.4a and b illustrate the reaction front propagation on the annealed $Rh(47\overline{9})$ and $Rh(7\overline{1}\overline{8})$ domains while Fig. 4.4c and d show the same for the additionally sputtered $Rh(47\overline{9})$ and $Rh(7\overline{1}\overline{8})$ domains. In both cases, the front propagates faster on the $Rh(47\overline{9})$ domain than on the $Rh(7\overline{1}\overline{8})$ domain. Since the partial hydrogen pressure varies in the two experiments (annealed and sputtered surface) and since the reaction front velocity depends on the partial hydrogen pressure, it is hardly possible to compare the absolute front propagation velocity, but one can compare the ratio of the front propagation velocities evaluated for the annealed and for the sputtered surface. On the annealed domains the H₂ front propagates approximately four times faster on the $Rh(47\overline{9})$ domain than on the $Rh(7\overline{1}\overline{8})$ domain. If the surface is sputtered with Ar⁺ long enough, the additionally created defects should dominate the surface structure and therefore equalise the reaction front velocity measured on different domains of the sample. Nevertheless, on the additionally sputtered domains the front propagations differ still by a factor of three, i.e. despite of the "equalising" sputtering effect, the surface structure seems to be still dominated by its original shape.

Summary

Summarising this chapter, it was shown, that the hydrogen reaction fronts nucleate on the polycrystalline Rh foil at domain borders as well as on defects within the domain. The reaction fronts propagate across the grain boundaries and spread unhindered over

4 Experimental results

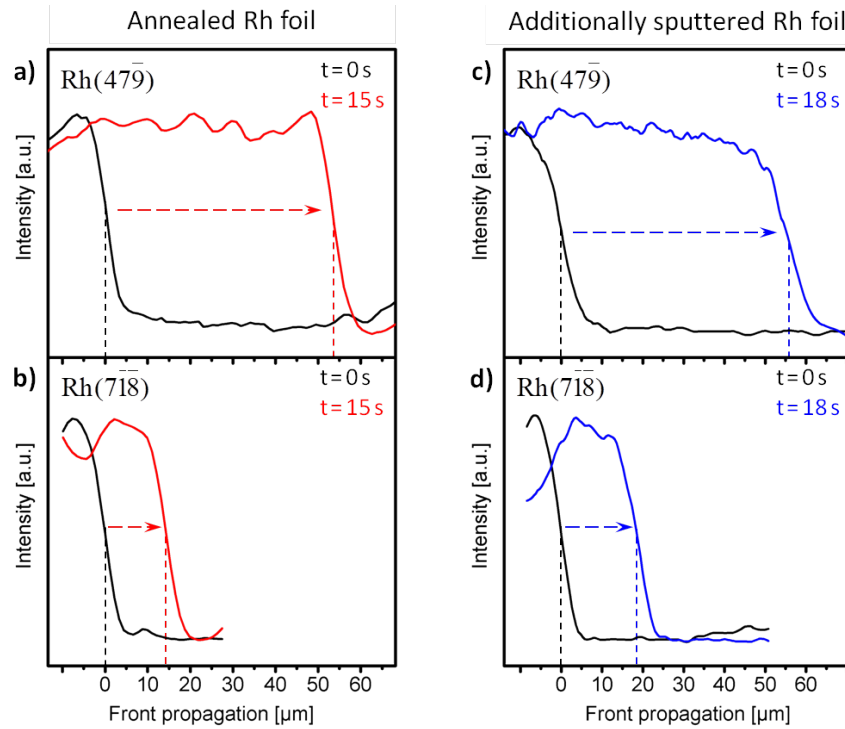


Fig. 4.4. Propagation of reaction fronts on annealed and on additionally sputtered domains of the Rh foil: a) Temporal evolution of the intensity profile illustrating the propagation of the H_2 front on the annealed $Rh(479)$ domain of the polycrystalline Rh foil at 493 K , $p_{O_2} = 7.7 \times 10^{-7}\text{ mbar}$ and $p_{H_2} = 1.9 \times 10^{-6}\text{ mbar}$; b) The same as (a), but for the $Rh(7\bar{1}8)$ domain; c) The same as (a), but after additionally sputtering for 15 min using Ar^+ ions of 1 keV energy ($\text{emission current} = 8\ \mu A$, $p_{Ar} = 1 \times 10^{-5}\text{ mbar}$). The front was observed at $p_{H_2} = 1.1 \times 10^{-6}\text{ mbar}$; d) The same as (c), but for the $Rh(7\bar{1}8)$ domain.

the whole polycrystalline sample surface. The shape of these fronts is determined by the diffusivity of the adsorbed hydrogen on the terraces and over the edges of the terraces since the oxygen atoms are almost immobile in comparison to hydrogen. Thus the anisotropy of the diffusion of hydrogen defines the particular shape of the front. Further, it was shown, that Ar^+ sputtering has an equalising effect reducing the anisotropy and peculiarity of the surface and thus the differences between reaction front propagation on differently orientated high-index Rh surfaces.

4.1.2 Bistability and kinetic phase diagrams

Since the bistable character of the catalytic H_2 oxidation on Rh single crystals and possibilities to characterise it were already discussed in detail in 2.3 and in 3.2.1.4, only the main principles necessary for interpreting kinetic phase diagrams will be briefly mentioned here. Catalytic reaction systems such as $\text{H}_2/\text{O}_2/\text{Pt}$ can be in two different steady states: the catalytically active state and the catalytically inactive (poisoned) state. A change of parameters, such as temperature or partial pressures, can induce a kinetic transition from one steady state to the other. These transitions are manifested by propagating reaction fronts which can be monitored, e.g. transitions in the CO oxidation on platinum group metals can be studied using PEEM [49, 112–114, 117]. To avoid that other processes, which can change the local work function, such as the segregation of impurities, are mistaken as kinetic transitions, it is necessary to monitor also the reaction production rate and correlate it with the changing PEEM intensity. A series of measurements revealing the transition points τ_A and τ_B at different temperatures but at a constant partial pressure of one reactant can be used to plot a so called kinetic phase diagram in the (p_{H_2}, T) -parameter space. Such a diagram characterises the catalytic activity of the catalyst by showing the regions of low activity, high activity and bistability in a certain parameter range. The kinetic phase diagrams discussed in the following are plotted in p_{H_2} vs. $1/T$ coordinates.

Studies of local reaction kinetics of the CO oxidation on Pt and Pd foils demonstrated, that the catalytic behaviour of differently oriented grains of the same polycrystalline foil differs, since the domain borders confine the spreading of the reaction fronts [120–123]. In turn, in the present study of the H_2 oxidation on a polycrystalline Rh foil, it is not possible to reveal independent kinetic phase diagrams for differently orientated domains since H_2 reaction fronts can propagate unhindered across grain boundaries (see Fig. 4.2 and the corresponding discussion).

Figure 4.5a shows the spreading of the H_2 fronts during the catalytic transition τ_A from the poisoned oxygen covered state to the active reduced state. A comparison of the position of the reaction fronts shown in (a) with the EBSD-map shown in (b) illustrates once more the spreading of fronts across the differently orientated domains of the polycrystalline Rh foil. This transition was monitored during an isothermal measurement at constant oxygen pressure but at cyclewise variation of p_{H_2} . At the beginning of this experiment the temperature and p_{O_2} were set before p_{H_2} was slowly increased. At a certain p_{H_2} the kinetic transition τ_A takes place. The transition was monitored by PEEM (increase of the

4 Experimental results

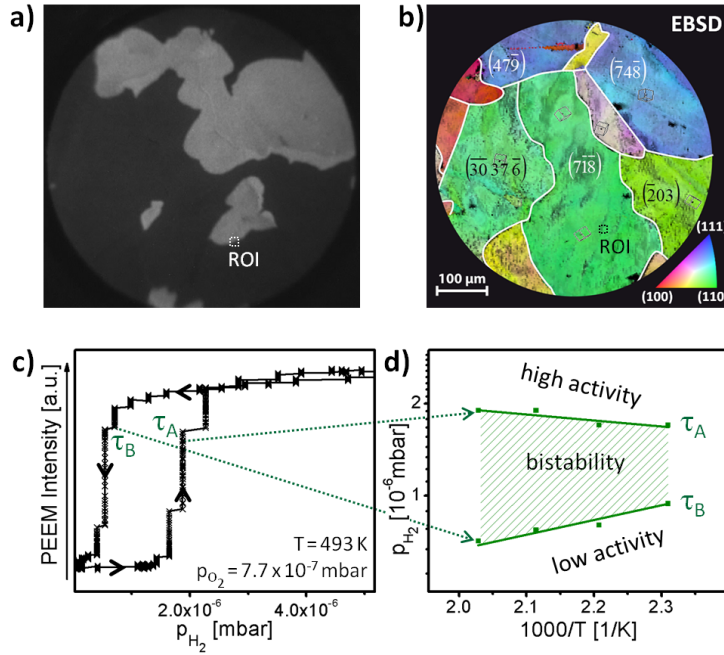


Fig. 4.5. Kinetics by imaging for the H_2 oxidation on the stepped polycrystalline Rh foil: a) PEEM-video frame taken during the kinetic transition τ_A in the H_2 oxidation from the inactive oxygen covered state (dark areas) to the active reduced state (bright areas) at 493 K, $p_{\text{O}_2} = 7.7 \times 10^{-7}$ mbar and $p_{\text{H}_2} = 1.9 \times 10^{-6}$ mbar; b) EBSD map of the studied field of view. Crystallographic orientations of individual domains are indicated; c) Hysteresis plot for the local PEEM intensity measured within the ROI marked in (b) during a cyclic variation of p_{H_2} at constant temperature and constant p_{O_2} . The kinetic transitions τ_A (from the inactive to the active state) and τ_B (from the active to the inactive state) are marked; d) Corresponding kinetic phase diagram. The regions of different catalytic activity and of bistability are marked.

intensity) as well as by the QMS (significant increase of the partial H_2O pressure, which represents the H_2O production rate). After the transition τ_A , the partial hydrogen pressure was reduced until the kinetic transition τ_B occurred, which was also monitored by PEEM as well as by the QMS. Since the two transitions appear at different p_{H_2} , the PEEM intensity forms a hysteresis-like plot in the p_{H_2} vs. "PEEM Intensity" coordinates. Figure 4.5c shows such an intensity-plot for the region of interest (ROI) within the $\text{Rh}(7\bar{1}\bar{8})$ domain, marked in Fig. 4.5b. Since the width of the hysteresis loop might depend on the scan rate of the H_2 pressure ($\frac{dp_{\text{H}_2}}{dt}$) [90] the scan rate was decreased until the obtained hysteresis width became constant. The final scan rate was below $1 \times 10^{-8} \frac{\text{mbar}}{\text{s}}$. From the obtained values τ_A and τ_B the kinetic phase diagram shown in Fig. 4.5d was constructed.

It is generally known, that the surface structure influences the catalytic behaviour of a material significantly. For example, Ar^+ sputtering of a Pd foil does not only change the behaviour of the reaction fronts but also shifts the kinetic phase diagram towards higher

4 Experimental results

p_{CO} , i.e. sputtering increases the tolerance of the catalyst towards poisoning [125]. In the 10^{-5} mbar pressure range a sputtered $Pd(111)$ domain can even behave in the CO oxidation like μm -sized Pd powder particles [131]. This finding leads to the question, how Ar^+ sputtering can change the catalytic behaviour of the Rh foil. To answer this question the Rh foil was sputtered using the same conditions as in the previously described experiment concerning the reaction front velocities on the annealed and the additionally sputtered Rh surface (Fig. 4.4). Using this Ar^+ sputtering conditions should have created artificial defects but despite of the "equalising" sputtering effect, the surface structure should still be dominated by its original shape.

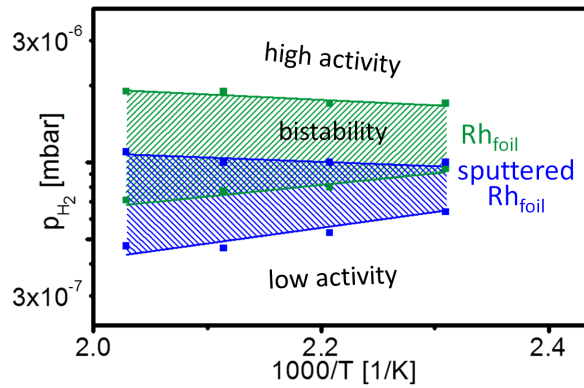


Fig. 4.6. Comparison of the kinetic phase diagrams for the annealed and the Ar^+ sputtered Rh foil: The cleaning procedure of the sputtered foil was the same as for the annealed foil, but extended by sputtering for 15 min using Ar^+ ions of 1 keV energy (*emission current* = 8 μA , p_{Ar} = 1×10^{-5} mbar). The diagram for the sputtered foil is shifted towards lower p_{H_2} . The regions of different catalytic activity and of bistability are marked.

The comparison of the two kinetic phase diagrams shown in Fig. 4.6 reveals the significant change of the catalytic behaviour of the Rh foil due to the sputtering. The diagram of the defect-rich Rh foil is shifted towards lower p_{H_2} values. On the first sight, this seems to be in a contradiction to the structure related shift of the kinetic phase diagram observed in the CO oxidation towards higher p_{CO} [125], but in both cases the shift visualised the increased tolerance towards poisoning (in the H_2 oxidation the oxygen covered surface is inactive). In the present case, the higher tolerance of the sputtered foil towards poisoning may result from the increased sticking coefficient of hydrogen in the presence of steps and defects [132].

4 *Experimental results*

Summary

Since reaction fronts in the H₂ oxidation on the polycrystalline Rh foil spread unhindered across grain boundaries it was not possible to obtain local kinetic phase diagrams for differently orientated domains. The comparison of kinetic phase diagrams for the annealed and for the additionally sputtered Rh foil revealed, in turn, that additional defects increase the tolerance of the Rh surface towards the oxygen caused poisoning in the H₂ oxidation.

4.2 Spatio-temporal oscillations in the hydrogen oxidation on pure rhodium

As previously mentioned in 2.4.2, self-sustaining oscillations in the catalytic H₂ oxidation on Pt, Pd and Ni samples were already reported in literature [72, 73, 76, 133–135]. This reaction can also exhibit an oscillating behaviour on Rh/Ni samples or on sharp Rh field emitter tips in high external electric fields [79, 80, 82, 136]. However, the oscillating H₂ oxidation was not yet observed on pure, low-index Rh single crystal surfaces, on pure Rh foils nor on Rh nanotips under field-free conditions. In the following first results showing the oscillating behaviour of the H₂ oxidation on pure flat Rh surfaces are presented.

4.2.1 PEEM observation of the spatio-temporal oscillations in the hydrogen oxidation on the polycrystalline rhodium foil

The studied polycrystalline Rh foil consists of μm -sized domains, which exhibit different crystallographic orientations. Before each experiment the sample was cleaned using a standard UHV cleaning procedure (Ar⁺ sputtering, annealing and heating in oxygen). The effectiveness of the cleaning procedure was verified by XPS measurements. After cleaning, the sample was heated up to 373 K and exposed to O₂ for 5 min at $p_{\text{O}_2} = 1.1 \times 10^{-6}$ mbar. Then p_{H_2} was varied gradually until the *in situ* monitored H₂ oxidation started to exhibit self-organised oscillations although all external parameters (T , p_{O_2} , p_{H_2}) were kept constant from then on.

Figure 4.7a shows a PEEM-snap shot taken *in situ* during the oscillating H₂ oxidation on the polycrystalline Rh foil. Although the formed pattern, which spreads across the whole field of view, varies within different regions, it always consists of two repetitive elements: the catalytically active reduced surface (bright areas) and the inactive oxygen covered surface (dark areas). The superposition of the oscillation pattern with the EBSD map of the same field of view, shown in Fig. 4.7b, reveals that the regions, where a certain oscillation pattern occurs, are confined by the grain boundaries surrounding differently oriented domains. For example the turbulence-like pattern within the $Rh(\overline{30}37\overline{6})$ domain looks chaotic on the first glance, while the wavy pattern on the $Rh(\overline{2}03)$ domain looks well structured. The temporal evolution of this well-structured pattern within a ROI marked in Fig. 4.7a is illustrated in Fig. 4.7c - f by highlighting the propagation of one reaction-diffusion wave. It is seen that the oscillation pattern shown in 4.7c is restored after 240 s in Fig. 4.7f.

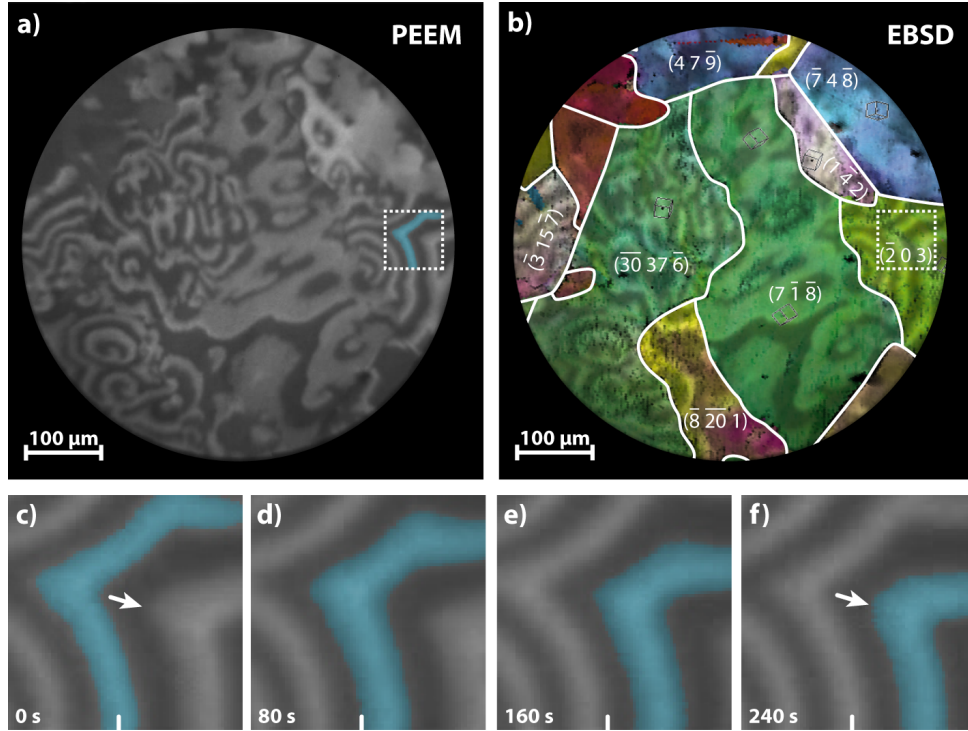


Fig. 4.7. Visualising isothermal oscillations in the catalytic H_2 oxidation on the polycrystalline Rh foil: a) PEEM-video frame taken *in situ* at 453 K , $p_{\text{O}_2} = 1.1 \times 10^{-6}\text{ mbar}$ and $p_{\text{H}_2} = 8.4 \times 10^{-7}\text{ mbar}$ showing the spatial turbulence-like distribution of the two steady states of different catalytic reactivity. The bright areas indicate catalytically active regions while dark areas indicate oxygen poisoned regions; b) Superposition of the oscillation pattern shown in (a) with the EBSD map of the same field of view. Chosen crystallographic orientations of individual domains are indicated; c - f) Temporal evolution of the oscillation pattern within the ROI marked in (a) and (b). The wave-shaped formation shown in (c) recurs after a period of 240 s in (f).

In the following, PEEM observations revealing the role of the surface structure in the appearance of the spatio-temporal oscillations in the H_2 oxidation on Rh and in their frequency are discussed.

4.2.2 The role of the surface structure in the oscillation frequency

Figure 4.7b indicates that differently oriented domains exhibit different oscillation patterns. Thus it makes sense also to compare the local oscillation frequencies for different domains.

The periodic change of the local PEEM brightness within the field of view, shown in Fig. 4.8a, is displayed in Fig. 4.8b and c. Comparing them reveals the significant difference of the oscillation frequencies of the $\text{Rh}(7\bar{1}8)$ and the $\text{Rh}(\bar{3}0\bar{3}7\bar{6})$ domain.

4 Experimental results

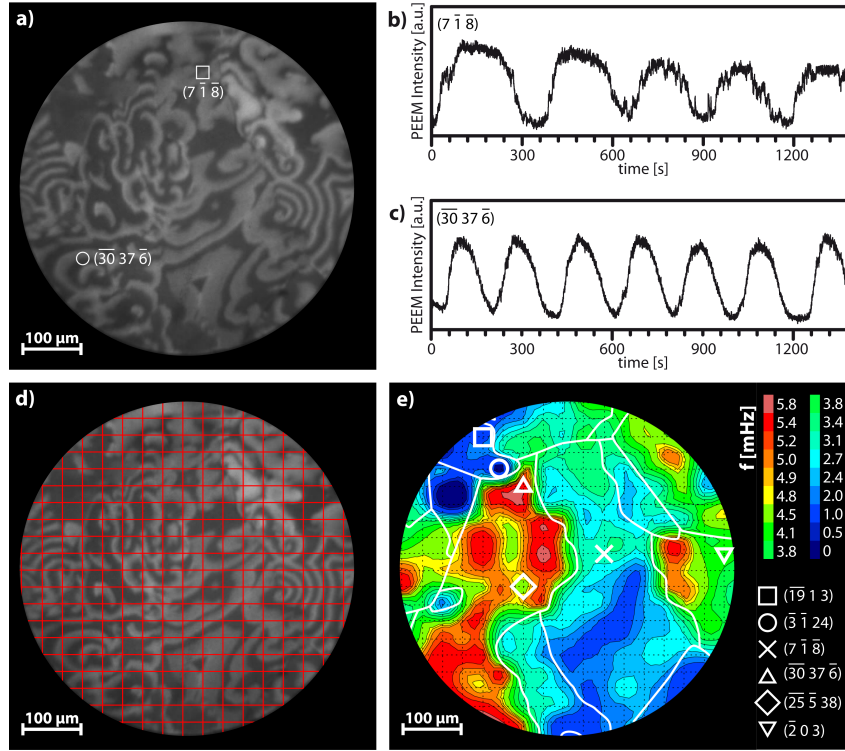


Fig. 4.8. Spatial distribution of the oscillation frequencies in the catalytic H_2 oxidation on the polycrystalline Rh foil: a) PEEM-video frame taken during the H_2 oxidation on the Rh foil under the same conditions as Fig. 4.7a depicting the spatially heterogeneous oscillation pattern; b) Oscillating local PEEM intensity measured within the white square marked in (a); c) The same as (b), but measured within the white circle marked in (a); d) Red coloured virtual line-grid placed above the field of view shown in (a). The local oscillation frequency was evaluated at each intersection point; e) Frequency map illustrating the spatial distribution of these frequencies. The domain borders are marked with white lines and chosen domains are named.

To obtain information about the spatial distribution of the oscillation frequencies within the whole field of view, the local image brightness on each intersection point of a virtual line-grid, that was placed above the field of view as shown in Fig. 4.8d, was analysed. The obtained data is illustrated in the colour-coded map shown in Fig. 4.8e where the crystallographic orientations of several domains, which are confined by the grain boundaries marked as white lines, are indicated. This map reveals that, similar to the pattern formation, the oscillation frequency of the H_2 oxidation also differs on differently oriented domains, i.e. the local oscillating behaviour is related to the surface structure.

To understand this relation, features of the studied Rh surfaces, which may influence the oscillation frequency, should be considered. We suggest to conflate these features into three illustrative structure related parameters, namely the orientation of the predominant terraces, the width of the terraces and the "roughness" of the step edge.

4 Experimental results

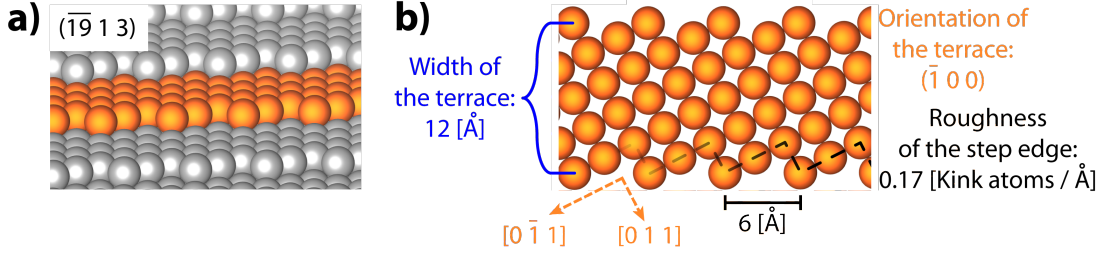


Fig. 4.9. Description of the $Rh(\bar{19} 13)$ surface using three structure related parameters: a) Ball model of the high-index surface with a highlighted terrace; b) Characterising the terrace highlighted in (a) using three parameters: the orientation of the terrace, the width of the terraces and the roughness of the step edge.

The three chosen parameters are illustrated in an example of the $Rh(\bar{19} 13)$ surface in Fig. 4.9. While Fig. 4.9a shows a ball model of the stepped surface, Fig. 4.9b depicts one single terrace of the surface and the three parameters describing it. In the following, the influence of the width of the terraces and the shape of the step edges on the local oscillation frequency is discussed by comparing four surfaces whose terraces exhibit the same crystallographic orientation.

The oscillations of the local image brightnesses for different domains vicinal to the $Rh(110)$ surface, namely the $Rh(7\bar{1}\bar{8})$, the $Rh(\bar{30}\bar{37}\bar{6})$, the $Rh(\bar{25}\bar{5}38)$ and the $Rh(\bar{2}03)$ domain, as well as ball models illustrating their surface structure are shown in Fig. 4.10. First, the catalytic behaviour of the H_2 oxidation on two surfaces, namely the $Rh(7\bar{1}\bar{8})$ and the $Rh(\bar{30}\bar{37}\bar{6})$ surface, which differ only in one parameter, are compared.

Table 4.1. Comparison of the $Rh(7\bar{1}\bar{8})$ with the $Rh(\bar{30}\bar{37}\bar{6})$ surface

Orientation	vicinal	Roughness [<i>Kink atoms</i> /Å]	Width [Å]	f [<i>mHz</i>]
$Rh(7\bar{1}\bar{8})$	$Rh(110)$	0.45	12.4	2.49
$Rh(\bar{30}\bar{37}\bar{6})$	$Rh(110)$	0.45	10.2	6.2

The terraces of both surfaces are vicinals to the $Rh(110)$ surface and the roughness of the step edges is identical. Thus the difference of the corresponding oscillation frequencies can solely result from the different widths of their terraces. The smaller width of the terraces the $Rh(\bar{30}\bar{37}\bar{6})$ surface consists of leads to a higher oscillating frequency.

In turn, the comparison of the $Rh(\bar{25}\bar{5}38)$ and the $Rh(\bar{2}03)$ domain reveals the influence of the roughness of the step edges on the oscillation frequency.

For this two domains only the orientation of the terraces is identical, i.e. both domains are vicinals to the $Rh(110)$ surface. According to the results presented above, the H_2 oxidation should oscillate with a higher frequency on the $Rh(\bar{2}03)$ domain, since the width

4 Experimental results

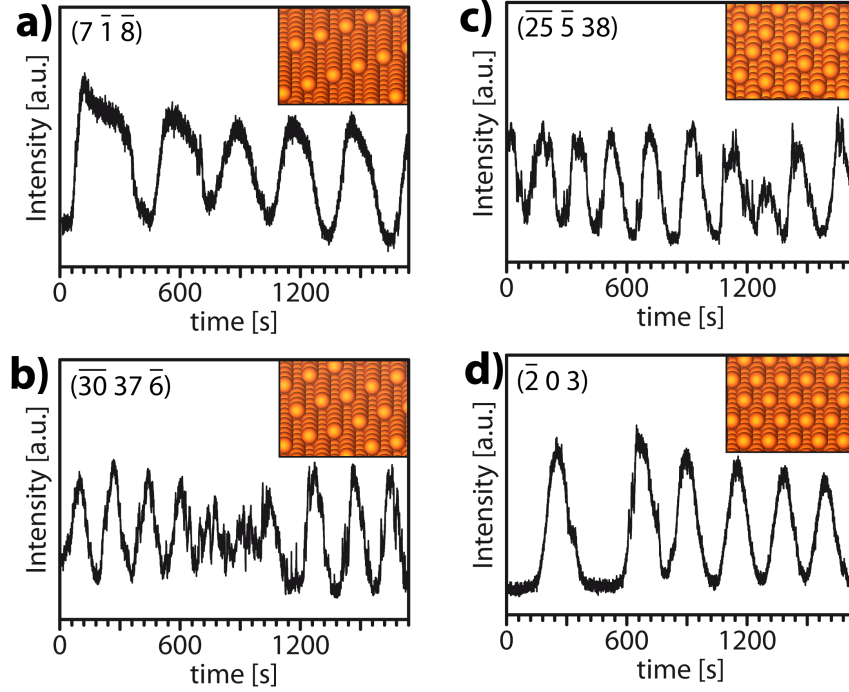


Fig. 4.10. Oscillations in the H_2 oxidation on different vicinal $\text{Rh}(110)$ surfaces: a) Oscillating local PEEM intensity measured on the $\text{Rh}(7\bar{1}\bar{8})$ domain of the Rh foil at 453 K , $p_{\text{O}_2} = 1.1 \times 10^{-6}\text{ mbar}$ and $p_{\text{H}_2} = 8.4 \times 10^{-7}\text{ mbar}$. The upper right inset shows a ball model of the surface; b) to d) The same as (a), but for the $\text{Rh}(30\bar{3}7\bar{6})$, the $\text{Rh}(25\bar{5}38)$ and the $\text{Rh}(2\bar{0}3)$ domain.

Table 4.2. Comparison of the $\text{Rh}(25\bar{5}38)$ with the $\text{Rh}(2\bar{0}3)$ surface

Orientation	vicinal	Width [\AA]	Roughness [$\text{Kink atoms}/\text{\AA}$]	f [mHz]
$\text{Rh}(25\bar{5}38)$	$\text{Rh}(110)$	7.5	0.41	4.48
$\text{Rh}(2\bar{0}3)$	$\text{Rh}(110)$	5.4	0	3.79

of the terraces of the $\text{Rh}(2\bar{0}3)$ domain is smaller than that of the $\text{Rh}(25\bar{5}38)$ surface. However, the frequency on the $\text{Rh}(2\bar{0}3)$ surface is lower. This result can be explained if the different shape of the step edges is also considered. The steps of the $\text{Rh}(25\bar{5}38)$ are kinked while those of the $\text{Rh}(2\bar{0}3)$ domain are far smoother, or to be more exactly kink-less. It seems, that in this particular case the difference in the roughness of the edges overrules the influence of the width of the terraces.

Summary

Self-sustaining oscillations of the local PEEM image brightness, which indicate a periodic change of the local reaction rate, were observed *in situ* in the H_2 oxidation on a poly-

4 Experimental results

crystalline Rh foil. Analysing the occurring patterns and the frequency map lead to the insight, that both, the pattern formation and the oscillation frequency, are influenced by the local surface structure. The presented results indicate that the catalytic H_2 oxidation may oscillate with a higher frequency on highly stepped and kinked vicinal $Rh(110)$ surfaces than on a surface consisting of wide, kink-less $Rh(110)$ terraces. A too smooth surface could probably even inhibit the oscillations in the H_2 oxidation on Rh.

4.2.3 The formation of the oscillation pattern

As already mentioned in 4.2.1, during the H_2 oxidation different oscillation patterns appear on differently oriented domains of the polycrystalline Rh foil. In this section the formation of the occurring patterns is addressed. It is reasonable first to consider the origin of the reaction-diffusion waves these patterns consist of.

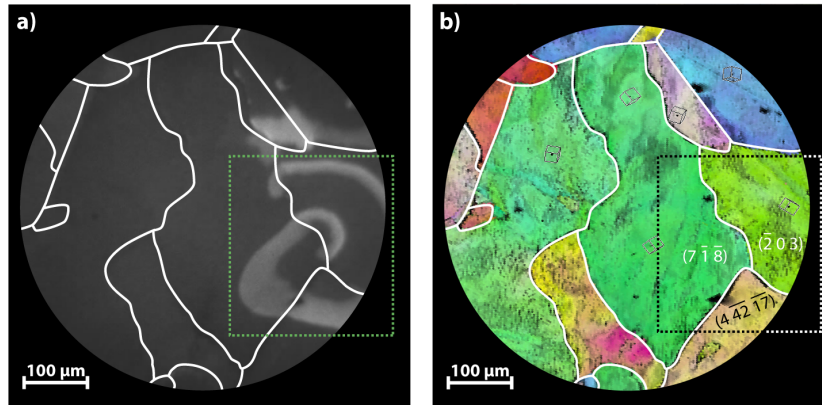


Fig. 4.11. Pattern formation at a single nucleation center in the H_2 oxidation on the Rh foil: a) PEEM-video frame showing the spreading of the spiral shaped pattern originating from a single nucleation center at 453 K , $p_{\text{O}_2} = 7.7 \times 10^{-7}\text{ mbar}$ and $p_{\text{H}_2} = 5.5 \times 10^{-7}\text{ mbar}$; b) Corresponding EBSD map of the field of view shown in (a). Three crystallographic orientations are indicated.

The nucleation and propagation of a single reaction-diffusion front could be observed at slightly different hydrogen pressure than that leading to the oscillations described above. At 453 K , $p_{\text{O}_2} = 7.7 \times 10^{-7}\text{ mbar}$ and $p_{\text{H}_2} = 5.5 \times 10^{-7}\text{ mbar}$ the observed bright spiral spreads over three domains, as shown in Fig. 4.11a. In the EBSD-map, shown in Fig. 4.11b, the orientations of the domains the spiral spreads across, namely the $Rh(7\bar{1}8)$, the $Rh(\bar{2}03)$ and the $Rh(442\bar{1}7)$ domain, are marked. Thus Fig. 4.11a also illustrates, that the width, the radius and the velocity of the spreading front change significantly as

4 Experimental results

the front spreads from the $Rh(\bar{2}03)$ to the $Rh(7\bar{1}\bar{8})$ domain, i.e. that the local surface structure influences the propagation behaviour of the reaction front.

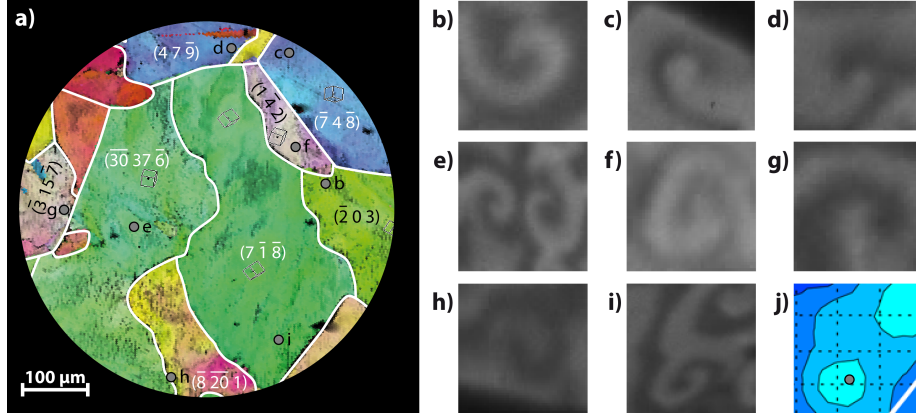


Fig. 4.12. Pattern formation at multiple nucleation centers: a) EBSD map of the studied field of view. Crystallographic orientations of individual domains are indicated; b-i) Magnified sectors of different PEEM-video frames, which were all taken within one experiment (453 K , $p_{O_2} = 1.1 \times 10^{-6}\text{ mbar}$ and $p_{H_2} = 8.4 \times 10^{-7}\text{ mbar}$). The sectors show spiral shaped patterns formed at nucleation centers, which are marked in (a); j) Part of the frequency map, which is entirely shown in Fig. 4.8e, visualising the local distribution of the oscillation frequencies within the area shown in (i). The nucleation center is marked as gray spot while the white line illustrates the grain boundaries.

Spiral shaped patterns were also observed on nearly all domains within the studied field of view during the ongoing oscillations at 453 K , $p_{O_2} = 1.1 \times 10^{-6}\text{ mbar}$ and $p_{H_2} = 8.4 \times 10^{-7}\text{ mbar}$. The corresponding nucleation centers of chosen spirals are marked in the EBSD map shown in Fig. 4.12a while magnified sectors of PEEM images depicting these spirals are illustrated in Fig. 4.12b - i. Figure 4.12e also shows, that spirals might nucleate at multiple centers within one domain. Since the spirals spread across domain borders, as already shown in Fig. 4.11, the observed oscillations on differently oriented domains are coupled. Further, the comparison of sectors of PEEM images depicting spirals with the corresponding regions of the oscillation-map reveals information about the spatial distribution of the oscillation frequencies close to nucleation centers, as exemplary shown in Fig. 4.12i and j. One spiral nucleates in the center of the magnified region shown in Fig. 4.12i while another one nucleates close to the top right corner. The comparison of this region, shown in Fig. 4.12i, with the corresponding sector of the frequency map, shown in Fig. 4.12j, reveals that at the nucleation centers of the spirals the highest oscillation frequencies were observed (light blue areas in Fig. 4.12j) while the overlap of waves significantly decreases the local oscillation frequency (darker blue areas in Fig. 4.12j).

4 Experimental results

Since the unhindered spreading of reaction fronts seems to lead to spiral shaped patterns, the overlap of spirals might lead to the other two dominating patterns visible in the already shown PEEM-images: wave-like patterns and chaotic turbulence-like structures. In the following the pattern formation in regions, where fronts originating from different numbers of nucleation centers contribute to the occurring patterns, is discussed exemplary by addressing sectors within the $Rh(\bar{3}15\bar{7})$, the $Rh(\bar{2}03)$ and the $Rh(\bar{3}037\bar{6})$ domain.

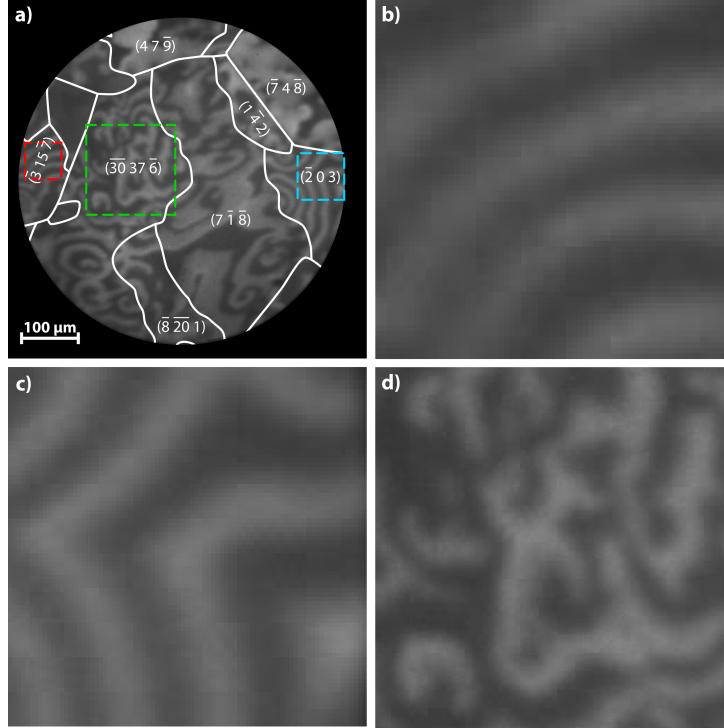


Fig. 4.13. Formation of complex patterns during the oscillating H_2 oxidation on the Rh foil: a) PEEM-video frame showing the spatial turbulence-like distribution of the two states of different catalytic activity taken at 453 K , $p_{O_2} = 1.1 \times 10^{-6}\text{ mbar}$ and $p_{H_2} = 8.4 \times 10^{-7}\text{ mbar}$. The domain borders are marked by white lines and chosen crystallographic orientations are indicated; b) Magnified area marked in (a) as a red square. The reaction fronts propagate unhindered as a wave-like pattern; c) Magnified region marked in (a) as a blue square. The pattern is formed by the overlap of reaction fronts originating from three nucleation centers; d) Magnified sector marked in (a) as a green square. The overlap of multiple reaction fronts forms a complex turbulence-like pattern.

The three regions marked within the PEEM-video frame shown in Fig. 4.13a depict clearly distinguishable patterns of different complexity. The magnified region marked within the $Rh(\bar{3}15\bar{7})$ domain, shown in Fig. 4.13b, illustrates the unhindered propagation of a wave-like pattern originating from a single spiral, whose nucleation center is located right below the lower right corner of the red square marked in Fig. 4.13a. The magnified sector

4 Experimental results

shown in Fig. 4.13c depicts the more complex pattern within the $Rh(\bar{2}03)$ domain, which is formed by the overlap of wave-like fronts nucleating at three different spots. These nucleation centers are located in Fig. 4.13a on the domain border between the $Rh(\bar{2}03)$ and the $Rh(7\bar{1}\bar{8})$ domain (next to the lower left corner of the blue square), on the grain boundary between the $Rh(\bar{2}03)$ and the $Rh(1\bar{4}2)$ domain (next to the upper left corner of the blue square) and at the border between the $Rh(\bar{2}03)$ and the $Rh(\bar{7}4\bar{8})$ domain (close to the upper right corner of the blue square). The even more complex pattern, including parts of several spiral shaped and wave-like patterns, shown in Fig. 4.13d, was observed within a region inside the $Rh(\bar{3}0\bar{3}7\bar{6})$ domain. For example a part of a bright spiral can be seen in the lower left corner of the green square marked in Fig. 4.13a. In summary, it can be said that the complexity of the oscillation pattern increases significantly with the density of nucleation centers.

Summary

Self-sustaining spiral shaped oscillation patterns in the catalytic H_2 oxidation on Rh were observed. While a single spiral leads to the spreading of a wave-like pattern, the overlap of multiple spirals originating from different nucleation centers might lead to complex turbulence-like patterns. Further, it was shown that the overlap of fronts originating from different nucleation centers decreases the local oscillation frequency, i.e. the highest frequency within a domain can be observed at nucleation centers of spiral shaped waves.

4.2.4 Guiding oscillations through geometry

As already discussed in 4.1.1 and 4.2.3, the grain boundaries enclosing differently oriented domains of the polycrystalline Rh foil can not confine propagating reaction fronts. Further, in 4.2.2 the assumption was made, that the catalytic H_2 oxidation can not oscillate on too flat Rh surfaces. Thus low-index surfaces consisting of wide kink-less terraces can probably confine regions exhibiting an oscillating behaviour. To prove this assumption, a mesoscopic defect on a $Rh(111)$ single crystal was used as confined region, which consists of rough, defect-rich surfaces. According to the obtained results, the rough Rh surfaces might exhibit an oscillating behaviour while the flat $Rh(111)$ single crystal surface should not oscillate.

A PEEM-image of the mesoscopic defect on the $Rh(111)$ single crystal surface is shown in Fig. 4.14a. To reveal more details about the shape of the defect AFM measurements were performed by co-workers from the USTEM. As shown in Fig. 4.14b, the furrow-like

4 Experimental results

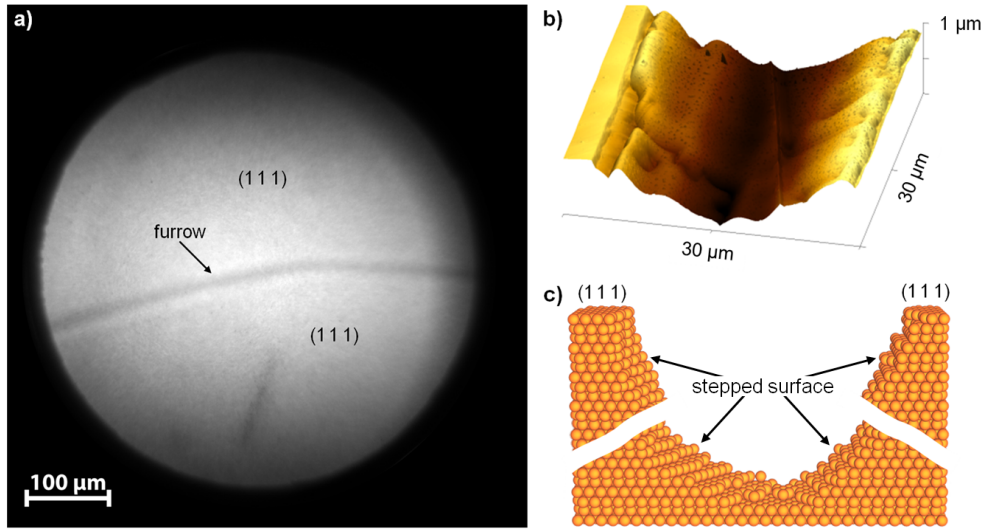


Fig. 4.14. Mesoscopic defect on the $Rh(111)$ single crystal: a) PEEM-image showing the $30\ \mu\text{m}$ -wide furrow separating the upper and the lower half of the studied field of view; b) AFM-image illustrating the profile of the furrow; c) Schematic model of the profile shown in (b) illustrating that the side walls of furrows exhibit stepped surfaces while smooth $[111]$ oriented surfaces confine the defect.

shaped defect is approximately $30\ \mu\text{m}$ wide and nearly $1\ \mu\text{m}$ deep. Although the AFM cannot image the side walls of the furrow with atomic resolution, they obviously consist of stepped surfaces, as illustrated by the schematic drawing shown in Fig. 4.14c.

Like the Rh foil, the Rh single crystal was also cleaned using a standard UHV cleaning procedure. The effectiveness of the procedure was verified by XPS measurements. The experiments of the single crystal study were carried out analogously to those of the Rh foil study.

A snap shot of the ongoing H_2 oxidation on the single crystal sample is shown in Fig. 4.15a while Fig. 4.15b illustrates the temporal evolution of the local PEEM image intensities obtained within five different ROIs. Three of them are placed within the furrow (marked in Fig. 4.15a as "ROI 1", "ROI 2" and "ROI 3") while the other two are placed on the flat $Rh(111)$ surface (marked in Fig. 4.15a as "top" and "bottom"). As it is seen in Fig. 4.15b, the local image brightness within the stepped furrow changes periodically in all three ROIs, but the local oscillation frequencies differ. These differences might be related to disparities in the surface structure of the side walls of the defect. In turn, outside the furrow the H_2 oxidation does not exhibit an oscillating behaviour at all.

4 Experimental results

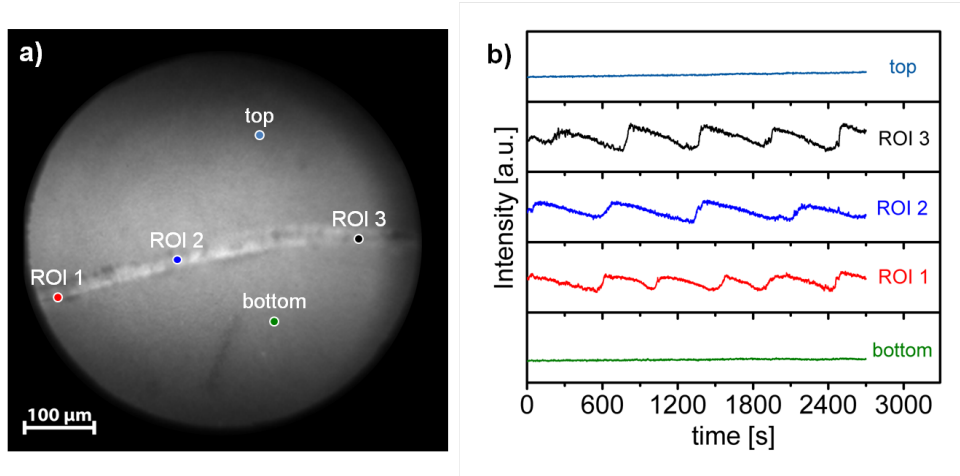


Fig. 4.15. Spatio-temporal behaviour of the catalytic hydrogen oxidation on the $Rh(111)$ single crystal sample: a) PEEM-video frame taken at 433 K , $p_{O_2} = 1.1 \times 10^{-6}\text{ mbar}$ and $p_{H_2} = 8.4 \times 10^{-7}\text{ mbar}$; b) Local PEEM intensities measured within the marked ROIs in (a) illustrating that the oscillation frequency varies within the furrow while no oscillations occur outside the furrow.

Summary

It was shown, that oscillations in the H_2 oxidation on Rh can be confined within a mesoscopic defect on a flat $Rh(111)$ surface. The oscillations were observed only on the stepped side walls of the furrow, at least under the studied conditions. This insight is in agreement with the assumption made in 4.2.2, that the oscillating behaviour of the H_2 oxidation on Rh might be inhibited by insufficient roughness of the Rh surface.

4.2.5 Structural limits for the existence of oscillations

The insight, that the H_2 oxidation oscillates on stepped high-Miller-index but not on flat single crystal Rh surfaces, indicates the existence of a certain structural limit for the oscillating behaviour. The comparison of the catalytic behaviour of the H_2 oxidation on two vicinal $Rh(100)$ surfaces, namely on the $Rh(\overline{19}13)$ and on the $Rh(\overline{3}\overline{1}24)$ surface, which were both marked in Fig. 4.8e, might reveal further insights into this limitation.

Figure 4.16a and b show the temporal evolution of the local image brightness for the $Rh(\overline{19}13)$ and the $Rh(\overline{3}\overline{1}24)$ domain. The corresponding ball models illustrating their surface structures are placed in the top right corners of Fig. 4.16a and b. On the $Rh(\overline{19}13)$ surface the local image brightness changes periodically, as shown in 4.16a, while the image brightness on the $Rh(\overline{3}\overline{1}24)$ surface, shown in 4.16b, does not change significantly. On the other hand it cannot be excluded that the PEEM intensity measured on the

4 Experimental results

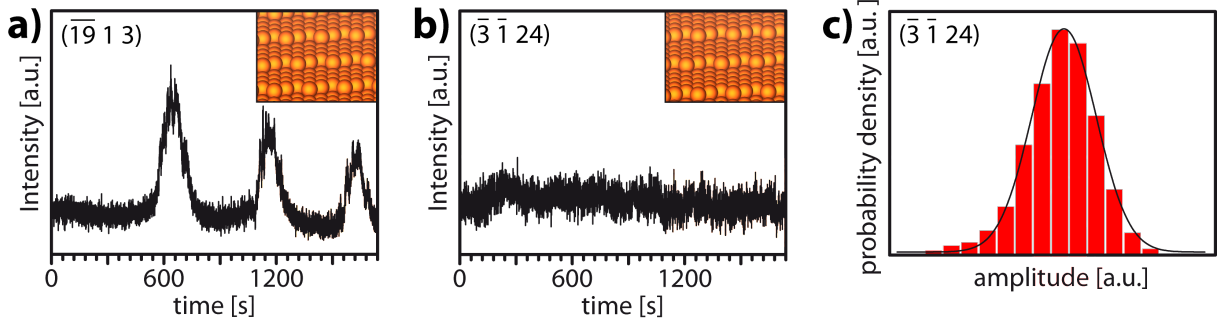


Fig. 4.16. Temporal evolution of the local PEEM intensities on different vicinal $Rh(100)$ surfaces: a) Oscillating local PEEM intensity measured within the $Rh(\overline{19}13)$ domain of the Rh foil during the catalytic H_2 oxidation at 453 K , $p_{O_2} = 1.1 \times 10^{-6}\text{ mbar}$ and $p_{H_2} = 8.4 \times 10^{-7}\text{ mbar}$. The inset in the upper right part shows a ball model of the surface; b) The same as (a) but for the $Rh(\overline{3}124)$ domain; c) Probability density distribution of the amplitude of the signal shown in (b). The data points were fitted using a Gaussian bell with a FWHM of 0.08399.

$Rh(\overline{19}13)$ domain oscillates but its amplitude is too small or its frequency is too high to be seen on the shown graph with the naked eye. To clarify this uncertainty, a probability distribution of the amplitude from the data shown in Fig. 4.16b was calculated. If the signal oscillates, the corresponding probability distribution would reveal two maxima (one corresponding to the high image brightness, i.e. to the catalytically active state, and one corresponding to the low one, i.e. to the catalytically inactive state). However, since the calculated probability distribution illustrated in Fig. 4.16c shows only one maximum and since the obtained data points can be fitted using a Gaussian bell, it is proven that the variation of the amplitude exhibits rather a stochastic than an oscillating behaviour. Thus the comparison of the $Rh(\overline{19}13)$ surface with the $Rh(\overline{3}124)$ proves that structural properties, which limit the oscillating behaviour of the catalytic H_2 oxidation on vicinal $Rh(100)$ surfaces, indeed exist. Since all three structure parameters (the crystallographic orientation of the predominant terraces, the width of the terraces and the roughness of the step edges) influence the oscillation frequency, it seems reasonable that the restriction of the oscillating behaviour is also related to a combination of all three parameters. This limit can be specified in this particular case by analysing the differences of the structure related parameters of the $Rh(\overline{19}13)$ and the $Rh(\overline{3}124)$ surface.

Table 4.3. Comparison of the $Rh(\overline{19}13)$ with the $Rh(\overline{3}124)$ surface

Orientation	vicinal	Roughness [<i>Kink atoms</i> / \AA]	Width [\AA]	f [mHz]
$Rh(\overline{19}13)$	$Rh(100)$	0.17	12.0	2.17
$Rh(\overline{3}124)$	$Rh(100)$	0.17	14.4	0

4 Experimental results

The roughness of the step edges of the $Rh(\overline{19}13)$ and the $Rh(\overline{3}\overline{1}24)$ domain is identical and both surfaces are vicinals to the $Rh(100)$ surface. Thus the difference in the oscillating behaviour can solely be addressed to the different widths of the terraces. In this particular case, the combination of the orientation of the terraces, the shape of the step edges and the width of 12 \AA enables oscillations in the H_2 oxidation, while an expansion of the width by 2.4 \AA leads to an inhibition of the oscillating behaviour. Thus, for this particular case, the oscillation limit in the form of the width of the terraces could be determined with an accuracy of a few \AA . It is important to mention here, that the dimension of this restriction probably is not valid for a vicinal $Rh(100)$ surface exhibiting step edges of a different roughness than those of the $Rh(\overline{19}13)$ and for vicinals of the $Rh(110)$ or the $Rh(111)$ surface.

Since changes of the partial H_2 pressure significantly influences the anisotropy of the reaction front propagation in the H_2 oxidation on $Rh(110)$ [137], it seems reasonable that the external parameters (T , p_{O_2} and p_{H_2}) might also affect the local oscillating behaviour.

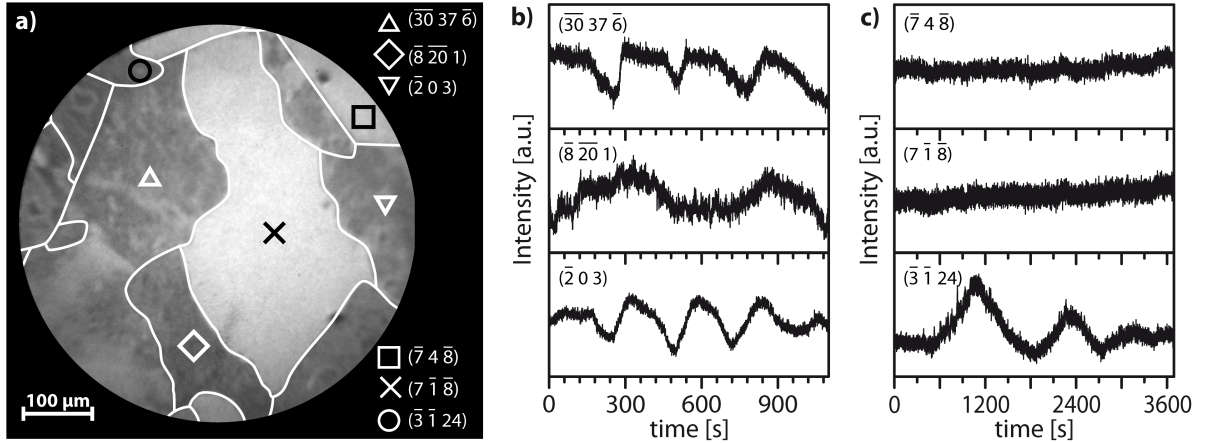


Fig. 4.17. Visualising isothermal oscillations in the catalytic H_2 oxidation on several domains of the polycrystalline Rh foil: a) PEEM-image taken *in situ* during the catalytic H_2 oxidation at 453 K , $p_{O_2} = 1 \times 10^{-6} \text{ mbar}$ and $p_{H_2} = 1.1 \times 10^{-6} \text{ mbar}$; b-c) Temporal evolution of the local image brightness within several domains of the Rh foil. The corresponding domains are marked in (a).

It was already reported in 4.2.3, that the H_2 oxidation oscillates at 453 K , $p_{O_2} = 1.1 \times 10^{-6} \text{ mbar}$ and $p_{H_2} = 8.4 \times 10^{-7} \text{ mbar}$ nearly within the whole field of view (the only exception is the $Rh(\overline{3}\overline{1}24)$ domain). Further in 4.2.3 was discussed, that lowering p_{H_2} while the other two external parameters (T and p_{O_2}) are kept constant, enabled to observe the nucleation of a single bright spiral on the mainly oxygen covered Rh surface. In turn,

4 Experimental results

increasing p_{H_2} while the temperature is kept constant and p_{O_2} is slightly lowered, leads to the formation of a chaotic-like oscillation pattern on several domains of the Rh foil while other regions remain in the reduced state, as shown in Fig. 4.17a. For example, the local intensity oscillates within the $Rh(\overline{30}37\overline{6})$, the $Rh(\overline{8}201)$ and the $Rh(\overline{2}03)$ domain also under this conditions as seen in Fig. 4.17b, although their frequencies differ from those obtained on the same three domains at the different conditions, which were discussed in the previous sections. An even more prominent change of the catalytic behaviour can be observed on three other domains. While the H_2 oxidation can oscillate on the $Rh(\overline{3}\overline{1}24)$ domain under this conditions, it can not oscillate any more on the $Rh(\overline{7}4\overline{8})$ and the $Rh(7\overline{1}\overline{8})$ domain, as seen in Fig. 4.17c. Analogous to the already discussed case of the vicinal $Rh(100)$ surfaces, the non-existence of the oscillations was proven by calculating and analysing the probability distributions of the amplitudes.

Comparing the catalytic behaviour on the $Rh(\overline{30}37\overline{6})$ and the $Rh(7\overline{1}\overline{8})$ domain reveals a structural limit for the existence of oscillations, which is valid under this particular conditions. In 4.2.2 was already discussed, that the terraces of these domains exhibit the same orientation and that their step edges are shaped identical. Thus, for this particular case, the oscillation limit in the form of the width of the terraces could be determined with an accuracy of 2.2 \AA .

Summary

The existence of structural properties necessary for the oscillating behaviour in the H_2 oxidation on Rh was proven by comparing the catalytic behaviour of two vicinal $Rh(100)$ and two vicinal $Rh(110)$ surfaces. In both cases the terraces of the two domains exhibit the same orientation and the shape of the step edges was identical. Thus, the structural limit in the form of the width of the terraces could be circumscribed for this two particular cases with an accuracy of only a few \AA . Further it was shown, that such limits are valid for a certain set of the external parameters (T , p_{O_2} and p_{H_2}). The results obtained for vicinal $Rh(100)$ and vicinal $Rh(110)$ surfaces indicate, that oscillations on pure Rh surfaces might be inhibited when their surfaces consist of too wide (and probably also kink-less) terraces, at least under the present conditions.

4.3 Spatio-temporal behaviour of the catalytic hydrogen oxidation on different scales

As already mentioned in 1.3, modern commercial catalysts usually consist of metal nanoparticles supported by different oxides. The nm-sized facets of such particles show a remarkable catalytic activity because their surfaces exhibit a high density of low-coordinated step atoms [138]. Similar to such particles, the Rh foil studied in the present work also consists of high-index surfaces, which are made up of stepped and kinked terraces exhibiting lots of low-coordinated atoms. However, a nanosized field emitter tip with a hemispherical apex made from a catalytically active metal is an even more suitable model for a catalytic nanoparticle since it has, in addition, the proper size. Further, the facets of particles and field emitter tips are, in contrast to a polycrystalline foil, not separated by grain boundaries. Moreover, unlike a nano-sized particle of a commercial catalyst, a nanotip can be characterised with atomic resolution by field-ion microscopy (FIM). Furthermore the ongoing reactions can be visualised *in situ* by FIM [139] or field-emission microscopy (FEM) [140]. Thus the spatio-temporal behaviour of catalytic reactions can be investigated in this way on a well-defined properly sized surface.

The comparison of results concerning the H_2 oxidation on μm -sized domains of the Rh foil, which were already presented in the previous chapters with those obtained for the nm-sized Rh tip allows to address the size-effect, i.e. the influence of the sample size on the catalytic reactivity.

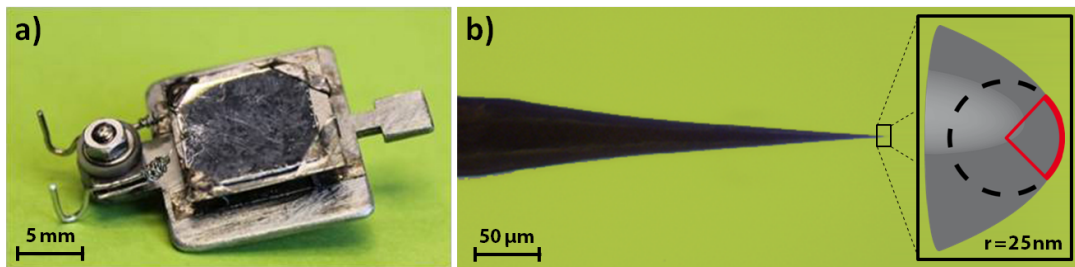


Fig. 4.18. Differently scaled Rh samples: a) Mesoscopic Rh foil; b) Rh nanotip exhibiting an apex, which serves as model of a nano particle.

Figure 4.18 shows two different model catalysts, namely the Rh foil and a Rh nanotip, which are compared within this section. The tip was studied using an apparatus with a base pressure of 2×10^{-9} mbar. It consists of a FIM-chamber with a tip assembly, which allows to perform experiments in the temperature range of $78 - 900$ K, a gas-supply

4 Experimental results

system (Ne, H₂, O₂) and a channel-plate/screen set-up used for imaging the tip surface either with field emitted electrons (FEM) or with field-ions (FIM). The screen can be monitored using a high speed CCD-camera (Hamamatsu C9300). For studying the H₂ oxidation on a Rh nanotip the FIM-chamber was used as a differentially pumped flow reactor.

The studied Rh tip was fabricated by sharpening a Rh wire (0.12 mm diameter, Goodfellows, 99.9 % purity) by electrochemical etching. In UHV the tip was further shaped by field evaporation at 77 K under Ne⁺ FIM image control whereby the temperature was controlled using a Ni/CrNi thermocouple. Before each experiment, the sample was additionally cleaned by field desorption at 373 K.

In the present FEM studies electrostatic field values of less than 5 V/nm were used. On the first sight 5 V/nm seems to be a quite high field strength, but since the tip surface during FEM measurements is charged negatively, the onset of field emission of electrons is achieved at field strengths far below values at which field induced modifications of the electron density can occur [141]. Thus, the present FEM measurements can be considered as quasi field-free.

In contrast to PEEM, which can only be used to study a small part of the Rh foil, FEM and FIM image the whole apex of the studied nanotip. Exemplary a PEEM- and a FEM-image of the Rh samples are shown in Fig. 4.19a and b.

As already discussed in 3.3.2, in the case of the polycrystalline Rh foil EBSD was used to obtain information about the crystallographic orientations of individual domains, which can be summarised in the map shown Fig. 4.19c. In the case of the nanotip, atomically resolved FIM-images were used to identify the crystallographic orientation of the facets enclosing the Rh tip. Such a Ne⁺ FIM image of the clean Rh nanotip, where chosen facets are indicated, is shown in Fig. 4.19d.

If the crystallographic orientations of the domains and facets are known, their surface structures can be illustrated using ball models. Figure 4.19e depicts the surface structure of the $Rh(7\bar{1}\bar{8})$ domain while the surface structure of the whole apex of the nanotip is illustrated in Fig. 4.19f by the spherical ball model, which was constructed on the basis of atomically resolved FIM images.

Since the image brightness of both, PEEM and FEM, is related to the local work function, the *kinetics by imaging* approach can also be applied to FEM studies (for further details see 3.2.1.4). Thus, the H₂ oxidation on the Rh tip could be studied in the same manner as it was done for the Rh foil but since in the studied temperature range the diffusion length

4 Experimental results

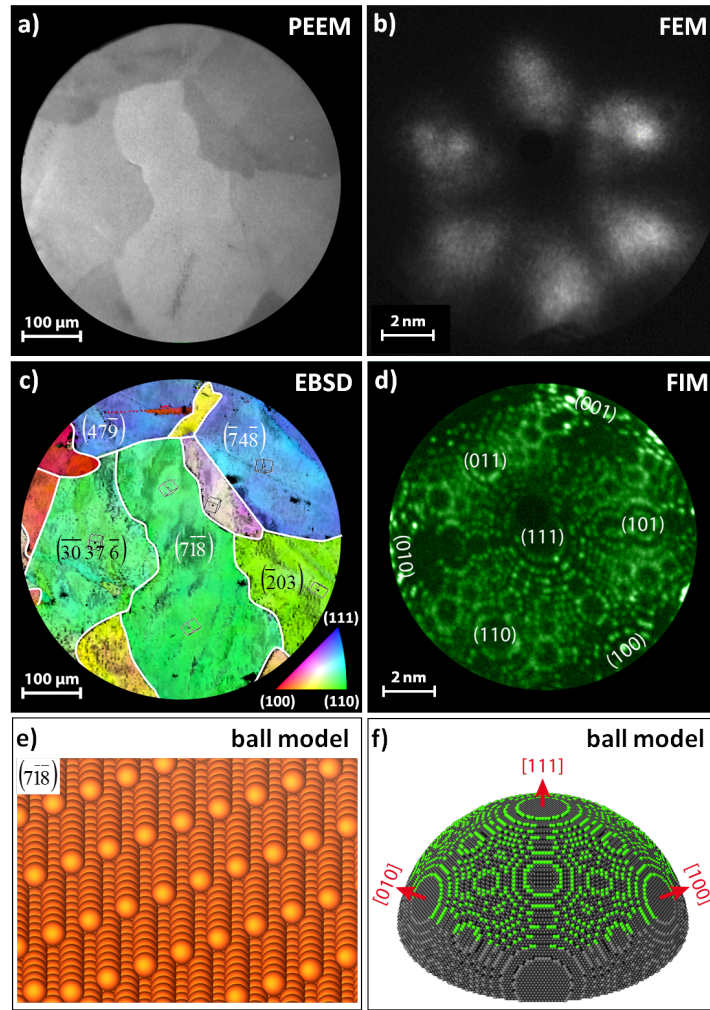


Fig. 4.19. Two differently scaled model systems: a) PEEM-image of a clean polycrystalline Rh foil surface consisting of differently oriented μm -sized domains; b) FEM-image of the clean Rh nanotip taken at 433 K and 5 V/nm . The clean $[1\ 1\ 1]$ -oriented tip exhibits a threefold symmetry; c) Colour-coded EBSD map of the same region as shown in (a) where chosen crystallographic orientations of the high-Miller-index domains are marked. The inverse pole figure is shown as reference in the bottom right corner; d) Atomically resolved Ne^+ FIM image of the Rh nanotip taken at 77 K and an applied field of 35 V/nm . Chosen crystallographic orientations of the differently oriented facets are indicated; e) Ball model of the surface structure of the $Rh(7\bar{1}\bar{8})$ domain; f) Spherical ball model of the Rh tip based on FIM images. The protruding atoms visible in the FIM micrograph shown in (d) are marked green.

of hydrogen is significantly larger (μm -range) than the facet sizes of the apex (nm-range) [127], kinetic transitions seem to occur simultaneously on all facets of the tip.

Similar to the PEEM-study discussed in 4.1.2, isothermal FEM measurements at constant p_{O_2} and at a cyclewise variation of p_{H_2} lead to hysteresis plots for the FEM intensity, which

4 Experimental results

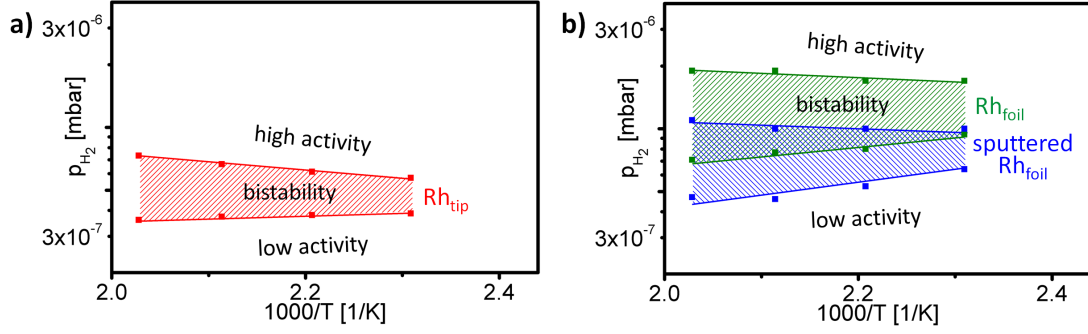


Fig. 4.20. Kinetic phase diagrams for differently scaled Rh samples: a) Kinetic phase diagram for the Rh nanotip measured at a constant oxygen pressure of 7.7×10^{-7} mbar. The regions of different catalytic activity and of bistability are marked; b) Kinetic phase diagrams for the annealed and the sputtered Rh foil, as already shown in Fig. 4.6. Both diagrams for the foil are valid for the same p_{O_2} and the same temperature range as (a).

were used to obtain the kinetic phase diagram shown in Fig. 4.20a. The comparison of the the kinetic phase diagram for the Rh nanotip, shown in Fig. 4.20a, with the kinetic phase diagrams for the annealed and the additionally sputtered Rh foil, shown in Fig. 4.20b, reveals, that the diagram of the tip is shifted towards lower p_{H_2} than those for the annealed and the sputtered Rh foil, i.e. that the Rh tip exhibit an even higher tolerance towards the poisoning effect of oxygen. The shift of the diagrams of the differently treated foils was explained in 4.1.2 by the increased sticking coefficient of hydrogen in the presence of steps and defects [132]. The additional shift of the diagram for the Rh tip can be explained in the same way. According to the FIM-image and the ball model shown in Fig 4.19d and f, the density of low-coordinated step- and kink atoms on the highly curved apex of the Rh tip is higher than that on the sputtered Rh foil, whose surface, as discussed in 4.1.1, seems to be (despite of the "equalising" sputtering effect) still dominated by the terraces forming the surfaces of the domains.

As already mentioned in 2.1, besides the bistable behaviour of the H_2 oxidation the oscillation mode was also observed earlier in FIM on sharp Rh field emitter tips in high external electric fields ($> 10 \frac{V}{nm}$) [82, 136]. The essential role of the external electric field in these observations is described in literature [82, 136]. As feedback mechanism serves the field induced formation of subsurface oxygen/surface oxide [142].

However, the catalytic H_2 oxidation on a Rh nano tip can also exhibit an oscillating behaviour under quasi field-free conditions although the external parameters ($T = 433$ K, $p_{O_2} = 1.1 \times 10^{-6}$ mbar and $p_{H_2} = 8.4 \times 10^{-7}$ mbar) are kept constant.

The comparison of the oscillations in the H_2 oxidation on the two differently sized samples reveals significant differences. Figure 4.21a shows the individual pattern formation on each

4 Experimental results

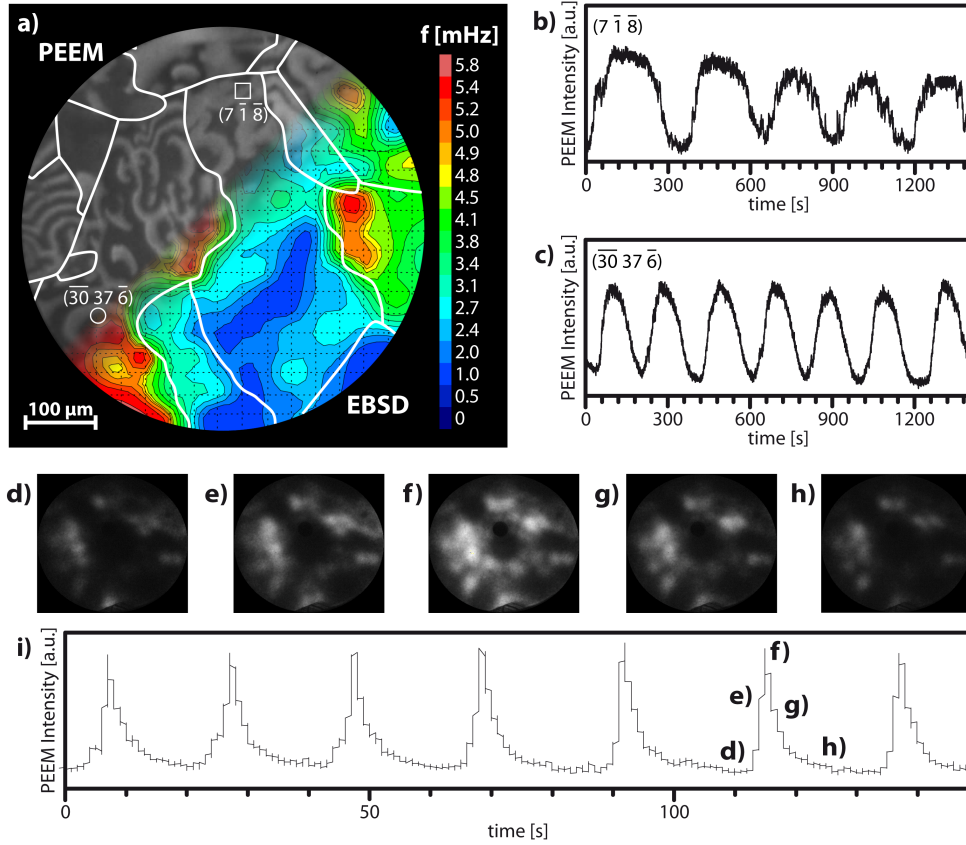


Fig. 4.21. Visualising the oscillating H_2 oxidation on differently scaled model systems: a) Combination of the PEEM-video frame and the frequency map, which were already shown in Fig. 4.8. The frame taken during the ongoing H_2 oxidation on the Rh foil at 453 K, $p_{\text{O}_2} = 1.1 \times 10^{-6} \text{ mbar}$ and $p_{\text{H}_2} = 8.4 \times 10^{-7} \text{ mbar}$ shows the spatial turbulence-like distribution of the two steady states of different catalytic reactivity. The frequency map illustrates the spatial distribution of the local oscillation frequencies; b - c) Local PEEM intensities measured within the $Rh(7\bar{1}\bar{8})$ and the $Rh(\bar{30}\bar{37}\bar{6})$ domain, as already shown in Fig. 4.8; d - h) Sequence of FEM images of the Rh nanotip depicting one oscillation cycle in the H_2 oxidation at 434 K, $p_{\text{O}_2} = 1.6 \times 10^{-6} \text{ mbar}$ and $p_{\text{H}_2} = 2.6 \times 10^{-7} \text{ mbar}$. (d - f) illustrate the kinetic transition from the poisoned (oxygen covered) state to the active (reduced) state while (f - h) depict the kinetic transition from the active (reduced) state to the poisoned (oxygen covered) state; i) Oscillating local FEM intensity averaged over the whole Rh nanotip. The corresponding positions of the frames shown in (d) - (h) are marked.

domain of the Rh foil during the oscillating H_2 oxidation and the domain specific (i.e. structure related) differences in the oscillation frequency. Exemplary the differences in the oscillating PEEM-image brightness of the $Rh(7\bar{1}\bar{8})$ and the $Rh(\bar{30}\bar{37}\bar{6})$ domain can be seen by comparing Fig. 4.21b and c. The parameters leading to these differences in the local oscillation frequency, namely the orientation of the predominant terraces, the width

4 Experimental results

of these terraces and the roughness of the step edges, were already discussed in 4.2.2. In turn, the oscillations on different facets of the Rh nanopip are globally well coupled due to the high hydrogen diffusivity and the nm-sized distances between the facets. Thus the image brightness of the FEM-snap shots shown in Fig. 4.21c - g changes (within the camera time-resolution of 0.02 s) simultaneously for all facets of the Rh tip - regardless of their differing surface structure. Further, it could be shown, that variations of the imaging electric field do not influence the observed oscillation frequency of 47 mHz, which was stable in a temperature range of 428 to 443 K with a deviation of only 0.37 mHz. The already presented results concerning the influence of the surface structure on the oscillation frequency, which were discussed in detail in 4.2.2, are in agreement with the fact, that the H₂ oxidation generally oscillates on the Rh tip with a higher frequency than on the Rh foil, since the highly curved surface of the tip exhibits generally a higher step density and a higher concentration of kink atoms than the μm-sized domains of the foil.

Summary

The comparison of the results obtained for the Rh foil by PEEM and for the Rh nanopip by FEM shows, that the Rh tip is more tolerant towards oxygen poisoning than the sputtered Rh foil. This higher tolerance can be explained by the increased sticking coefficient for H₂ on the tip surface. Further it was shown, that the H₂ oxidation can oscillate on a Rh nanopip under quasi field-free conditions. This oscillations occur with a significantly higher frequency than those on the stepped domains of the Rh foil. This increase can be addressed to the differences in the roughness of the Rh surface of the foil and the nanopip.

4.4 The feedback mechanism of the oscillating hydrogen oxidation on pure rhodium

As already mentioned in 2.4, two requirements need to be fulfilled to enable self-sustaining oscillations: first, the reaction must exhibit a bistable behaviour and, secondly, a feedback mechanism, which initialises the switches between the two steady states, must exist [58]. Examples of illustrative feedback mechanisms governing the oscillating behaviour can be found in ecosystems. A prime example is the periodic change of the populations of prey and predators within a certain confined region. If the prey population is large enough, the predators find enough food and their population grows. This increase leads to a decrease of the prey population and soon, the predators will not find enough food anymore and start to starve. The followed decrease of the population of predators enables the population of prey to recover and thus the cycle is closed. The oscillating behaviour of these two populations and the phase shift between them are described in detail in a study based on the numbers of furs from hares and lynxes delivered to the Hudson's Bay Company between 1845 and 1935 [143].

In the case of a chemical reaction, ascertaining a proper feedback mechanism is often much more difficult. Some feedback mechanisms like the reversible segregation of one compound of a bimetallic catalyst or the lifting of the reconstruction of surfaces were already mentioned in 2.4. However, these mechanisms do not fit to our reaction system since the studied samples consist of pure Rh and since, according to FIM observations, Rh surfaces do not reconstruct under the studied reaction conditions. In turn, our experimental results indicate, that the oscillations of the H₂ oxidation observed in the present studies show a certain resemblance to the field induced oscillations ruled by the formation of subsurface oxygen, as already described in 2.4.2. Experimental indications, supporting this idea are presented below.

4.4.1 Lowering of the local work function during the catalytic hydrogen oxidation on polycrystalline rhodium

As already shown in 4.1.1, hydrogen fronts which propagate on a polycrystalline Rh surface are not confined by domain boundaries and thus can spread unhindered across the whole Rh foil. Since during a kinetic transition usually multiple reaction fronts nucleate on the Rh foil at different nucleation centers, the collision of these fronts is unavoidable.

4 Experimental results

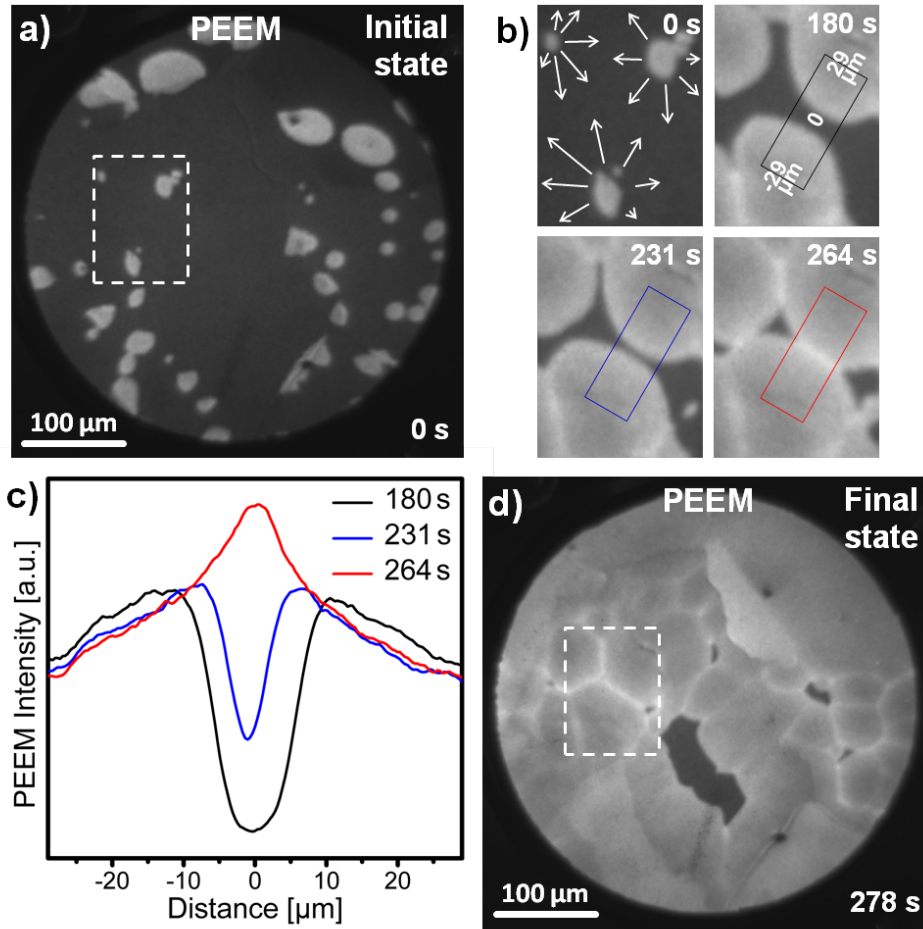


Fig. 4.22. Formation of the low work function network due to the collisions of reaction fronts in the ongoing H₂ oxidation on the polycrystalline Rh foil: a) PEEM-video frame showing hydrogen fronts originating from multiple nucleation centers. The image was taken at 513 K, $p_{O_2} = 7.7 \times 10^{-7}$ mbar and $p_{H_2} = 1 \times 10^{-6}$ mbar; b) Approach and collision of reaction fronts nucleated within the region marked in (a). The collision event leads to the formation of bright stripes, i.e. to regions of low work function; c) Intensity profiles measured within the three colour-coded boxes marked in (b); d) Bright net-like structure formed by the collisions of hydrogen fronts.

Figure 4.22a shows a PEEM-video frame recorded just after such nucleation events. The hydrogen fronts nucleated within the rectangular region marked in Fig. 4.22a approach and collide with each other, as shown in Fig. 4.22b. The collisions of the fronts lead to the formation of regions exhibiting a significantly increased image brightness, i.e. to regions of a lower work function. This increase is also illustrated by the intensity profiles, shown in Fig. 4.22c, which correspond to the three colour-coded boxes marked in Fig. 4.22b. It is clearly seen, that the curve with a minimum turns into a curve with a maximum in the

4 Experimental results

collision region. Finally, Fig. 4.22d shows the formed "network" of bright stripes, which is not related to the grain boundaries or defects, but solely reflects the geometry of collision events.

The lowering of the local work function of a $Rh(111)$ single crystal surface due to colliding reaction fronts was already observed for the NO reduction by H_2 [144] and also for the H_2 oxidation after a long-term oxygen pretreatment ($T = 770\text{ K}$, $p_{O_2} = 2 \times 10^{-4}\text{ mbar}$ and $t_{ox} = 36\text{ h}$) [49]. In both cases the lowering of the local work function could be addressed to the formation of subsurface oxygen. If oxygen adsorbs on a metallic surface, a dipole moment is formed, which increases the local work function. In turn, incorporated oxygen forms an inverse dipole moment (in comparison to adsorbed oxygen), which lowers the local work function below the work function of the clean surface [113].

In the present case of the catalytic H_2 oxidation on Rh, the formed hydrogen-Rh bonds are far weaker than the oxygen-Rh bonds [145]. On the $Rh(111)$ surface, the strong oxygen-Rh bonds even lead to a rearrangement of the surface atoms since the threefold coordinated oxygen draws the Rh atoms, which are bound to the atomic oxygen, 0.14 \AA out of the surface. This enlargement of the Rh-Rh bonds by about 4% indicates a weakening of the metal-metal bonds [145]. Since such modifications may only occur on oxygen covered Rh surfaces but not on reduced Rh, a tension gradient might occur close to reaction fronts. The collisions of reaction fronts lead to the doubling of the surface tension, which may promote the diffusion of adsorbed oxygen to subsurface sites.

Thus it seems reasonable to address the formation of bright stripes, which was observed during the ongoing H_2 oxidation on the polycrystalline Rh foil, to the formation of subsurface oxygen. The "network" remaining after such collisions illustrate a landscape of the enhanced subsurface oxygen formation.

4.4.2 The proposed feedback mechanism

Since the observed oscillation frequencies differ on differently oriented regions of the Rh foil, the feedback mechanism also needs to include processes, which exhibit structure related kinetics. Thus in the following, the formation and removal of the bright stripes is exemplary compared for two regions of different crystallographic orientation.

Figure 4.23 illustrates the formation and removal of the bright stripes on the $Rh(\bar{7}4\bar{8})$ and the $Rh(\bar{3}0\bar{3}7\bar{6})$ surface of the polycrystalline Rh foil. The initial increase of the local PEEM intensities indicates the formation, the red coloured part of the graphs the lifetime and the following decrease of the intensity the removal of subsurface oxygen. Comparing

4 Experimental results

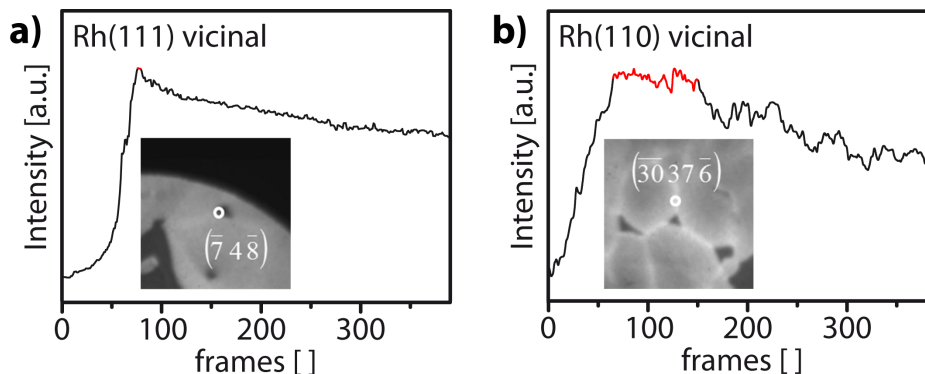


Fig. 4.23. Formation and removal of bright stripes on differently oriented Rh surfaces: a) Temporal evolution of the local PEEM intensity illustrating the formation and removal of the bright stripes on the $Rh(\bar{7}4\bar{8})$ domain at 513 K , $p_{\text{O}_2} = 7.7 \times 10^{-7}\text{ mbar}$ and $p_{\text{H}_2} = 1 \times 10^{-6}\text{ mbar}$. The lifetime of the stripe is red coloured; b) The same as (a) but for the $Rh(\bar{3}0\bar{3}7\bar{6})$ domain.

the two shown plots reveal that the lifetime of the bright stripes is far lower on the $Rh(\bar{7}4\bar{8})$ surface than on the $Rh(\bar{3}0\bar{3}7\bar{6})$ surface, at least under the studied conditions. The results discussed above lead to the suggestion, that the formation of subsurface oxygen serves as feedback mechanism for the oscillating H_2 oxidation on Rh.

Figure 4.24a illustrates the suggested mechanism of the observed oscillations. On the metallic Rh surface oxygen adsorbs primarily since the sticking coefficient of oxygen is higher than that of hydrogen. When the oxygen coverage reaches a certain value, oxygen starts to incorporate into the bulk. After the saturation of all subsurface sites, oxygen subsequently forms a surface oxide layer. Since this process significantly decreases the sticking coefficient of oxygen, hydrogen starts to adsorb preferentially and reactively removes the previously adsorbed oxygen by forming H_2O , which nearly immediately desorbs from the Rh surface. If the oxygen coverage decreases below a certain value, subsurface oxygen diffuses to the surface where it is consumed by the ongoing H_2O production. On the reduced Rh surface oxygen starts to primarily adsorb again and depletes the previously adsorbed hydrogen by forming H_2O . The oxygen coverage again increases until oxygen starts to incorporate into the bulk and thus closes the cycle.

A similar feedback mechanism for the oscillating H_2 oxidation on Rh tips in high electric fields was already discussed in 2.4.2, but in the case of this FIM study, the formation of subsurface oxygen is, at least mainly, stimulated by the applied field [82]. However, the present results show, that a sufficiently rough Rh surface can also enable the formation of subsurface oxygen, i.e. that the H_2 oxidation can oscillate on pure Rh if the surface provides sufficient roughness. Subsequently it can be concluded, that the local oscillation

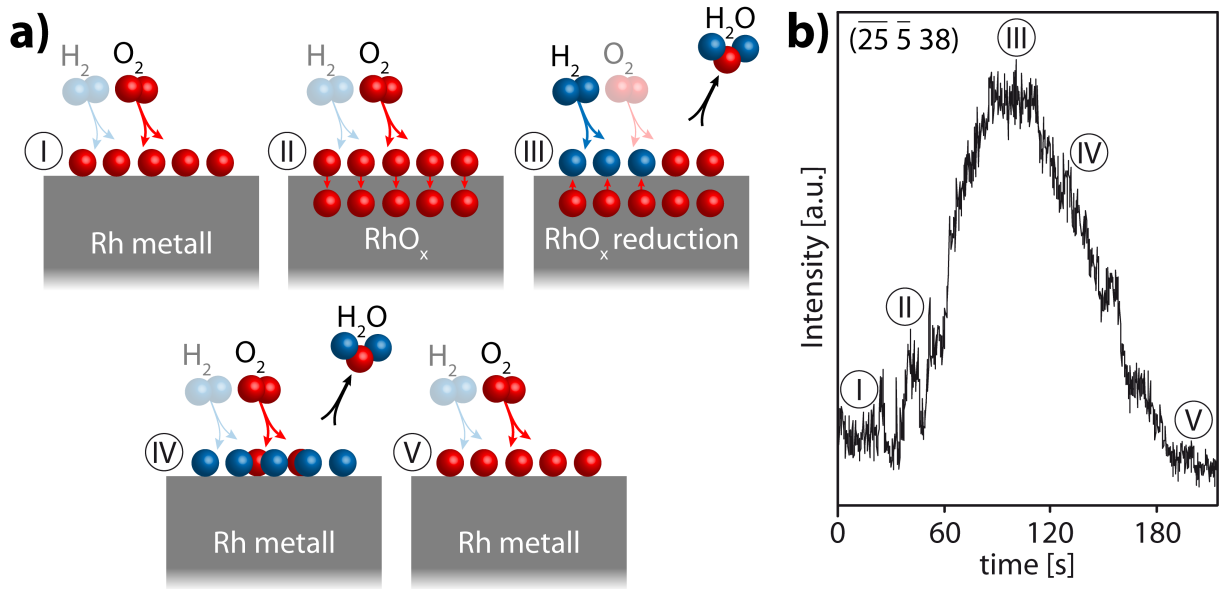


Fig. 4.24. Suggested mechanism of the oscillating H_2 oxidation on Rh: a) Schematic illustration of the proposed mechanism. I - Preferential adsorption of oxygen leads to an oxygen covered surface, II - Formation of subsurface oxygen reducing the sticking coefficient for oxygen, III - Preferential adsorption of hydrogen leads to the reduction of the Rh surface, IV - Preferentially adsorbing oxygen depletes the previously adsorbed hydrogen, V - Closing of the cycle since the surface is again oxygen covered; b) Temporal evolution of the local PEEM intensity on the $\text{Rh}(\overline{25} \overline{5} 38)$ domain. The steps explained in (a) are marked.

frequency must be strictly related to the kinetics of the formation of subsurface oxygen, e.g. on a too smooth Rh surface probably not enough subsurface oxygen can be formed within a reasonable time to initiate the change of the adsorption properties necessary to enable the oscillating behaviour of the H_2 oxidation. In turn, at rough surfaces the formation and reduction of subsurface oxygen governs the frequency of oscillations, i.e. a higher roughness of the surface leads to a higher rate of the subsurface oxygen formation and thus to a higher oscillation frequency, as discussed in 4.2.2.

Summary

The presented PEEM observations revealed, that the collisions of hydrogen fronts on the polycrystalline Rh foil may result in the formation of bright stripes, i.e. areas exhibiting a low work function. The observed "network" of bright stripes reflects the geometry of collision events and not the net of the domain borders. Since the dipole moment of subsurface oxygen, which is inverse to the dipole moment of adsorbed oxygen, lowers the local work function, the bright stripes may indicate the formation of subsurface oxygen.

4 *Experimental results*

This insight leads to the suggestion that the reversible formation of subsurface oxygen may serve as feedback mechanism for the oscillating H₂ oxidation on pure Rh. Since the kinetics of the formation of subsurface oxygen is related to the surface roughness, the correlation between the frequency of oscillations and the surface structure of individual domains can be explained.

5

Conclusions

In the present thesis, the spatio-temporal behaviour of the catalytic hydrogen oxidation on high-Miller-index domains of a polycrystalline Rh foil was studied in the 10^{-6} mbar pressure range by photoemission electron microscopy (PEEM) while quadrupole mass spectrometry (QMS) was used to monitor the gas phase.

The ongoing reaction was monitored *in situ* by PEEM and the nucleation and propagation of hydrogen reaction fronts in the steady state regime have been studied. It was shown, that these fronts nucleate on grain boundaries between the domains as well as on defects within the domains. The shape of the occurring fronts is determined by the diffusivity of adsorbed hydrogen, which is highly mobile on Rh surfaces, while the adsorbed oxygen can be treated as relatively immobile under the present reaction conditions. Since the diffusivity of hydrogen is influenced by features of the local surface structure, such as steps or the furrows of the *Rh*(110) surface, anisotropic reaction front propagation was expected for many domains and directly observed by PEEM. The influence of the individual surface structures on the front propagation could be decreased by Ar^+ sputtering, which equalises the peculiarities of different surfaces by creating artificial defects.

In contrast to the CO oxidation on polycrystalline foils, where spreading reaction fronts are confined by domain borders, hydrogen fronts spread on the Rh foil unhindered across grain boundaries because the diffusivity of adsorbed hydrogen is significantly higher than that of adsorbed CO. Thus, the catalytic behaviour of different domains is coupled by hydrogen diffusion, despite of the differences in the local surface structures of the individual domains.

The kinetics of the reaction have been studied by applying the *kinetics by imaging* approach, which is based on the fact, that both, the local PEEM image brightness and the local H_2O production rate depend on the local surface coverage of the adsorbed reactants. The oxygen covered (inactive) Rh surface exhibits a higher work function which leads to a lower photoelectron yield (darker PEEM image) than the reduced (active) surface. In this way, the kinetic transitions from the inactive to the active state and vice versa could be

5 Conclusions

monitored by PEEM. Monitoring the reaction by PEEM during the cyclewise variation of the partial hydrogen pressure at constant oxygen pressure and at a constant temperature reveals the hysteresis-like kinetics of the reaction. This reflects the bistability in the H₂ oxidation on Rh that originates from the Langmuir-Hinshelwood mechanism under the consideration of the inequivalence of the adsorption of reactants, i.e. of hydrogen and oxygen. A set of such hysteresis-measurements performed at different temperatures allows to construct a kinetic phase diagram, i.e. a plot which characterises the catalytic behaviour of the sample in a broad parameter range. Additional Ar⁺ sputtering of the sample changes the catalytic behaviour, since the artificially created defects shift the hydrogen-oxygen equilibrium towards the hydrogen side, i.e. the kinetic phase diagram of the sputtered Rh foil is shifted towards lower hydrogen pressures.

After varying the reaction conditions (p_{H_2} , p_{O_2} and T) self-sustaining oscillations in the H₂ oxidation on the Rh foil were observed. Unexpectedly, each particular domain exhibited an individual oscillation frequency and a certain oscillation pattern, despite of the reaction front spreading across the grain boundaries. The spatial distribution of these local oscillation frequencies was summarised in a frequency map. The comparison of the frequency map with the electron backscatter diffraction map (EBSD map) revealed, that the reaction oscillates with a lower frequency on smoother vicinal $Rh(110)$ surfaces than on rougher vicinal $Rh(110)$ surfaces which exhibit a higher density of low coordinated step and kink atoms.

The PEEM observations have also revealed, that the occurring oscillation patterns result from the spreading and overlap of the spirally shaped waves which originate at nucleation centers. These waves propagate unhindered across grain boundaries, although the width, the velocity and the radius of the propagating wave change abruptly on the grain boundary.

The results obtained on the Rh foil indicate, that a certain degree of roughness is necessary for the appearance of oscillations. To prove this indication, the catalytic behaviour of the H₂ oxidation was studied on a $Rh(111)$ single crystal surface containing a furrow-like mesoscopic defect with a width of 30 μm and a depth of 1 μm as was measured by AFM. PEEM observations of the H₂ oxidation on this sample revealed, that the reaction shows an oscillating behaviour within the furrow-like defect which exhibits highly stepped surfaces on the side walls of the furrow. In turn, the reaction does not oscillate on the surrounding flat single crystal surface. This observation as well as the analysis of the oscillating behaviour of the reaction on differently oriented domains of the Rh foil revealed that an atomically rough (stepped or kinked) surface is necessary to observe oscillations

5 Conclusions

in the H₂ oxidation under present reaction conditions.

The results obtained on the μm -sized domains of the Rh foil were compared with results obtained on a Rh nanotip using FEM. Since the surface of the highly curved apex of the nanotip exhibits a higher density of low coordinated step and kink atoms than the Rh foil, the kinetic phase diagram for the H₂ oxidation on such a tip is expected to be shifted towards lower hydrogen pressures than that for the annealed or the additionally Ar⁺ sputtered Rh foil. It can also be expected, that the H₂ oxidation should oscillate with a higher frequency on the Rh nanotip than on the planar domains of the Rh foil. The detailed analysis of the experimental results obtained for the μm -sized domains of the Rh foil and the nm-sized Rh tip confirms both assumptions.

Generally, self-sustaining oscillations in surface reactions can only occur if the reaction exhibits a bistable behaviour and if a proper feedback mechanism exists, which governs the periodic switches between the two steady states. While the bistability of the H₂ oxidation on Rh is known, the feedback mechanism needs to be revealed. Since the oscillations were observed solely on stepped surfaces, the formation of subsurface oxygen might serve as suitable feedback mechanism. To confirm this suggestion, a PEEM study focused on colliding hydrogen fronts on the Rh foil surface was performed. This study revealed, that the collision of fronts often leads to the formation of low work function regions, which appear as "bright stripes" in PEEM images. Since the formation of subsurface oxygen lowers the local work function of Rh, the formation of bright stripes testifies the diffusion of atomic oxygen into subsurface sites. This experimental observation confirms the idea of the formation of subsurface oxygen as feedback mechanism for the H₂ oxidation on stepped Rh surfaces.

List of figures

1.1	Energy diagram of the chemical reaction $A + B \rightarrow AB$ without and with using a proper catalyst	5
1.2	Possible ways of bridging the pressure and materials gap	9
2.1	Schema of the Langmuir-Hinshelwood mechanism of the catalytic H_2 oxidation on Rh	13
2.2	Construction of a kinetic phase diagram	16
2.3	Nonreconstructed and reconstructed Pt surfaces	19
3.1	Schematic drawing of the experimental set-up	23
3.2	Experimental set-up	24
3.3	View into the PEEM-chamber through a CF40 window	26
3.4	View through a CF40 window into the XPS-chamber	28
3.5	Load lock	29
3.6	Energy diagram for the photoeffect	31
3.7	Scheme of the contrast formation in PEEM	32
3.8	Schematic drawing of a UV-PEEM	33
3.9	Kinetics by imaging	35
3.10	Working principle of a QMS	36
3.11	Working principle of an XPS	38
3.12	Working principle of an XPS-analyser	39
3.13	Schematic cross section of a hemispherical electron energy analyser	40
3.14	Universal mean free path curve	41
3.15	Schematic photoelectron spectrum for an excitation energy of a few keV	42
3.16	Example of chemical shifts for different oxidation states of Zr	43
3.17	Working principle of an EBSD	44
3.18	Working principle of an AFM	46
3.19	Surface structure of Rh surfaces	47
3.20	The polycrystalline Rh foil	48
4.1	Nucleation of hydrogen fronts in the H_2 oxidation on Rh	52
4.2	Propagation of a H_2 reaction front across a grain boundary	53
4.3	Isotropic and anisotropic propagation of H_2 reaction fronts on stepped Rh surfaces	54

4.4	Propagation of reaction fronts on annealed and on additionally sputtered domains of the Rh foil	56
4.5	Kinetics by imaging for the H ₂ oxidation on the stepped polycrystalline Rh foil	58
4.6	Comparison of the kinetic phase diagrams for the annealed and the Ar ⁺ sputtered Rh foil	59
4.7	Visualising isothermal oscillations in the catalytic H ₂ oxidation on the polycrystalline Rh foil	62
4.8	Spatial distribution of the oscillation frequencies in the catalytic H ₂ oxidation on the polycrystalline Rh foil	63
4.9	Description of the <i>Rh</i> ($\overline{19}13$) surface using three structure related parameters	64
4.10	Oscillations in the H ₂ oxidation on different vicinal <i>Rh</i> (110) surfaces . . .	65
4.11	Pattern formation at a single nucleation center in the H ₂ oxidation on the Rh foil	66
4.12	Pattern formation at multiple nucleation centers	67
4.13	Formation of complex patterns during the oscillating H ₂ oxidation on the Rh foil	68
4.14	Mesoscopic defect on the <i>Rh</i> (111) single crystal	70
4.15	Spatio-temporal behaviour of the catalytic H ₂ oxidation on the <i>Rh</i> (111) single crystal sample	71
4.16	Temporal evolution of the local PEEM intensities on different vicinal <i>Rh</i> (100) surfaces	72
4.17	Visualising isothermal oscillations in the catalytic H ₂ oxidation on several domains of the polycrystalline Rh foil	73
4.18	Differently scaled Rh samples	75
4.19	Two differently scaled model systems	77
4.20	Kinetic phase diagrams for differently scaled Rh samples	78
4.21	Visualising the oscillating H ₂ oxidation on differently scaled model systems	79
4.22	Formation of the low work function network due to the collisions of reaction fronts in the ongoing H ₂ oxidation on the polycrystalline Rh foil	82
4.23	Formation and removal of bright stripes on differently oriented Rh surfaces	84
4.24	Suggested mechanism of the oscillating H ₂ oxidation on Rh	85

List of tables

2.1	Adsorption phases for oxygen on Rh and oxygen induced reconstructions of Rh surfaces	14
4.1	Comparison of the $Rh(7\bar{1}\bar{8})$ with the $Rh(\bar{3}\bar{0}\bar{3}\bar{7}\bar{6})$ surface	64
4.2	Comparison of the $Rh(\bar{2}\bar{5}\bar{5}\bar{3}\bar{8})$ with the $Rh(\bar{2}\bar{0}\bar{3})$ surface	65
4.3	Comparison of the $Rh(\bar{1}\bar{9}\bar{1}\bar{3})$ with the $Rh(\bar{3}\bar{1}\bar{2}\bar{4})$ surface	72

References

- [1] J. J. Berzelius, *Årsberättelsen om framsteg i fysik och kemi*, Royal Swedish Academy of Sciences, 1835.
- [2] P. E. McGovern, J. Zhang, J. Tang, Z. Zhang, G. R. Hall, R. A. Moreau, A. Nunez, E. D. Butrym, M. P. Richards, C. Wang, G. Cheng, Z. Zhao and C. Wang, *PNAS* **101** (2004) 17593.
- [3] <http://www.grandviewresearch.com/industry-analysis/catalyst-market>, 05.02.2017.
- [4] <http://www.grandviewresearch.com/press-release/catalyst-market-analysis>, 05.02.2017.
- [5] H. Davy, *Phil. Trans. R. Soc. Lond.* **106** (1816) 1.
- [6] H. Davy, *Phil. Trans. R. Soc. Lond.* **107** (1817) 77.
- [7] J. K. Laylin, *Nobel Laureates in Chemistry 1901-1992 (History of Modern Chemical Sciences)*, American Chemical Society, 1993.
- [8] F. Haber and R. L. Rossignol, *Z. f. Elektroch.* **19** (1913) 53.
- [9] F. Haber, *Die Naturwissenschaften* **49** (1922) 1041.
- [10] A. Boulamanti and J. A. Moya, *Renew. Sustainable Energy Rev.* **68** (2017) 1205.
- [11] J. W. Erisman, M. A. Sutton, J. Galloway, Z. Klimont and W. Winiwarter, *Nat. Geosci.* **1** (2008) 639.
- [12] R. D. Monte and J. Kašpar, *Top. Catal.* **28** (2004) 47.
- [13] M. V. Twigg, *Catal. Today* **163** (2011) 33.
- [14] T. H. Shin, M. Shin, G.-W. Park, S. Lee, S.-K. Woo and J. Yu, *Sustainable Energy Fuels* **1** (2017) 103.
- [15] F. Che, S. Ha and J.-S. McEwen, *Ind. Eng. Chem. Res.* **56** (2017) 1201.
- [16] A. Thallam Thattai, V. Oldenbroek, L. Schoenmakers, T. Woudstra P. V. Aravind, *Appl. Therm. Eng.* **114** (2017) 170.

Bibliography

- [17] Y. Sun, J. Li, Y. Zeng, B. S. Amirkhiz, M. Wang, Y. Behnamiana and J. Luo, *J. Mater. Chem. A* **3** (2015) 11048.
- [18] G. A. Somorjai and Y. Li, *Introduction to Surface Chemistry and Catalysis*, John Wiley & Sons, Inc., 2010.
- [19] I. Langmuir, *Trans. Faraday Soc.* **17** (1922) 607.
- [20] I. Langmuir, *Trans. Faraday Soc.* **17** (1922) 621.
- [21] G. Ertl, *Angew. Chem. Int. Ed.* **47** (2008) 3524.
- [22] H.-J. Freund, H. Kuhlenbeck, J. Libuda, G. Rupprechter, M. Bäumer and H. Hamann, *Top. Catal.* **15** (2001) 201.
- [23] T. Dellwig, G. Rupprechter, H. Unterhalt and H.-J. Freund, *Phys. Rev. Lett.* **85** (2000) 776.
- [24] A. Dubey, S. K. Kolekar, E. S. Gnanakumar, K. Roy, C. P. Vinod and C. S. Gopinath, *Catal. Struct. React.* **2** (2016) 1.
- [25] A. Stevanovic, J. Velmurugan, F. Yi, D. La Van and A. Kolmakov, *Microsc. Microanal.* **22** (2016) 1292.
- [26] E. P. Dougherty and H. Rabitz, *J. Chem. Phys.* **72** (1980) 6571.
- [27] G. B. Kauffman, *Platinum Metals Rev.* **43** (1999) 122.
- [28] P. P. Edwards, V. L. Kuznetsov, W. I. F. David and N. P. Brandon, *Energy Policy* **36** (2008) 4356.
- [29] S. Banerjee and D. E. Curtin, *J. Fluorine Chem.* **125** (2004) 1211.
- [30] V. Das, S. Padmanaban, K. Venkitesamy, R. Selvamuthukumar, F. Blaabjerg and P. Siano, *Renewable Sustainable Energy Rev.* **73** (2017) 10.
- [31] V. V. Gorodetskii, B. E. Nieuwenhuys, W. M. H. Sachtler and G. K. Boreskov, *Appl. Surf. Sci.* **7** (1981) 355.
- [32] J. T. Yates Jr., P. A. Thiel and W. H. Weinberg, *Surf. Sci.* **82** (1979) 45.
- [33] G. Pauer, A. Eichler, M. Sock, M. G. Ramsey, F. Netzer and A. Winkler, *J. Chem. Phys.* **119** (2003) 5253.

Bibliography

- [34] S. H. Payne, H. J. Kreuzer, W. Frie, L. Hammer and K. Heinz, *Surf. Sci.* **421** (1999) 279.
- [35] J. T. Yates Jr., P. A. Thiel and W. H. Weinberg, *Surf. Sci.* **84** (1979) 427.
- [36] V. V. Gorodetskii, B. E. Nieuwenhuys, W. M. H. Sachtler and G. K. Boreskov, *Surf. Sci.* **108** (1981) 225.
- [37] L. Hammer, W. Nichtl-Pecher, N. Elbel, W. Stammer, K. Heinz and K. Müller, *Surf. Sci.* **287** (1993) 84.
- [38] A. N. Salanov and V. I. Savchenko, *React. Kinet. Catal. Lett.* **48** (1992) 537.
- [39] E. Schwarz, J. Lenz, H. Wohlgemuth and K. Christmann, *Vacuum* **41** (1990) 167.
- [40] J. Derouin, R. G. Farber and D. R. Killelea, *J. Phys. Chem. C* **119** (2015) 14748.
- [41] W. Oed, B. Dötsch, L. Hammer, K. Heinz and K. Müller, *Surf. Sci.* **207** (1988) 55.
- [42] A. G. Norris, F. Schedin, G. Thornton, V. R. Dhanak, T. S. Turner and R. McGrath, *Phys. Rev. B* **62** (2000) 2113.
- [43] G. Comelli, V. R. Dhanak, M. Kiskinova, N. Pangher, G. Paolucci, K. C. Prince and R. Rosei, *Surf. Sci.* **260** (1992) 7.
- [44] C. Africh, F. Esch, G. Comelli and R. Rosei, *J. Chem. Phys.* **115** (2001) 477.
- [45] E. Vesselli, C. Africh, A. Baraldi, G. Comelli, F. Esch and R. Rosei, *J. Chem. Phys.* **114** (2001) 4221.
- [46] F. M. Leibsle, P. W. Murray, S. M. Francis, G. Thornton and M. Bowker, *Nature* **363** (1993) 706 .
- [47] V. R. Dhanak, G. Comelli, G. Cautero, G. Paolucci, K. C. Prince, M. Kiskinova and R. Rosei, *Chem. Phys. Lett.* **188** (1992) 237.
- [48] G. Hoogers and D. A. King, *Surf. Sci.* **286** (1993) 306.
- [49] A. Schaak and R. Imbihl, *J. Chem. Phys.* **113** (2000) 9822.
- [50] G. Ertl, *Science* **254** (1991) 1750.
- [51] W. C. Bray, *J. Am. Chem. Soc.* **43** (1921) 1262.

Bibliography

- [52] G. T. Fechner, *Schweigg J. Chem. Phys.* **53** (1828) 129.
- [53] A. N. Zaikin and A. M. Zhabotinsky, *Nature* **225** (1970) 535.
- [54] D. Zhang, L. Györgyi and W. R. Peltier, *Chaos* **3** (1993) 723.
- [55] P. Hugo, *Ber. Bunsen-Ges. Phys. Chem.* **74** (1970) 121.
- [56] P. Hugo and M. Jakubith, *Chem.-Ing.-Tech.* **44** (1972) 383.
- [57] C. G. Takoudis and L. D. Schmidt, *J. Phys. Chem.* **87** (1983) 964.
- [58] U. F. Frank, *Temporal Order*, Springer, 1985.
- [59] F. J. M. Horn and R. C. Lin, *Ind. Eng. Chem. Proc. Des. Dev.* **6** (1967) 21.
- [60] J. Wolff, A. G. Papathanasiou, I. G. Kevrekidis, H. H. Rotermund and G. Ertl, *Science* **294** (2001) 134.
- [61] S. Y. Yamamoto, C. M. Surko, M. B. Maple and R. K. Pina, *J. Chem. Phys.* **102** (1995) 8614.
- [62] M. P. Cox, G. Ertl and R. Imbihl, *Phys. Rev. Lett.* **54** (1985) 1725.
- [63] G. Ertl, *Adv. Catal.* **37** (1990) 213.
- [64] R. Imbihl, *Prog. Surf. Sci.* **44** (1993) 185.
- [65] R. Imbihl and G. Ertl, *Chem. Rev.* **95** (1995) 697.
- [66] R. Imbihl, *Catal. Today* **105** (2005) 206.
- [67] P.-A. Carlsson, V. P. Zhdanov and M. Skoglundh, *Phys. Chem. Chem. Phys.* **8** (2006) 2703.
- [68] N. Freyer, M. Kiskinova, G. Pirug, H. P. Bonzel, *Surf. Sci.* **166** (1986) 206.
- [69] Y. Suchorski, W. Drachsel, V. Gorodetskii, V. Medvedev and H. Weis, *Surf. Sci.* **600** (2006) 1579.
- [70] R. Imbihl, M. P. Cox and G. Ertl, *J. Chem. Phys.* **84** (1986) 3519.
- [71] R. Imbihl, M. P. Cox, G. Ertl, H. Müller and W. Brenig, *J. Chem. Phys.* **83** (1985) 1578.

Bibliography

- [72] P. K. Tsai and M. B. Maple, *J. Catal.* **101** (1986) 142.
- [73] G. Saidi and T. T. Tsotsis, *Surf. Sci.* **161** (1985) L591.
- [74] F. Behrendt, O. Deutschmann, R. Schmidt and J. Warnatz, *Heterogeneous Hydrocarbon Oxidation*, American Chemical Society, 1996.
- [75] V. V. Gorodetskii, A. A. Sametova, A. V. Matveev and V. M. Tapilin, *Catal. Today* **144** (2009) 219.
- [76] D. Eng, M. Stoukides and T. McNally, *J. Catal.* **106** (1987) 343.
- [77] M. Hock and J. Küppers, *Surf. Sci.* **188** (1987) 575.
- [78] A.-S. Mårtensson, *Surf. Sci.* **215** (1989) 55.
- [79] F. Lovis, T. Smolinsky, A. Locatelli, M. Á. Niño and R. Imbihl, *J. Phys. Chem. C* **116** (2012) 4083.
- [80] T. Smolinsky, M. Homann and R. Imbihl, *Phys. Chem. Chem. Phys.* **18** (2016) 970.
- [81] Y.-E. Li and R. D. Gonzalez, *Catal. Lett.* **1** (1988) 229.
- [82] J.-S. McEwen, P. Gaspard, T. Visart de Bocarmé and Norbert Kruse, *PNAS* **106** (2009) 3006.
- [83] V. Medvedev, Y. Suchorski, C. Voss, T. Visart de Bocarmé, T. Bär and N. Kruse, *Langmuir* **14** (1998) 6151.
- [84] E. Brüche, *E. Z. Physik* **86** (1933) 448.
- [85] K. Oura, V. G. Lifshits, A. Saranin, A. V. Zotov and M. Katayama, *Surface Science. An Introduction*, Springer, 2003.
- [86] W. Engel, M. E. Kordesch, H. H. Rotermund, S. Kubala and A. von Oertzen, *Ultramicroscopy* **36** (1991) 148.
- [87] M. E. Kordesch, W. Engel, G. J. Lapeyre, E. Zeitler and A. M. Bradshaw, *Appl. Phys. A* **49** (1989) 399.
- [88] H. H. Rotermund, *Surf. Sci.* **603** (2009) 1662.

Bibliography

- [89] M. Ehsasi, M. Berdau, T. Rebitzki, K.-P. Charlé, K. Christmann and J. H. Block, *J. Chem. Phys.* **98** (1993) 9177.
- [90] M. Berdau, G. G. Yelenin, A. Karpowicz, M. Ehsasi, K. Christmann and J. H. Block, *J. Chem. Phys.* **110** (1999) 11551.
- [91] H. Hertz, *Ann. Phys.* **267** (1887) 983.
- [92] W. Hallwachs, *Ann. Phys.* **269** (1888) 301.
- [93] A. Einstein, *Ann. Phys.* **332** (1905) 132.
- [94] H. Simon and R. Suhrmann, *Der lichtelektrische Effekt und seine Anwendungen*, Springer, 1958.
- [95] S. Günther, B. Kaulich, L. Gregoratti and M. Kiskinova, *Prog. Surf. Sci.* **70** (2002) 187.
- [96] Y. Suchorski, C. Spiel, D. Vogel, W. Drachsel, R. Schlögl and G. Rupprechter, *ChemPhysChem* **11** (2010) 3231.
- [97] P. D. Innes, *Proc. R. Soc. A* **79** (1907) 442.
- [98] K. Siegbahn, *Rev. Mod. Phys.* **54** (1982) 709.
- [99] http://www.yambo-code.org/tutorials/Surface_spectroscopy/index.php, 24.06.2013.
- [100] D. P. Woodruff and T. A. Delchar, *Modern Techniques Of Surface Science*, Cambridge University Press (1994).
- [101] I. Bepalov, M. Datler, S. Buhr, W. Drachsel, G. Rupprechter and Y. Suchorski, *Ultramicroscopy* **159** (2015) 147.
- [102] A. J. Schwartz, M. Kumar, B. L. Adams and D. P. Field, *Electron Backscatter Diffraction in Materials Science*, Springer, 2009.
- [103] http://www.ustem.tuwien.ac.at/fileadmin/_processed_/csm_ebsd_oim_b7b4525b9c.jpg, 19.04.2017.
- [104] S. Nishikawa and S. Kikuchi, *Nature* **121** (1928) 1019.
- [105] Y. Kainuma, *Acta Cryst.* **8** (1955) 247.

Bibliography

- [106] G. Binnig, C. F. Quate and C. Gerber, *Phys. Rev. Lett.* **9** (1986) 930.
- [107] J.-M. Zhang, F. Ma and K.-W. Xu, *Appl. Surf. Sci.* **229** (2004) 34.
- [108] Y.-N. Wena and J.-M. Zhang, *Solid State Commun.* **144** (2007) 163.
- [109] R. Smoluchowski, *Phys. Rev.* **60** (1941) 661.
- [110] H.-J. Freund, G. Meijer, M. Scheffler, R. Schlögl, M. Wolf, *Angew. Chem. Int. Ed.* **50** (2011) 10064.
- [111] X.-M. Zeng, R. Huang, Y.-H. Wen and S.-G. Sun, *Phys. Chem. Chem. Phys.* **17** (2015) 5751.
- [112] A. Schaak, S. Shaikhutdinov and R. Imbihl, *Surf. Sci.* **421** (1999) 191.
- [113] M. I. Monine, A. Schaak, B. Y. Rubinstein, R. Imbihl and L. M. Pismen, *Catal. Today* **70** (2001) 321.
- [114] H. Kondoh, R. Toyoshima, Y. Monya, M. Yoshida, K. Mase, K. Amemiya and B. S. Mun, *Catal. Today* **260** (2016) 14.
- [115] N. P. Lebedeva, M. T. M. Koper, J. M. Feliu and R. A. van Santen, *J. Phys. Chem. B* **106** (2002) 12938.
- [116] A. L. Walter, F. Schiller, M. Corso, L. R. Merte, F. Bertram, J. Lobo-Checa, M. Shipilin, J. Gustafson, E. Lundgren, A. X. Brio ú-Ríos, P. Cabrera-Sanfelix, D. Sánchez-Portal and J. E. Ortega, *Nat. Commun.* **6** (2015) 8903.
- [117] G. Lilienkamp, H. Wei, W. Maus-Friedrichs, V. Kempter, H. Marbach, S. Günther and Y. Suchorski, *Surf. Sci.* **532** (2003) 132.
- [118] A. Schaak and R. Imbihl, *Chem. Phys. Lett.* **283** (1998) 386.
- [119] M. Datler, I. Bepalov, S. Buhr, J. Zeininger, M. Stöger-Pollach, J. Bernardi, G. Rupprechter and Y. Suchorski, *Catal. Lett.* **146** (2016) 1867.
- [120] D. Vogel, C. Spiel, Y. Suchorski, A. Trincherro, R. Schlögl, H. Grönbeck and G. Rupprechter, *Angew. Chem. Int. Ed.* **51** (2012) 10041.
- [121] D. Vogel, C. Spiel, Y. Suchorski, A. Urich, R. Schlögl and G. Rupprechter, *Surf. Sci.* **605** (2011) 1999.

Bibliography

- [122] D. Vogel, Z. Budinska, C. Spiel, R. Schlögl, Y. Suchorski, G. Rupprechter, *Catal. Lett.* **143** (2013) 235.
- [123] C. Spiel, D. Vogel, R. Schlögl, G. Rupprechter and Y. Suchorski, *Ultramicroscopy* **159** (2015) 178.
- [124] I. Bespalov, M. Datler, G. Rupprechter and Y. Suchorski, (2017) (in preparation)
- [125] D. Vogel, C. Spiel, M. Schmid, M. Stöger-Pollach, R. Schlögl, Y. Suchorski and G. Rupprechter, *J. Phys. Chem. C* **117** (2013) 12054
- [126] S. B. Schwartz, L. D. Schmidt, G. B. Fisher, *J. Phys. Chem.* **90** (1986) 6194.
- [127] E. G. Seebauer, A. C. F. Kong, L. J. Schmidt, *J. Chem. Phys.* **88** (1988) 6597.
- [128] A. Makeev and R. Imbihl, *J. Chem. Phys.* **113** (2000) 3854.
- [129] A. Schaak, B. Nieuwenhuys and R. Imbihl, *Surf. Sci.* **441** (1999) 33.
- [130] G. Hoogers, B. Lesifik-Ortowska and D. A. King, *Surf. Sci.* **327** (1995) 47.
- [131] M. Datler, I. Bespalov, G. Rupprechter and Y. Suchorski, *Catal. Lett.* **145** (2015) 1120.
- [132] S. N. Payne, H. J. Kreuzer, W. Frie, L. Hammer and K. Heinz, *Surf. Sci.* **421** (1999) 279.
- [133] V. P. Zhdanov, *Surf. Sci.* **296** (1993) 261.
- [134] K. Rajagopalan, M. Sheintuch and D. Luss, *Chem. Eng. Commun.* **7** (1980) 335.
- [135] E. Lalik, A. Drelinkiewicz, R. Kosydar, T. Szumelda, E. Bielańska, D. Groszek, A. Iannetelli and M. Groszek, *Ind. Eng. Chem. Res.* **54** (2015) 7047.
- [136] P. Grosfils, P. Gaspard and T. Visart de Bocarmé, *J. Chem. Phys.* **143** (2015) 064705.
- [137] F. Mertens and R. Imbihl, *Chem. Phys. Lett.* **242** (1995) 221.
- [138] X.-M. Zeng, R. Huang, Y.-H. Wen and S.-G. Sun, *Phys. Chem. Chem. Phys.* **17** (2015) 5751.

Bibliography

- [139] Y. Suchorski, W. Drachsel, *Field Ion Microscopy (FIM) and Atom Probe (AP)*; in *Surface and Thin Film Analysis*, Wiley-VCH, 2011.
- [140] Y. Suchorski, *Field Ion and Field Desorption Microscopy: Principles and Applications*; in *Surface Science Tools for Nanomaterials Characterization*, Springer, 2015.
- [141] Y. Suchorski, R. Imbihl and V. Medvedev, *Surf. Sci.* **401** (1998) 392.
- [142] T. Visart de Bocarmé, T. Bär and N. Kruse, *Ultramicroscopy* **89** (2001) 75.
- [143] D. A. McLulich, *Fluctuations in the Number of Varying Hare*, University of Toronto Press, 1937.
- [144] N. M. H. Janssen, A. Schaak, B. E. Nieuwenhuys, R. Imbihl, *Surf. Sci.* **364** (1996) 555.
- [145] K. Christmann, *Surf. Sci. Rep.* **9** (1988) 1.

Publications

Journal articles

3. M. Datler, I. Bepalov, S. Buhr, J. Zeininger, M. Stöger-Pollach, J. Bernardi, G. Rupprechter and Y. Suchorski: *Hydrogen oxidation on stepped Rh surfaces: μm -scale versus nanoscale*; Catalysis Letters, **146** (2016) 1867 - 1874.
2. M. Datler, I. Bepalov, G. Rupprechter and Y. Suchorski: *Analyzing the reaction kinetics for individual catalytically active components: CO oxidation on a Pd powder supported by Pt foil*; Catalysis Letters, **145** (2015) 1120 – 1125.
1. I. Bepalov, M. Datler, S. Buhr, W. Drachsel, G. Rupprechter and Y. Suchorski: *Initial stages of oxide formation on the Zr surface at low oxygen pressure: an in situ FIM and XPS study*; Ultramicroscopy, **159** (2015) 147 – 151.

Conference contributions

39. M. Datler, J. Zeininger, C. Freytag, S. Buhr, P. Winkler, G. Rupprechter and Y. Suchorski: poster *H₂ oxidation on Rh: Guiding reaction instabilities through surface geometry*; 8th International Workshop on Surface Physics, Trzebnica, Poland; 26.06.2017 - 30.06.2017; in: "8th INTERNATIONAL WORKSHOP ON SURFACE PHYSICS (IWSP-2017)" (2017) 44
38. S. Buhr, J. Zeininger, M. Datler, C. Freytag, P. Winkler, G. Rupprechter and Y. Suchorski: poster *H₂ oxidation on Rh: Mapping the nm- and μm -sized reaction fronts*; 8th International Workshop on Surface Physics, Trzebnica, Poland; 26.06.2017 - 30.06.2017; in: "8th INTERNATIONAL WORKSHOP ON SURFACE PHYSICS (IWSP-2017)" (2017) 40
37. C. Freytag, M. Datler and Y. Suchorski: oral contribution *Local instabilities in the H₂ oxidation on rhodium: structural effects*; VSS VIENNA young SCIENTISTS SYMPOSIUM, TUtheSky Lounge, TU Vienna; 01.06.2017 - 02.06.2017; in: "VSS VIENNA young SCIENTISTS SYMPOSIUM" (2017) 13

Publications

36. M. Datler, I. Beshpalov, J. Zeininger, S. Buhr, M. Stöger-Pollach, J. Bernardi, C. Freytag, G. Rupprechter and Y. Suchorski: oral contribution *Guiding chemical waves through geometry: H₂ oxidation on Rh*; International FOXSI Conference 2017, TUtheSky Lounge, TU Vienna; 15.05.2017 - 17.05.2017
35. J. Zeininger, M. Datler, S. Buhr, G. Rupprechter and Y. Suchorski: oral contribution *Imaging catalysis on a nanoscale: H₂ oxidation on Rh*; International FOXSI Conference 2017, TUtheSky Lounge, TU Vienna; 15.05.2017 - 17.05.2017
34. S. Buhr, J. Zeininger, M. Datler, C. Freytag, P. Winkler, G. Rupprechter and Y. Suchorski: poster *H₂ oxidation on Rh: Mapping the nm- and μm-sized reaction fronts*; International FOXSI Conference 2017, TUtheSky Lounge, TU Vienna; 15.05.2017 - 17.05.2017
33. M. Datler: oral contribution *Spatio-temporal behaviour of the catalytic hydrogen oxidation on high-Miller-index rhodium surfaces*; Fokus Materialchemie, TU Wien, TU Wien; 15.03.2017
32. Y. Suchorski, S. Kozlov, M. Datler, I. Beshpalov, K. M. Neyman and G. Rupprechter: poster *Long ranging metal-oxide boundary effect in catalytic CO oxidation on ZrO₂-supported Pd*; 3S'17, Symposium on Surface Science 2017, St. Moritz, Switzerland; 05.03.2017 - 10.03.2017; in: "3S'17, Symposium on Surface Science 2017, Contributions" (2017) 101 - 102
31. M. Datler, I. Beshpalov, J. Zeininger, C. Freytag, M. Stöger-Pollach, J. Bernardi, G. Rupprechter and Y. Suchorski: oral contribution *Oscillating phenomena in confined mesoscopic reaction systems*; 6th Annual FOXSI PhD Workshop, Haus im Ennstal; 01.02.2017 - 04.02.2017
30. S. Buhr, J. Zeininger, M. Datler, C. Freytag, G. Rupprechter and Y. Suchorski: poster *Local instabilities in H₂ oxidation observed in mesoscopic and microscopic model reaction systems*; 6th Annual FOXSI PhD Workshop, Haus im Ennstal; 01.02.2017 - 04.02.2017
29. I. Beshpalov, M. Datler, S. Buhr, J. Zeininger, M. Stöger-Pollach, J. Bernardi, G. Rupprechter and Y. Suchorski: poster *Catalytic CO Oxidation on Stepped Rh Surfaces*; International FOXSI Conference 2016, TUtheSky Lounge, Technische Universität Wien; 23.05.2016 - 25.05.2016

Publications

28. M. Datler, I. Bepalov, S. Buhr, J. Zeininger, M. Stöger-Pollach, J. Bernardi, G. Rupprechter and Y. Suchorski: poster *Spatio-temporal oscillations in hydrogen oxidation on Rh: mesoscopic versus nanoscale*; SFB-F45 "FOXSI" Annual PhD Workshop 2016, Haus im Ennstal; 30.03.2016 - 02.04.2016
27. I. Bepalov, M. Datler, J. Zeininger, M. Stöger-Pollach, J. Bernardi, G. Rupprechter and Y. Suchorski: oral contribution *Catalytic CO oxidation on high index Rh surfaces*; SFB-F45 "FOXSI" Annual PhD Workshop 2016, Haus im Ennstal; 30.03.2016 - 02.04.2016
26. S. Buhr, J. Zeininger, I. Bepalov, M. Datler, G. Rupprechter and Y. Suchorski: oral contribution *Catalytic CO oxidation on Rh on the nanoscale*; SFB-F45 "FOXSI" Annual PhD Workshop 2016, Haus im Ennstal; 30.03.2016 - 02.04.2016
25. M. Datler, I. Bepalov, J. Zeininger, G. Rupprechter and Y. Suchorski: oral contribution *Spatio-temporal pattern evolution in oscillating H₂ oxidation on Rh*; 3S'16, Symposium on Surface Science 2016, St. Christoph am Arlberg; 21.02.2016 - 27.02.2016
24. M. Datler, I. Bepalov, S. Buhr, J. Zeininger, G. Rupprechter and Y. Suchorski: poster *Hydrogen oxidation on Rh: nm- versus μ m-scale*; SFB-F45 "FOXSI" Annual Meeting 2015, Stadtschlaining; 14.09.2015 - 16.09.2015
23. I. Bepalov, M. Datler, G. Rupprechter, J. Zeininger and Y. Suchorski: poster *CO oxidation on Rh: role of defects in the local reaction kinetics*; SFB-F45 "FOXSI" Annual Meeting 2015, Stadtschlaining; 14.09.2015 - 16.09.2015
22. M. Datler, I. Bepalov, G. Rupprechter and Y. Suchorski: poster *Spatially- and component-resolved reaction kinetics on a μ m-scale: CO oxidation on Pd model catalysts*; ECOSS-31 31st European Conference on Surface Science, Barcelona; 31.08.2015 - 04.09.2015
21. Y. Suchorski, M. Datler, I. Bepalov, J. Zeininger and G. Rupprechter: oral contribution *Local surface reaction kinetics "just by imaging"*; ECOSS-31 31st European Conference on Surface Science, Barcelona; 31.08.2015 - 04.09.2015
20. I. Bepalov, M. Datler, S. Buhr, J. Zeininger, P. Blaha, G. Rupprechter and Y. Suchorski: poster *Initial surface oxidation of Zr: XPS, PEEM, FIM, FEM and*

Publications

- DFT studies*; ECOS-31 31st European Conference on Surface Science, Barcelona; 31.08.2015 - 04.09.2015
19. M. Datler, I. Bespalov, J. Zeininger, G. Rupprechter and Y. Suchorski: poster *Mapping the Reaction Front Nucleation and Propagation in H₂ Oxidation on Rh*; 7th International Workshop on Surface Physics, Trzebnica, Poland; 21.06.2015 - 25.06.2015
 18. M. Datler, I. Bespalov, J. Zeininger, G. Rupprechter and Y. Suchorski: oral contribution *Visualizing Local Reaction Kinetics: Hydrogen Oxidation on Rhodium*; 7th International Workshop on Surface Physics, Trzebnica, Poland; 21.06.2015 - 25.06.2015
 17. I. Bespalov, M. Datler, S. Buhr, J. Zeininger, P. Blaha, G. Rupprechter and Y. Suchorski: poster *Bridging Scales in the Surface Oxidation of Zr: XPS, PEEM, FIM, FEM and DFT Studies*; 7th International Workshop on Surface Physics, Trzebnica, Poland; 21.06.2015 - 25.06.2015
 16. J. Zeininger, I. Bespalov and M. Datler: oral contribution *Initial Oxidation Of Zirconium: XPS And PEEM Studies*; Vienna Young Scientists Symposium, Wien; 25.06.2015 - 26.06.2015
 15. M. Datler, I. Bespalov, J. Zeininger, G. Rupprechter and Y. Suchorski: oral contribution *Visualizing Reaction Kinetics: Hydrogen Oxidation on Rh and Rh/ZrO₂ model catalysts*; International SFB FOXSI Symposium 2015, TUtheSky Lounge, Technische Universität Wien; 11.05.2015 - 13.05.2015
 14. M. Datler, I. Bespalov, J. Zeininger, G. Rupprechter and Y. Suchorski: poster *Topography of the reaction front nucleation and propagation in H₂ oxidation on Rh*; International SFB FOXSI Symposium 2015, TUtheSky Lounge, Technische Universität Wien; 11.05.2015 - 13.05.2015
 13. I. Bespalov, M. Datler, S. Buhr, J. Zeininger, P. Blaha, G. Rupprechter and Y. Suchorski: poster *Initial stages of Zr surface oxidation: XPS, PEEM, FIM, FEM and DFT studies*; International SFB FOXSI Symposium 2015, TUtheSky Lounge, Technische Universität Wien; 11.05.2015 - 13.05.2015

Publications

12. M. Datler, I. Bepalov, J. Zeininger, G. Rupprechter and Y. Suchorski: oral contribution *Hydrogen oxidation on Rh/ZrO₂ model catalysts: the role of the support*; 4th Annual FOXSI PhD Workshop, Haus im Ennstal; 29.03.2015 - 01.04.2015
11. I. Bepalov, M. Datler, S. Buhr, J. Zeininger, P. Blaha, G. Rupprechter and Y. Suchorski: poster *Surface Oxidation of Zr: PEEM, FIM, XPS and DFT Study*; 4th Annual FOXSI PhD Workshop, Haus im Ennstal; 29.03.2015 - 01.04.2015
10. M. Datler, I. Bepalov, G. Rupprechter and Y. Suchorski: poster *Reaction front nucleation and propagation in H₂ oxidation on Rh*; 4th Annual FOXSI PhD Workshop, Haus im Ennstal; 29.03.2015 - 01.04.2015
9. S. Buhr, I. Bepalov, M. Datler, G. Rupprechter and Y. Suchorski: poster *Initial oxide formation on the Zr surface at low oxygen pressure: an in situ FIM, PEEM and XPS study*; International Conference on Atom Probe Tomography Microscopy, Stuttgart; 31.08.2014 - 05.09.2014
8. I. Bepalov, M. Datler, G. Rupprechter and Y. Suchorski: poster *Compatibility of the nm-scale and μ m-scale studies of the catalytic CO oxidation on Pd: FIM/FEM versus PEEM*; International Conference on Atom Probe Tomography Microscopy, Stuttgart; 31.08.2014 - 05.09.2014
7. M. Datler, I. Bepalov, R. Schlögl, G. Rupprechter and Y. Suchorski: poster *The role of the surface morphology in the CO oxidation reaction: Pd powder versus plane Pd(hkl) surfaces*; SFB-F45 "FOXSI" Annual PhD Seminar 2014, Hochkar, Göstling; 07.04.2014 - 10.04.2014
6. Y. Suchorski, M. Datler, I. Bepalov, R. Schlögl and G. Rupprechter: poster *Laterally-resolved reaction kinetics in CO oxidation on Pd: powder versus plane Pd(hkl) surfaces*; 3S'14 Symposium on Surface Science 2014, St. Christoph/Arlberg, St. Christoph/Arlberg; 09.03.2014 - 15.03.2014
5. I. Bepalov, M. Datler, D. Vogel, Z. Budinska, R. Schlögl, G. Rupprechter and Y. Suchorski: poster *Surface oxides on Zr and Pd surfaces: an XPS and PEEM studies*; 2nd Annual SFB FOXSI Symposium, Conference Center Burg Schlaining; 18.09.2013 - 20.09.2013
4. D. Vogel, Z. Budinska, I. Bepalov, M. Datler, R. Schlögl, G. Rupprechter and Y. Suchorski: poster *Kinetics of oxides formation on Zr and Pd surfaces: an XPS and*

Publications

PEEM study; 6th International Workshop on Surface Physics, Niemcza, Poland;
01.09.2013 - 06.09.2013

3. I. Bepalov, M. Datler, D. Vogel, Z. Budinska, G. Rupprechter and Y. Suchorski:
poster *Reaction front propagation in the CO oxidation on Pd-powder catalysts*; SFB
FOXSI PhD Workshop 2013 "FOXSKI", Hochkar; 18.03.2013 - 21.03.2013
2. M. Datler: oral contribution *CO oxidation reaction on Palladium - Platinum model
catalysts: kinetic transitions and spatial coupling*; IMC Seminar der Technischen
Universität Wien, Technische Universität Wien; 16.01.2013
1. D. Vogel, Z. Budinska, M. Datler, Y. Suchorski, R. Schlögl and G. Rupprechter:
poster *Visualizing the CO oxidation on powder samples: palladium versus platinum*;
Annual SFB FOXSI Symposium, Burg Schleining; 26.09.2012 - 28.09.2012.

Curriculum vitae

Personal data

Full name Martin Datler

Date and place of birth September 23th 1986,
Vienna, Austria

Citizenship Austria

Address Liechtensteinstraße 117,
1090 Wien

E-Mail martin.datler@tuwien.ac.at

Education

10/2013 - 07/2017 Ph.D. studies at the Institute of Materials Chemistry,
Technische Universität Wien, Austria
Supervisors: Prof. Y. Suchorski and Prof. G. Rupprechter

09/2013 Magister rerum naturalium (eq. M.Sc.),
Technische Universität Wien, Austria
Thesis: CO oxidation reaction on palladium - platinum
model catalysts: the role of the support
Supervisor: Prof. Y. Suchorski

10/2006 - 09/2013 Teacher Training Programme (Physics and Chemistry)
Technische Universität Wien, Austria